UNIVERSITÀ
DEGLI STUDI
DI PADOVA

UNIVERSITÀ DEGLI STUDI DI PADOVA

Dipartimento di Ingegneria Industriale

Scuola di Dottorato di Ricerca in Ingegneria Industriale
Indirizzo in Ingegneria dell'Energia Elettrica
Ciclo XXXI

Advanced Algorithms for Flux-Weakening and Sensorless Control of Interior PM and Reluctance Synchronous Motor Drives

Direttore della Scuola:
Ch.mo Prof. Paolo Colombo

Coordinatore d'Indirizzo:
Prof. Roberto Turri

Supervisore:
Ch.mo Prof. Silverio Bolognani

Dottoranda: Virginia Manzolini

30 Settembre 2018

Contents

Preface

This Preface describes the motivation and the main contributions of the thesis. The content of each Chapter of the thesis is briefly summarized and a list of publications of the author is reported.

Background

Everyone is noting that Permanent Magnet Synchronous Machines (PMSMs) are more and more invading home, commercial and industrial applications thanks to their superior performance and efficiency, high torque and power density. Due to these features, this kind of machines is widely employed in several fields of technology. In the transportation branch, electric traction based on PMSM is becoming a strong competitor with conventional propulsion systems based on either combustion engines or induction machines. Clear examples are pure and hybrid electric vehicles, trains etc... Due to the always more pressing energy label constraints, PMSM are conquering the market of large home appliances, e.g. washing machines and dryers, refrigerators and air conditioner. Finally, robotics and high precision systems, machine tool and industrial applications are always more employing PMSM for high performance and efficiency devices.

In recent years there has been a growing interest in Synchronous Reluctance Machines (SyRMs) since they feature superior reliability and are cost effective due to the absence of permanent magnets in the rotor. Due to these relevant characteristics, the possibility of replacing PMSM with SyRMs in existing applications is very attractive for people working in all the aforementioned fields.

The motivations of this thesis are driven by industrial needs. In particular, the topics of this research have been developed according to specific requirements provided by E.E.I. S.p.a. (Equipaggiamenti Elettronici Industriali - Vicenza, Italy), the industrial partner that has been supporting the scholarship of my PhD. Two main research themes have been determined regarding the control of synchronous machines, in particular IPMSMs and SyRMs. First, the possibility to develop a control algorithm able to exploit the wide speed range operation capability of the machine. This is a crucial aspect in the design of an electric drive that allows avoiding the oversizing of both the power converter and the motor, which in turn brings to space and money savings. The second topic consists in the analysis of open research topics regarding the sensorless control of PMSM. Position estimation algorithms allow avoiding the use of position

sensors leading to advantages in term of cost and reliability of the drive. For these reasons sensorless applications are very attractive from an industrial point of view. However, the performances of conventional algorithms for the position estimation at zero or low speed degrade in case of heavy saturation condition and they could be prone to instability. According to the industrial partner requirements, all the developed solutions have to: (i.) result in an ease of application, (ii.) support the implementation in low cost systems such as DSP and (iii.) be easily combined with well-established industrial techniques.

In SyRMs the rotor saliency leads to an easy flux-weakening feature which can be exploited for wide speed range operation. For this purpose, a control scheme able to drive the machine into Maximum Torque Per Ampere (MTPA), Flux-Weakening (FW) and Maximum Torque Per Voltage (MTPV) operations has to be used. Robustness and reliability are very important feature for a control algorithm for electric drives due to the nature of the different applications, e.g. traction or home appliances, in which it has to be used. Moreover, to be considered for industrial application it has to be simple and apt for real-time applications. For these reasons a cascade structure of speed and current regulators with Current Vector Control (CVC) is the main choice in a great number of industrial applications. However, in literature the majority of the works that propose a control algorithm able to control a reluctance machine also in all the aforementioned operations are based on Direct Torque Control (DTC) or Model Predictive Control (MPC). The DTC based solutions are characterized by high computational burden, deterioration of the performance at high speed and all drawbacks typical of DTC, such as the high current ripple. MPC algorithms rely on a precise knowledge of the machine model and parameter in order to obtain a reliable and robust drive with good performance. In SyRM the iron saturation greatly affects the inductances values therefore this issue is particularly severe. All these issues make the algorithm proposed in literature less attractive for industrial applications. Differently in Interior Permanent Magnet Synchronous Machine (IPMSM) drives CVC based FW algorithms are widely used. They feature ease of implementation and low computational burden. However, these control strategies do not allow MTPV operations since in many case it is not required in IPMSM.

One of the aims of this thesis is to study the wide speed operations of SyRMs and IPMSMs and to investigate the possibility to develop a CVC based control algorithm for the wide speed operations (including MTPV operations) of a SyRM and IPMSM drives.

To control synchronous machines, it is essential to have a precise rotor position information so usually absolute encoders or resolvers are employed. The use of position sensors entails some significant drawbacks in term of reliability and cost. Sensorless SM drives use estimated rotor position in place of the measured one and thus allow to avoid all these possible disadvantages. At standstill and low working speed the rotor position can be estimated through the injection of additional high frequency voltages in the stator winding. The presence of a high frequency rotor anisotropy is exploited for this purpose, so this estimation algorithm is particularly suitable for IPMSMs and Synchronous Reluctance Motors SyRMs. It is well known that iron saturation, and in particular cross-saturation, degrades the performance of this position estimation algorithm causing an estimation error. Moreover, this technique suffers from an ambiguity

in the d axis polarity. Sensorless SyRMs drives are not affected by this issue since reluctance machines feature a symmetrical rotor. Differently in IPMSMs the estimation algorithm is not able to determine the polarity of the magnet. A magnet polarity error can cause starting failure or temporary inverse rotation, so a d axis polarity detection is necessary for a smooth and effective starting of the motor.

Part of the research work described in this thesis is committed to study the performance of the high frequency voltage injection position estimation in case of heavily saturated machine. Since the SyRM is the most affected by iron saturation among the synchronous machines, it is a perfect case study. Different techniques with the aim of limiting the negative effects of saturation on the position estimation are analysed. Besides iron saturation allows the detection of the correct magnet polarity in IPMSMs. In particular the possibility to exploit the cross-saturation effect for the d axis polarity detection is studied.

Outline of the thesis

Hereafter, the content of the each Chapter of the thesis is briefly described:

Chapter 1 The electrical model of synchronous machines with a particular focus on the machine typologies analysed in this work, i.e. interior permanent magnet and reluctance machines, is described. At first a doubly-fed three phase machine, that is the most general representation for an electrical machine, is considered and its electrical equations are derived with the assumptions of no hysteresis and eddy currents. After that, a transformation of the system into a doubly fed two phase machine is performed. The hypothesis of magnetic linearity and a sinusoidal winding distribution have been also taken into account. Finally specific models of interior permanent magnet and reluctance synchronous machines have been developed by applying appropriate conditions on the rotor currents.

Chapter 2 The synchronous reluctance motor drive features an inherent unlimited speed range capability. To exploit this peculiar characteristic of the drive while assuring the lowest power losses and complying with current and voltage limitations, a proper control algorithm has to be used. A control strategy for wide speed range operation of the synchronous reluctance motor drives is proposed. It is based on a current vector control scheme, with conventional current loops and PWM inverter control, coupled with a novel voltage loop that exploits the polar coordinates representation of the reference current vector. A small signal analysis is carried out to verify the stability of the proposed control. Moreover the possibility to consider the iron saturation phenomenon in the control algorithm is investigated.

Chapter 3 Analogously to synchronous reluctance machines, also interior permanent magnet motors can be employed for wide speed range operation. The control strategy for reluctance motors developed in the previous chapter is extended and adapted for the interior permanent magnet machines. Also in this case the possibility to include the effect of iron saturation in the proposed control using look-up tables is analysed.

Chapter 4 At zero and low speed the rotor position estimation of anisotropic machines, such as interior permanent magnet or reluctance motors, is often obtained through the injection of high frequency voltage signals in the stator windings. An overview of this position estimation algorithm and its main features is reported. With this technique the rotor position can be estimated except for the magnet polarity, leading to control issues in permanent magnet motor drives. A polarity detection procedure able to solve this ambiguity in the estimated position is presented. It exploits the cross-saturation phenomenon so a description of the properties of the mutual differential inductance is also given.

Chapter 5 Iron saturation affects the high frequency voltage injection position estimation worsening its performance. A deep insight of the convergence of this position estimation algorithm in case of heavily saturated machines is reported. Synchronous reluctance motors are considered as a case study since this kind of machine is considerably affected by iron saturation. The convergence analysis shows that in case of heavy saturation some machines can lose their self-sensing capability due to the lack of convergence points for the estimation algorithm. Finally an overview and a comparison between different compensation methods to enhance and extend the convergence range of the position estimation has been proposed.

List of publications

Several parts of this Ph.D. thesis have been presented by the author during his Ph.D. course in international conferences and journals. Hereafter the publications are listed in a chronological order:

- **Manzolini V.** , Da Rú D. and Bolognani S., "*A new control strategy for high efficiency wide speed range synchronous reluctance motor drives*". Accepted for publication in IEEE Transactions on Industry Applications.
- Berto M., Carlet P. G., **Manzolini V.** and Alberti L., "*An effective ellipse fitting technique of the current response locus to rotating HF voltage injection in IPMSM for sensorless rotor position estimation*". In IECON 2018 - 44nd Annual Conference of the IEEE Industrial Electronics Society, Washington DC, USA, 21-23 October, 2018.
- **Manzolini V.** and Bolognani S., "*On the Rotor Position Self-sensing Capability of IPM and Reluctance Synchronous Motors*". In 2018 IEEE Symposium on Sensorless Control for Electrical Drives (SLED), Helsinki, Finland, 13-14 September, 2018.
- **Manzolini V.** , Da Rú D. and Bolognani S., "*An effective voltage control loop for a deep flux-weakening in IPM synchronous motor drives*". In 2017 IEEE Energy Conversion Congress and Exposition (ECCE), Cincinnati, Ohio USA, 1-5 October, 2017, p. 3979-3985, DOI: 10.1109/ECCE.2017.8096696.
- **Manzolini V.** , Da Rú D. and Bolognani S., "*A new control strategy for high efficiency wide speed range synchronous reluctance motor drives*". In 2017 IEEE

International Electric Machines and Drives Conference (IEMDC), Miami, Florida USA, 21-24 May, 2017, p. 1-7, DOI: 10.1109/IEMDC.2017.8002276.

- **Manzolini V.** , Morandin M. and Bolognani S., "*D-axis polarity detection for IPM synchronous motor drives by high frequency voltage injection*". In IECON 2016 - 42nd Annual Conference of the IEEE Industrial Electronics Society, Firenze, Italy, 23-26 October, 2016, p. 4325-4330, DOI: 10.1109/IECON.2016.7793082.

- **Manzolini V.** , Morandin M. and Bolognani S., "*The crowded axis of the frequency: Optimal pole/zero allocation for a full speed sensorless synchronous motor drives*". In 2016 IEEE Energy Conversion Congress and Exposition (ECCE), Milwaukee, Wisconsin USA, 18-22 September, 2016, p. 1-8, DOI: 10.1109/ECCE.2016.7855497.

- **Manzolini V.** , Darba A. and De Belie F., "*Improving the torque generation in self-sensing BLDC drives by shaping the current waveform*". In 2016 International Symposium on Power Electronics, Electrical Drives, Automation and Motion (SPEEDAM), Anacapri, Italy, 2016, pp. 510-515, DOI: 10.1109/SPEEDAM.2016.7525828

Chapter 1

Synchronous machines

To study and develop control systems and algorithms a good knowledge of the plant is required. Therefore, in case of synchronous motor drives, a deep comprehension of the electrical machines is necessary. This chapter reports an analysis of the electrical model of synchronous machines with a particular focus on the machine typologies analysed in this work, i.e. Interior Permanent Magnet and Reluctance Synchronous Machines.

1.1. Introduction

The aim of this chapter is to derive a mathematical model for Interior Permanent Magnet Synchronous Machines (IPMSMs) and of Synchronous Reluctance Machines (SyRMs). The analysis is carried out starting from the most general representation of an electrical machine and gradually adding the assumptions needed to obtain the desired model. A doubly-fed three phase machine, i.e. a machine with a three phase winding on both the stator and the rotor, is considered at first. This machine is described by mean of equations relating the stator and rotor voltages with the currents and fluxes. The only assumptions made at this stage of the analysis are no hysteresis and no eddy currents. Furthermore the equations of a doubly-fed two phase machine are obtained by mean of a transformation of the three phase system into a two phase system. No further assumptions are included to achieve this representation of the machine. Both the doubly-fed three phase and the doubly-fed two phase machine models are initially obtained with no assumptions on the magnetic behaviour of the machine, i.e. using a general relationship between flux and currents. Later the hypothesis of linearity of the machine is introduced neglecting the iron saturation phenomenon. The machine flux depends also on the rotor position. To further simplify the machine flux behaviour the assumption of sinusoidally distributed windings is introduced, leading to a sinusoidal variation of the flux linkage with the rotor position. Finally, specific models for interior permanent magnet machines and for reluctance machines are derived through the assumption of appropriate conditions on the rotor currents.

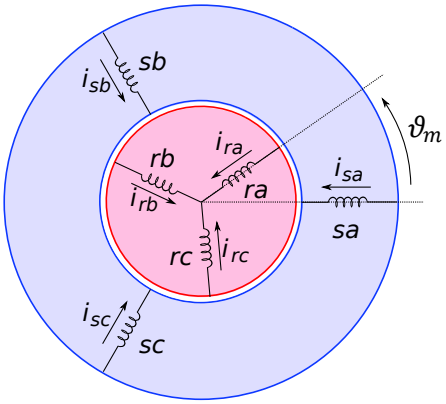

Figure 1.1: Doubly fed three phase machine representation

1.2. General model of the doubly-fed three phase machine

The general machine considered in this section, presents a three phase winding on both the stator and the rotor as shown in Figure 1.1. The mechanical position of the rotor ϑ_m is identified with the angle between the phase a of the stator, sa, and that of the rotor, ra. In case of machines with more than one pole pair, i.e. $p > 1$, the electrical position can be defined as $\vartheta_{me} = p\vartheta_m$. Analogously, the mechanical speed of the rotor, ω_m, and the electrical speed, ω_{me}, are related through $\omega_{me} = p\omega_m$. The electrical equations relating the voltages u, the currents i and the flux linkages λ are reported in (1.1) where $\bar{u}_s = [u_{sa}\, u_{sb}\, u_{sc}]^{\mathrm{T}}$, $\bar{i}_s = [i_{sa}\, i_{sb}\, i_{sc}]^{\mathrm{T}}$ and $\bar{\lambda}_s = [\lambda_{sa}\, \lambda_{sb}\, \lambda_{sc}]^{\mathrm{T}}$ are the stator voltage, current and flux vectors respectively.

$$\begin{aligned} \bar{u}_s &= \mathbf{R}_s \bar{i}_s + \frac{d}{dt}\bar{\lambda}_s \\ \bar{u}_r &= \mathbf{R}_r \bar{i}_r + \frac{d}{dt}\bar{\lambda}_r \end{aligned} \tag{1.1}$$

The stator resistance matrix is defined as $\mathbf{R}_s = R_s I_{3\times 3}$ where $I_{3\times 3}$ is the identity matrix.
The rotor quantities are analogously defined and indicated using the subscript r.

The set of six equations (1.1) represents the electric voltage balance of each phase. The voltage at the terminals is the sum of the resistive voltage drop and the time variation of the flux coupled with the winding taken into account. The compact expression (1.2), where $\bar{u} = [\bar{u}_s\, \bar{u}_r]^{\mathrm{T}}$, $\bar{i} = [\bar{i}_s\, \bar{i}_r]^{\mathrm{T}}$, $\bar{\lambda} = [\bar{\lambda}_s\, \bar{\lambda}_r]^{\mathrm{T}}$ are vectors with size 6×1, is used to join the stator and rotor equations.

$$\bar{u} = \mathbf{R}\bar{i} + \frac{d}{dt}\bar{\lambda} \tag{1.2}$$

The resistance matrix $\mathbf{R}$ can be written as a diagonal block matrix (1.3) where $0_{3\times 3}$ is the null matrix.

$$\mathbf{R} = \begin{bmatrix} \mathbf{R}_s & 0_{3\times 3} \\ 0_{3\times 3} & \mathbf{R}_r \end{bmatrix} \tag{1.3}$$

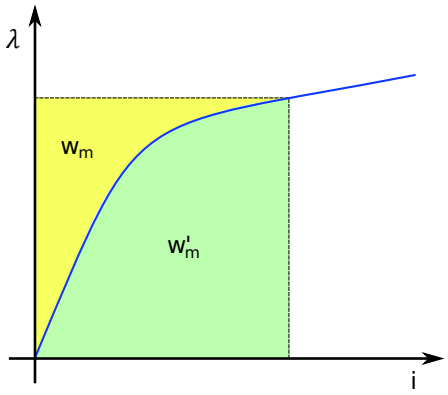

Figure 1.2: IPMSM and SyRM conventions

To develop the machine model, the assumptions of no hysteresis and eddy currents are considered. Therefore the relationships (1.4) that link the current and the flux linkage are biunivocal.

$$\begin{aligned} \bar{\lambda} = \bar{\lambda}(\bar{i}, \vartheta_{me}) &= \begin{bmatrix} \bar{\lambda}_s(\bar{i}_s, \bar{i}_r, \vartheta_{me}) \\ \bar{\lambda}_r(\bar{i}_s, \bar{i}_r, \vartheta_{me}) \end{bmatrix} \\ \bar{i} = \bar{i}(\bar{\lambda}, \vartheta_{me}) &= \begin{bmatrix} \bar{i}_s(\bar{\lambda}_s, \bar{\lambda}_r, \vartheta_{me}) \\ \bar{i}_r(\bar{\lambda}_s, \bar{\lambda}_r, \vartheta_{me}) \end{bmatrix} \end{aligned} \tag{1.4}$$

Fixed the position ϑ_{me}, the magnetic energy w_m and coenergy w'_m can be defined as in (1.5) where the indexes from 1 to 6 indicate the components of the two vectors $\bar{\lambda}$ and $\bar{i}$, i.e. $\lambda_{sa}, \lambda_{sb}, ..., \lambda_{rc}$ and $i_{sa}, i_{sb}, ..., i_{rc}$ respectively.

$$\begin{aligned} w_m(\bar{\lambda}, \vartheta_{me}) &= \int_{0,...,0}^{\lambda_1,...,\lambda_6} \sum_{k=1}^{6} i_k(\lambda_1, ..., \lambda_6, \vartheta_{me}) d\lambda_k \\ w'_m(\bar{i}, \vartheta_{me}) &= \int_{0,...,0}^{i_1,...,i_6} \sum_{k=1}^{6} \lambda_k(i_1, ..., i_6, \vartheta_{me}) di_k \end{aligned} \tag{1.5}$$

For the sake of simplicity a system with only one phase is considered at first. In this case the relationship between flux and current can be represented by the magnetization curve qualitatively reported in Figure 1.2. Energy and coenergy, expressed in (1.6) for the case of one phase, have the meaning of the two area highlighted in Figure 1.2.

$$\begin{aligned} w_m(\lambda, \vartheta_{me}) &= \int_0^{\lambda} i(\lambda, \vartheta_{me}) d\lambda \\ w'_m(i, \vartheta_{me}) &= \int_0^{i} \lambda(i, \vartheta_{me}) di \end{aligned} \tag{1.6}$$

Therefore, from geometrical considerations, (1.7) can be easily derived.

$$w_m(\lambda, \vartheta_{me}) + w'_m(i, \vartheta_{me}) = i\lambda \tag{1.7}$$

The equation can be generalised for the case of a doubly-fed three phase machine considered in this section as in (1.8).

$$w_m(\bar{\lambda}, \vartheta_{me}) + w'_m(\bar{i}, \vartheta_{me}) = \bar{i}^{\mathrm{T}} \bar{\lambda} \tag{1.8}$$

Being the flux linkage $\bar{\lambda}$ a function of currents $\bar{i}$ and position ϑ_{me}, the flux derivative in the electrical equation (1.2) can be split considering the partial derivatives with respect to current and position. The result is reported in (1.9) where $\boldsymbol{\ell}$ represents the 6×6 matrix of differential inductance in (1.10). The differential inductance represents the slope of the magnetization surface at each current value.

$$\begin{aligned} \bar{u} &= \mathbf{R}\bar{i} + \frac{\partial \bar{\lambda}}{\partial \bar{i}} \frac{d}{dt}\bar{i} + \frac{\partial \bar{\lambda}}{\partial \vartheta_{me}} \frac{d}{dt}\vartheta_{me} \\ &= \mathbf{R}\bar{i} + \boldsymbol{\ell}\frac{d}{dt}\bar{i} + \frac{\partial \bar{\lambda}}{\partial \vartheta_{me}}\omega_{me} \end{aligned} \tag{1.9}$$

$$\frac{\partial \bar{\lambda}}{\partial \bar{i}} = \boldsymbol{\ell}(\bar{i}, \vartheta_{me}) = \begin{bmatrix} \frac{\partial \lambda_{sa}}{\partial i_{sa}} & \cdots & \frac{\partial \lambda_{sa}}{\partial i_{rc}} \\ \vdots & \ddots & \vdots \\ \frac{\partial \lambda_{rc}}{\partial i_{sa}} & \cdots & \frac{\partial \lambda_{rc}}{\partial i_{rc}} \end{bmatrix} \tag{1.10}$$

The energy balance can be obtained by multiplying (1.2) or equivalently (1.9) by $\bar{i}^{\mathrm{T}}dt$. The result is reported in (1.11) where dw_{in} is the input electrical energy, dw_J is the Joule loss component, dw_m is the variation of the magnetic energy stored in the system (as defined in the first of (1.5)) and thus dw_{em} is energy converted from electrical to mechanical. The last term corresponds to the output mechanical work under the assumption of no mechanical losses.

$$\underbrace{\bar{i}^{\mathrm{T}}\bar{u}dt}_{dw_{in}} = \bar{i}^{\mathrm{T}}\mathbf{R}\bar{i}dt + \bar{i}^{\mathrm{T}}d\bar{\lambda} = \underbrace{\bar{i}^{\mathrm{T}}\mathbf{R}\bar{i}dt}_{dw_J} + \underbrace{\bar{i}^{\mathrm{T}}\frac{\partial \bar{\lambda}}{\partial \bar{i}}d\bar{i}}_{dw_m} + \underbrace{\bar{i}^{\mathrm{T}}\frac{\partial \bar{\lambda}}{\partial \vartheta_m}d\vartheta_m}_{dw_{em}} \tag{1.11}$$

Imposing $dw_{em} = Md\vartheta_m$, where M is the instantaneous torque, it is possible to write (1.12).

$$\bar{i}^{\mathrm{T}}d\bar{\lambda} = dw_m(\bar{\lambda}, \vartheta_{me}) + Md\vartheta_m \tag{1.12}$$

Since the magnetic energy is a function of stator and rotor fluxes and of the position, the infinitesimal variation dw_m can be expressed as (1.13).

$$\begin{aligned} dw_m &= \frac{\partial w_m(\bar{\lambda}, \vartheta_{me})}{\partial \lambda_{sa}}d\lambda_{sa} + ... + \frac{\partial w_m(\bar{\lambda}, \vartheta_{me})}{\partial \lambda_{ra}}d\lambda_{ra} + ... + \frac{\partial w_m(\bar{\lambda}, \vartheta_{me})}{\partial \vartheta_{me}}d\vartheta_{me} = \\ &= \frac{\partial w_m(\bar{\lambda}, \vartheta_{me})}{\partial \bar{\lambda}}d\bar{\lambda} + \frac{\partial w_m(\bar{\lambda}, \vartheta_{me})}{\partial \vartheta_{me}}d\vartheta_{me} \end{aligned} \tag{1.13}$$

Combining (1.12) and (1.13) the equation (1.14) can be written.

$$\bar{i}^{\mathrm{T}}d\bar{\lambda} - Md\vartheta_m = \frac{\partial w_m(\bar{\lambda}, \vartheta_{me})}{\partial \bar{\lambda}}d\bar{\lambda} + \frac{\partial w_m(\bar{\lambda}, \vartheta_{me})}{\partial \vartheta_{me}}d\vartheta_{me} \tag{1.14}$$

Given that the state variables are independent quantities, equation (1.14) can be divided in two components: (1.15) and (1.16). The first one represents the winding current and the second one the expression of the torque as a function of the magnetic energy.

$$\bar{i}(\bar{\lambda}, \vartheta_{me}) = \frac{\partial w_m(\bar{\lambda}, \vartheta_{me})}{\partial \bar{\lambda}} \tag{1.15}$$

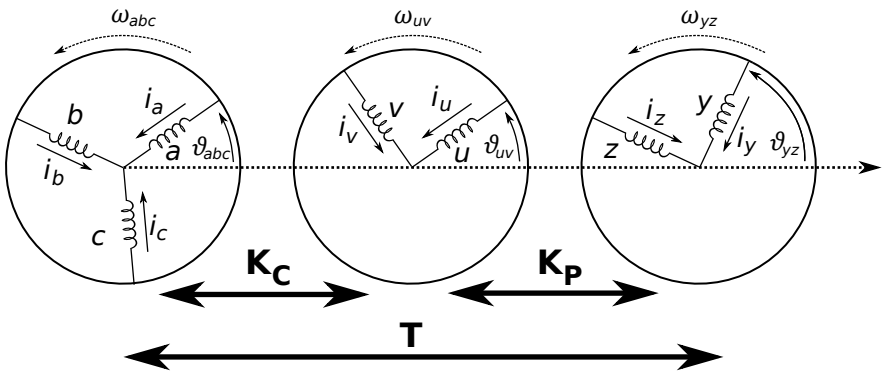

Figure 1.3: Schematic representation of Clarke and Park transformations

$$M(\bar{\lambda}, \vartheta_{me}) = -p\frac{\partial w_m(\bar{\lambda}, \vartheta_{me})}{\partial \vartheta_{me}} \tag{1.16}$$

A new expression for the torque as a function of the current $\bar{i}$ and the position ϑ_{me} can be found considering the magnetic coenergy and in particular (1.17).

$$w'_m(\bar{i}, \vartheta_{me}) = \bar{i}^{\mathrm{T}}\bar{\lambda} - w_m(\bar{\lambda}, \vartheta_{me}) \tag{1.17}$$

Differentiating (1.17) and combining it with (1.16) the torque expression (1.18) can be written.

$$M(\bar{i}, \vartheta_{me}) = p\frac{\partial w'_m(\bar{i}, \vartheta_{me})}{\partial \vartheta_{me}} \tag{1.18}$$

1.3. General model of the doubly-fed two phase machine

In the analysis of the synchronous machine, two particular transformations are widely used: the Clarke and Park transformations. A schematic representation of Clarke and Park transformation is reported in Figure 1.3. A general three-phase winding *abc* rotating with an angular speed ω_{abc} is considered. The position of the *a* phase with respect to the abscissa axis is represented with ϑ_{abc}. The Clarke transformation allows to transform the *abc* system into a two phase system *uv* characterised by the same speed and position, i.e. $\omega_{abc} = \omega_{uv}$ and $\vartheta_{abc} = \vartheta_{uv}$. In this chapter only balanced three phase systems are considered so the homopolar component is assumed to be zero. The transformation is reported in (1.19) where $\bar{f}$ is used to represent a general quantity, e.g. the voltage, the current or the flux, while subscripts *abc* and *uv* refer to the three-phase and the two-phase system respectively. The matrix $\mathbf{K}_C$, reported in (1.20), is the transformation matrix with size 2×3 while $\mathbf{K}_C^{-1}$ is the inverse matrix. It is worth highlighting that the inverse matrix can be calculated by considering the homopolar component, i.e. reintroducing the third row in the matrix $\mathbf{K}_C$ that in this way becomes an invertible square matrix. After the matrix inversion the homopolar component, i.e. the third column, is omitted again.

$$\bar{f}_{uv} = \mathbf{K}_C\bar{f}_{abc} \qquad \bar{f}_{abc} = \mathbf{K}_C^{-1}\bar{f}_{uv} \tag{1.19}$$

$$\mathbf{K}_C = \frac{2}{3}\begin{bmatrix} 1 & -\frac{1}{2} & -\frac{1}{2} \\ 0 & \frac{\sqrt{3}}{2} & -\frac{\sqrt{3}}{2} \end{bmatrix} \qquad \mathbf{K}_C^{-1} = \begin{bmatrix} 1 & 0 \\ -\frac{1}{2} & \frac{\sqrt{3}}{2} \\ -\frac{1}{2} & -\frac{\sqrt{3}}{2} \end{bmatrix} \tag{1.20}$$

The Park transformation can be used to transform the uv system into a general two phase system yz rotating with angular speed of ω_{yz}. The position of the phase y with respect to the abscissa axis is ϑ_{yz}. The transformation matrices $\mathbf{K}_P$ and $\mathbf{K}_P^{-1}$ are described in (1.22) where $\vartheta_{yz-uv} = \vartheta_{yz} - \vartheta_{uv}$.

$$\bar{f}_{yz} = \mathbf{K}_P \bar{f}_{uv} \qquad \bar{f}_{uv} = \mathbf{K}_P^{-1} \bar{f}_{yz} \tag{1.21}$$

$$\begin{aligned} \mathbf{K}_P(\vartheta_{yz-uv}) &= \begin{bmatrix} \cos(\vartheta_{yz-uv}) & \sin(\vartheta_{yz-uv}) \\ -\sin(\vartheta_{yz-uv}) & \cos(\vartheta_{yz-uv}) \end{bmatrix} \\ \mathbf{K}_P^{-1}(\vartheta_{yz-uv}) &= \begin{bmatrix} \cos(\vartheta_{yz-uv}) & -\sin(\vartheta_{yz-uv}) \\ \sin(\vartheta_{yz-uv}) & \cos(\vartheta_{yz-uv}) \end{bmatrix} \end{aligned} \tag{1.22}$$

Finally the two transformations can be combined obtaining a single matrix $\mathbf{T}$ representing the relationship between the three-phase abc and the two-phase yz systems. The transformation matrix $\mathbf{T}$ and its inverse $\mathbf{T}^{-1}$ are described in (1.24) where $\vartheta_{yz-abc} = \vartheta_{yz} - \vartheta_{abc}$.

$$\bar{f}_{yz} = \mathbf{T} \bar{f}_{abc} \qquad \bar{f}_{abc} = \mathbf{T}^{-1} \bar{f}_{yz} \tag{1.23}$$

$$\begin{aligned} \mathbf{T}(\vartheta_{yz-abc}) &= \frac{2}{3} \begin{bmatrix} \cos(\vartheta_{yz-abc}) & \cos(\vartheta_{yz-abc} - \frac{2}{3}\pi) & \cos(\vartheta_{yz-abc} + \frac{2}{3}\pi) \\ -\sin(\vartheta_{yz-abc}) & -\sin(\vartheta_{yz-abc} - \frac{2}{3}\pi) & -\sin(\vartheta_{yz-abc} + \frac{2}{3}\pi) \end{bmatrix} \\ \mathbf{T}^{-1}(\vartheta_{yz-abc}) &= \begin{bmatrix} \cos(\vartheta_{yz-abc}) & -\sin(\vartheta_{yz-abc}) \\ \cos(\vartheta_{yz-abc} - \frac{2}{3}\pi) & -\sin(\vartheta_{yz-abc} - \frac{2}{3}\pi) \\ \cos(\vartheta_{yz-abc} + \frac{2}{3}\pi) & -\sin(\vartheta_{yz-abc} + \frac{2}{3}\pi) \end{bmatrix} \end{aligned} \tag{1.24}$$

The three-phase winding on the stator and on the rotor of a doubly-fed three-phase machine can be studied considering the equivalent system yz. Starting from the equation of the three-phase winding and using (1.23), it possible to write (1.25).

$$\begin{aligned} \bar{u}_{abc} &= \mathbf{R}\bar{i}_{abc} + \frac{d}{dt}\bar{\lambda}_{abc} \\ \mathbf{T}^{-1}\bar{u}_{yz} &= \mathbf{R}\mathbf{T}^{-1}\bar{i}_{yz} + \frac{d}{dt}(\mathbf{T}^{-1}\bar{\lambda}_{yz}) \\ \mathbf{T}^{-1}\bar{u}_{yz} &= \mathbf{R}\mathbf{T}^{-1}\bar{i}_{yz} + \mathbf{T}^{-1}\frac{d}{dt}(\bar{\lambda}_{yz}) + \frac{d}{dt}(\mathbf{T}^{-1})\bar{\lambda}_{yz} \end{aligned} \tag{1.25}$$

The derivative of the transformation matrix in (1.26) is obtained by an element-by-element derivation.

$$\begin{aligned} \frac{d}{dt}(\mathbf{T}^{-1}) &= (\omega_{yz} - \omega_{abc})\mathbf{T}^{-1}\mathbf{J} \\ &= (\omega_{yz} - \omega_{abc}) \begin{bmatrix} -\sin(\vartheta_{yz-abc}) & -\cos(\vartheta_{yz-abc}) \\ -\sin(\vartheta_{yz-abc} - \frac{2}{3}\pi) & -\cos(\vartheta_{yz-abc} - \frac{2}{3}\pi) \\ -\sin(\vartheta_{yz-abc} + \frac{2}{3}\pi) & -\cos(\vartheta_{yz-abc} + \frac{2}{3}\pi) \end{bmatrix} \end{aligned} \tag{1.26}$$

The matrix $\mathbf{J}$ used in (1.26) is defined in (1.27).

$$\mathbf{J} = \begin{bmatrix} 0 & -1 \\ 1 & 0 \end{bmatrix} \tag{1.27}$$

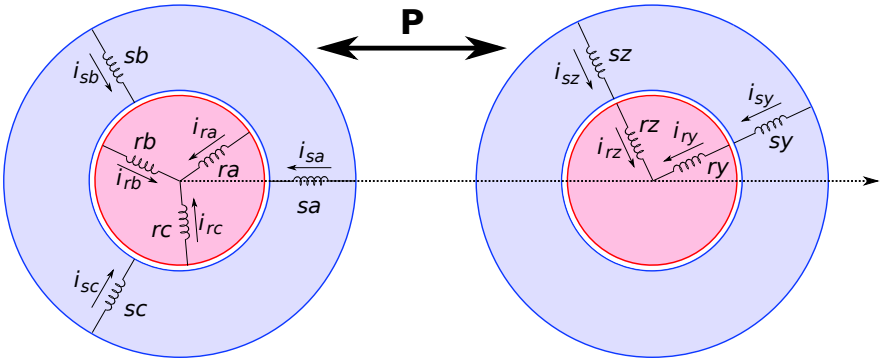

Figure 1.4: Transformation to the doubly fed two phase machine

Combining (1.25) and (1.26), it is possible to write (1.28). It is worth mentioning that (1.28) is valid for both the stator and the rotor. They can be differentiated by imposing the speed of the two systems, $\omega_{abc} = 0$ for the stator and $\omega_{abc} = \omega_m$ for the rotor.

$$\begin{aligned} \mathbf{T}^{-1}\bar{u}_{yz} &= \mathbf{R}\mathbf{T}^{-1}\bar{i}_{yz} + \mathbf{T}^{-1}\frac{d}{dt}(\bar{\lambda}_{yz}) + \mathbf{T}^{-1}\mathbf{J}\bar{\lambda}_{yz}(\omega_{yz} - \omega_{abc}) \\ \bar{u}_{yz} &= \mathbf{R}\bar{i}_{yz} + \frac{d}{dt}(\bar{\lambda}_{yz}) + \mathbf{J}\bar{\lambda}_{yz}(\omega_{yz} - \omega_{abc}) \end{aligned} \tag{1.28}$$

A more general expression including both the stator and the rotor equations can be derived using the transformation matrix $\mathbf{P}$. This matrix, with size 4×6, and its inverse are defined in (1.29).

$$\begin{aligned} \mathbf{P} &= \begin{bmatrix} \mathbf{T}(\vartheta_{yz}) & 0_{2\times 3} \\ 0_{2\times 3} & \mathbf{T}(\vartheta_{yz} - \vartheta_{me}) \end{bmatrix} \\ \mathbf{P}^{-1} &= \begin{bmatrix} \mathbf{T}^{-1}(\vartheta_{yz}) & 0_{3\times 2} \\ 0_{3\times 2} & \mathbf{T}^{-1}(\vartheta_{yz} - \vartheta_{me}) \end{bmatrix} \end{aligned} \tag{1.29}$$

The matrices are obtained considering the position of the stator winding equal to 0 as represented in Figure 1.4. In this way, (1.2) can be rewritten as (1.30) where the matrix $\mathbf{G}$ is defined in (1.31).

$$\begin{aligned} \bar{u}_{yz} &= \mathbf{R}\bar{i}_{yz} + \frac{d}{dt}\bar{\lambda}_{yz} + \mathbf{G}\bar{\lambda}_{yz} \\ &= \mathbf{R}\bar{i}_{yz} + \boldsymbol{\ell}_{yz}\frac{d}{dt}\bar{i}_{yz} + \frac{\partial\bar{\lambda}_{yz}}{\partial\vartheta_{yz}}\omega_{yz} + \mathbf{G}\bar{\lambda}_{yz} \end{aligned} \tag{1.30}$$

$$\mathbf{G} = \begin{bmatrix} 0 & -\omega_{yz} & 0 & 0 \\ \omega_{yz} & 0 & 0 & 0 \\ 0 & 0 & 0 & -(\omega_{yz} - \omega_{me}) \\ 0 & 0 & (\omega_{yz} - \omega_{me}) & 0 \end{bmatrix} \tag{1.31}$$

The differential inductance matrix $\boldsymbol{\ell}_{yz}$ in the yz system is a 4×4 matrix defined as in

(1.32).

$$\boldsymbol{\ell}_{yz}(\bar{i}_{yz}, \vartheta_{yz}) = \begin{bmatrix} \frac{\partial \lambda_{sy}}{\partial i_{sy}} & \cdots & \frac{\partial \lambda_{sy}}{\partial i_{rz}} \\ \vdots & \ddots & \vdots \\ \frac{\partial \lambda_{rz}}{\partial i_{sy}} & \cdots & \frac{\partial \lambda_{rz}}{\partial i_{rz}} \end{bmatrix} \tag{1.32}$$

The energy balance for a two phase machine (1.33) can be obtained multiplying (1.30) by $\bar{i}_{yz}^{\mathrm{T}} dt$.

$$\underbrace{\bar{i}_{yz}^{\mathrm{T}} \bar{u}_{yz} dt}_{\frac{2}{3} dw_{in}} = \underbrace{\bar{i}_{yz}^{\mathrm{T}} \mathbf{R} \bar{i}_{yz} dt}_{\frac{2}{3} dw_J} + \underbrace{\bar{i}_{yz}^{\mathrm{T}} d\bar{\lambda}_{yz} + \bar{i}_{yz}^{\mathrm{T}} \mathbf{G} \bar{\lambda}_{yz} dt}_{\frac{2}{3} dw_m + \frac{2}{3} dw_{em}} \tag{1.33}$$

The variation of the stored energy and the mechanical energy output can be written as (1.34). The $\frac{2}{3}$ factor has to be introduced since the transformations used in this chapter are not power conservative.

$$\frac{2}{3}(dw_m + M d\vartheta_m) = \bar{i}_{yz}^{\mathrm{T}} d\bar{\lambda}_{yz} + \bar{i}_{yz}^{\mathrm{T}} \mathbf{G} \bar{\lambda}_{yz} dt \tag{1.34}$$

The electromagnetic torque M can be expressed starting from the energy balance as in (1.35) where ω_m is the mechanical speed of the rotor, defined as $\omega_m = \omega_{me}\, p$.

$$\begin{aligned} M = {} & \frac{3}{2} \frac{1}{\omega_m} [\omega_{yz}(\lambda_{sy} i_{sz} - \lambda_{sz} i_{sy}) + (\omega_{yz} - \omega_{me})(\lambda_{ry} i_{rz} - \lambda_{rz} i_{ry})] + \\ & + \frac{3}{2} p \bar{i}_{yz}^{\mathrm{T}} \frac{\partial \bar{\lambda}_{yz}}{\partial \vartheta_{me}} - p \frac{\partial w_m(\bar{i}_{yz}, \vartheta_{me})}{\partial \vartheta_{me}} \end{aligned} \tag{1.35}$$

Besides, considering the relationship between magnetic energy and coenergy (1.36), the torque equation becomes (1.37).

$$\frac{2}{3}(w_m(\bar{\lambda}_{yz}, \vartheta_{me}) + w'_m(\bar{i}_{yz}, \vartheta_{me})) = \bar{i}_{yz}^{\mathrm{T}} \bar{\lambda}_{yz} \tag{1.36}$$

$$M = \frac{3}{2} \frac{1}{\omega_m} [\omega_{yz}(\lambda_{sy} i_{sz} - \lambda_{sz} i_{sy}) + (\omega_{yz} - \omega_{me})(\lambda_{ry} i_{rz} - \lambda_{rz} i_{ry})] + p \frac{\partial w'_m(\bar{i}_{yz}, \vartheta_{me})}{\partial \vartheta_{me}} \tag{1.37}$$

1.3.1. Reference frame synchronous with the stator

In the analysis of the synchronous machine, two particular reference frame are commonly used. The first one is the reference frame synchronous with the stator named α-β and characterised by $\omega_{\alpha\beta} = 0$. In this case, the axis representing the coil α is aligned with the phase a of the stator so $\vartheta_{\alpha\beta} = 0$. The transformation matrix $\mathbf{P}$ can be rewritten as (1.38).

$$\mathbf{P}_{\alpha\beta} = \begin{bmatrix} \mathbf{T}(0) & 0_{2\times 3} \\ 0_{2\times 3} & \mathbf{T}(-\vartheta_{me}) \end{bmatrix} \qquad \mathbf{P}_{\alpha\beta}^{-1} = \begin{bmatrix} \mathbf{T}^{-1}(0) & 0_{3\times 2} \\ 0_{3\times 2} & \mathbf{T}^{-1}(-\vartheta_{me}) \end{bmatrix} \tag{1.38}$$

Also the voltage and the torque equation can be particularised for the α-β reference frame as in (1.39) and (1.41) respectively.

$$\bar{u}_{\alpha\beta} = \mathbf{R} \bar{i}_{\alpha\beta} + \frac{d}{dt} \bar{\lambda}_{\alpha\beta} + \mathbf{G}_{\alpha\beta} \bar{\lambda}_{\alpha\beta} \tag{1.39}$$

$$\mathbf{G}_{\alpha\beta} = \begin{bmatrix} 0 & 0 & 0 & 0 \\ 0 & 0 & 0 & 0 \\ 0 & 0 & 0 & \omega_{me} \\ 0 & 0 & -\omega_{me} & 0 \end{bmatrix} \tag{1.40}$$

$$M = \frac{3}{2} p(\lambda_{r\beta} i_{r\alpha} - \lambda_{r\alpha} i_{r\beta}) + p \frac{\partial w'_m(\bar{i}_{\alpha\beta}, \vartheta_{me})}{\partial \vartheta_{me}} \tag{1.41}$$

1.3.2. Reference frame synchronous with the rotor

A second reference frame is broadly used for the study of the synchronous machines: the reference frame synchronous with the rotor, named *d-q*. It is characterised by $\omega_{dq} = \omega_{me}$ and the axis representing the coil d is aligned with the phase a of the rotor so $\vartheta_{dq} = \vartheta_{me}$. The transformation matrix $\mathbf{P}$ in the *d-q* reference frame is (1.42).

$$\begin{aligned} \mathbf{P}_{dq} &= \begin{bmatrix} \mathbf{T}(\vartheta_{me}) & 0_{2\times3} \\ 0_{2\times3} & \mathbf{T}(0) \end{bmatrix} \\ \mathbf{P}_{dq}^{-1} &= \begin{bmatrix} \mathbf{T}^{-1}(\vartheta_{me}) & 0_{3\times2} \\ 0_{3\times2} & \mathbf{T}^{-1}(0) \end{bmatrix} \end{aligned} \tag{1.42}$$

Using this transformation the voltage and the torque equation can be expressed in *d-q* as in (1.43) and (1.45) respectively.

$$\bar{u}_{dq} = \mathbf{R}\bar{i}_{dq} + \frac{d}{dt}\bar{\lambda}_{dq} + \mathbf{G}_{dq}\bar{\lambda}_{dq} \tag{1.43}$$

$$\mathbf{G}_{dq} = \begin{bmatrix} 0 & -\omega_{me} & 0 & 0 \\ \omega_{me} & 0 & 0 & 0 \\ 0 & 0 & 0 & 0 \\ 0 & 0 & 0 & 0 \end{bmatrix} \tag{1.44}$$

$$M = \frac{3}{2} p(\lambda_{sd} i_{sq} - \lambda_{sq} i_{sd}) + p \frac{\partial w'_m(\bar{i}_{dq}, \vartheta_{me})}{\partial \vartheta_{me}} \tag{1.45}$$

1.4. Model without iron saturation

In the following part of the chapter a linear machine is considered, i.e. the iron saturation is neglected. The relationship (1.4) linking flux and current represents a general curve, named magnetisation curve, that is qualitatively reported in blue in Figure 1.5 for a pair of flux and current, λ_{sa} and i_{sa} for instance, assuming null all the other currents. Differently for a linear machine the magnetisation curve is a straight line, represented in red in Figure 1.5, and (1.4) can be rewritten as in (1.46).

$$\bar{\lambda}(\bar{i}, \vartheta_{me}) = \mathbf{L}(\vartheta_{me})\bar{i} \tag{1.46}$$

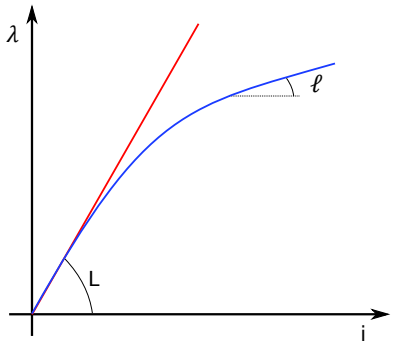

Figure 1.5: Magnetisation curve of a linear machine

The matrix $\mathbf{L}$ is the apparent inductance matrix, that depends on the position but not on the current and can be expressed as in (1.47). The submatrices are reported in (1.48).

$$\mathbf{L}(\vartheta_{me}) = \begin{bmatrix} \mathbf{L}_s(\vartheta_{me}) & \mathbf{L}_{sr}(\vartheta_{me}) \\ \mathbf{L}_{rs}(\vartheta_{me}) & \mathbf{L}_r(\vartheta_{me}) \end{bmatrix} \tag{1.47}$$

$$\begin{aligned} \mathbf{L}_s(\vartheta_{me}) &= \begin{bmatrix} L_{s,a}(\vartheta_{me}) & L_{s,ab}(\vartheta_{me}) & L_{s,ac}(\vartheta_{me}) \\ L_{s,ba}(\vartheta_{me}) & L_{s,b}(\vartheta_{me}) & L_{s,bc}(\vartheta_{me}) \\ L_{s,ca}(\vartheta_{me}) & L_{s,cb}(\vartheta_{me}) & L_{s,c}(\vartheta_{me}) \end{bmatrix} \\ \mathbf{L}_{sr}(\vartheta_{me}) = \mathbf{L}_{rs}^{\mathrm{T}}(\vartheta_{me}) &= \begin{bmatrix} L_{sr,aa}(\vartheta_{me}) & L_{sr,ab}(\vartheta_{me}) & L_{sr,ac}(\vartheta_{me}) \\ L_{sr,ba}(\vartheta_{me}) & L_{sr,bb}(\vartheta_{me}) & L_{sr,bc}(\vartheta_{me}) \\ L_{sr,ca}(\vartheta_{me}) & L_{sr,cb}(\vartheta_{me}) & L_{sr,cc}(\vartheta_{me}) \end{bmatrix} \\ \mathbf{L}_r(\vartheta_{me}) &= \begin{bmatrix} L_{r,a}(\vartheta_{me}) & L_{r,ab}(\vartheta_{me}) & L_{r,ac}(\vartheta_{me}) \\ L_{r,ba}(\vartheta_{me}) & L_{r,b}(\vartheta_{me}) & L_{r,bc}(\vartheta_{me}) \\ L_{r,ca}(\vartheta_{me}) & L_{r,cb}(\vartheta_{me}) & L_{r,c}(\vartheta_{me}) \end{bmatrix} \end{aligned} \tag{1.48}$$

From simple geometrical considerations it can be deduced that, in case of linearity, the magnetic energy and coenergy are equal. Therefore considering (1.8) $w'_m = \frac{1}{2}\bar{i}^{\mathrm{T}}\bar{\lambda}$ can be written. Finally it possible to rewrite (1.18) as in (1.49).

$$\begin{aligned} M &= \frac{1}{2}p\bar{i}^{\mathrm{T}}\frac{d\bar{\lambda}}{d\vartheta_{me}} = \frac{1}{2}p\bar{i}^{\mathrm{T}}\frac{d\mathbf{L}}{d\vartheta_{me}}\bar{i} \\ &= \underbrace{\frac{1}{2}p\bar{i}_s^{\mathrm{T}}\frac{d\mathbf{L}_s}{d\vartheta_{me}}\bar{i}_s}_{M_r} + \underbrace{p\bar{i}_s^{\mathrm{T}}\frac{d\mathbf{L}_{sr}}{d\vartheta_{me}}\bar{i}_r}_{M_{ed}} + \underbrace{\frac{1}{2}p\bar{i}_r^{\mathrm{T}}\frac{d\mathbf{L}_r}{d\vartheta_{me}}\bar{i}_r}_{M_c} \end{aligned} \tag{1.49}$$

The three torque components at the last member of the equation represents the reluctance torque M_r, the electrodynamic torque M_{ed} and the cogging torque M_c respectively. The reluctance torque M_r is related to the stator inductance matrix variations with the rotor position ϑ_{me}. The variation occurs when the rotor features an anisotropic structure due to flux barriers or pole saliencies. The electrodynamic torque M_{ed} is connected to the variation of the mutual inductances between stator and rotor windings with the rotor position. This variation is mainly due to the movement of the rotor with respect

to the stator. Finally the cogging torque M_c is due to stator anisotropies principally caused by the slots opening.

Equation (1.46) can be also written for the equivalent doubly fed two-phase machine using the transformation matrix $\mathbf{P}$ as shown in (1.50).

$$\begin{aligned} \bar{\lambda} &= \mathbf{L}(\vartheta_{me})\bar{i} \\ \mathbf{P}^{-1}\bar{\lambda}_{yz} &= \mathbf{L}(\vartheta_{me})\mathbf{P}^{-1}\bar{i}_{yz} \\ \bar{\lambda}_{yz} &= \underbrace{\mathbf{P}\mathbf{L}(\vartheta_{me})\mathbf{P}^{-1}}_{\mathbf{L}_{yz}}\bar{i}_{yz} \end{aligned} \tag{1.50}$$

$\mathbf{L}_{yz}$ can be split in different submatrices as in (1.51). These matrices are not explicitly written since it does not add useful information.

$$\mathbf{L}_{yz}(\vartheta_{me}) = \begin{bmatrix} \mathbf{L}_{s,yz}(\vartheta_{me}) & \mathbf{L}_{sr,yz}(\vartheta_{me}) \\ \mathbf{L}_{rs,yz}(\vartheta_{me}) & \mathbf{L}_{r,yz}(\vartheta_{me}) \end{bmatrix} \tag{1.51}$$

As previously shown for the three-phase machine, the torque equation of an equivalent two-phase machine (1.37) assumes a particular form in case of linearity. In particular, considering the relationship (1.36) between the magnetic energy and coenergy and that they are equal $w'_m = \frac{3}{4}\bar{i}_{yz}^{\mathrm{T}}\bar{\lambda}_{yz}$ can be written. Taking into account this last equation it is possible to obtain (1.52) from (1.37).

$$\begin{aligned} M = {} & \frac{3}{2}\frac{1}{\omega_m}[\omega_{yz}(\lambda_{sy}i_{sz} - \lambda_{sz}i_{sy}) + (\omega_{yz} - \omega_{me})(\lambda_{ry}i_{rz} - \lambda_{rz}i_{ry})] \\ & + \frac{3}{4}p\bar{i}_{s,yz}^{\mathrm{T}}\frac{d\mathbf{L}_{s,yz}}{d\vartheta_{me}}\bar{i}_{s,yz} + \frac{3}{2}p\bar{i}_{s,yz}^{\mathrm{T}}\frac{d\mathbf{L}_{sr,yz}}{d\vartheta_{me}}\bar{i}_{r,yz} + \frac{3}{4}p\bar{i}_{r,yz}^{\mathrm{T}}\frac{d\mathbf{L}_{r,yz}}{d\vartheta_{me}}\bar{i}_{r,yz} \end{aligned} \tag{1.52}$$

It is worth restating that the equations of the linear two-phase machine are expressed in yz and therefore are general and can be particularised for every choice of the reference frame. In particular the apparent inductance matrices in the stator $\mathbf{L}_{\alpha\beta}$ (1.53) and rotor $\mathbf{L}_{dq}$ (1.54) reference frame can be calculated using the appropriate matrices $\mathbf{P}$, (1.38) and (1.42) respectively.

$$\mathbf{L}_{\alpha\beta}(\vartheta_{me}) = \begin{bmatrix} \mathbf{L}_{s,\alpha\beta}(\vartheta_{me}) & \mathbf{L}_{sr,\alpha\beta}(\vartheta_{me}) \\ \mathbf{L}_{rs,\alpha\beta}(\vartheta_{me}) & \mathbf{L}_{r,\alpha\beta}(\vartheta_{me}) \end{bmatrix} \tag{1.53}$$

$$\mathbf{L}_{dq}(\vartheta_{me}) = \begin{bmatrix} \mathbf{L}_{s,dq}(\vartheta_{me}) & \mathbf{L}_{sr,dq}(\vartheta_{me}) \\ \mathbf{L}_{rs,dq}(\vartheta_{me}) & \mathbf{L}_{r,dq}(\vartheta_{me}) \end{bmatrix} \tag{1.54}$$

Also the torque can be expressed in α-β and d-q obtaining (1.55) and (1.56) respectively

$$\begin{aligned} M = {} & \frac{3}{2}p(\lambda_{r\beta}i_{r\alpha} - \lambda_{r\alpha}i_{r\beta}) \\ & + \frac{3}{4}p\bar{i}_{s,\alpha\beta}^{\mathrm{T}}\frac{d\mathbf{L}_{s,\alpha\beta}}{d\vartheta_{me}}\bar{i}_{s,\alpha\beta} + \frac{3}{2}p\bar{i}_{s,\alpha\beta}^{\mathrm{T}}\frac{d\mathbf{L}_{sr,\alpha\beta}}{d\vartheta_{me}}\bar{i}_{r,\alpha\beta} + \frac{3}{4}p\bar{i}_{r,\alpha\beta}^{\mathrm{T}}\frac{d\mathbf{L}_{r,\alpha\beta}}{d\vartheta_{me}}\bar{i}_{r,\alpha\beta} \end{aligned} \tag{1.55}$$

$$\begin{aligned} M = {} & \frac{3}{2}p(\lambda_{sd}i_{sq} - \lambda_{sq}i_{sd}) \\ & + \frac{3}{4}p\bar{i}_{s,dq}^{\mathrm{T}}\frac{d\mathbf{L}_{s,dq}}{d\vartheta_{me}}\bar{i}_{s,dq} + \frac{3}{2}p\bar{i}_{s,dq}^{\mathrm{T}}\frac{d\mathbf{L}_{sr,dq}}{d\vartheta_{me}}\bar{i}_{r,dq} + \frac{3}{4}p\bar{i}_{r,dq}^{\mathrm{T}}\frac{d\mathbf{L}_{r,dq}}{d\vartheta_{me}}\bar{i}_{r,dq} \end{aligned} \tag{1.56}$$

1.5. Sinusoidally distributed windings

In AC machines, the stator windings are designed to enhance the fundamental component of the airgap flux distribution. Ideally, if the winding has a sinusoidal distribution around the airgap, the resulting flux linkage is sinusoidal with the rotor position. In the following part sinusoidally distributed windings are analysed. Differently from the previous part of the chapter this section will focus only on a single three phase winding, the stator one. This choice was made because later the models of two synchronous machines featuring only stator winding will be presented. The hypothesis of linearity has also been considered.

Under the assumption of distributed windings, the 3×3 inductance matrix can be expressed as (1.57) where $L_\Sigma = (L_q + L_d)/2$ and $L_\Delta = (L_q - L_d)/2$.

$$\mathbf{L} = \frac{2}{3}\begin{bmatrix} L_\Sigma - L_\Delta\cos(2\vartheta_{me}) & -\frac{L_\Sigma}{2} - L_\Delta\cos(2\vartheta_{me}+\frac{4\pi}{3}) & -\frac{L_\Sigma}{2} - L_\Delta\cos(2\vartheta_{me}-\frac{4\pi}{3}) \\ -\frac{L_\Sigma}{2} - L_\Delta\cos(2\vartheta_{me}+\frac{4\pi}{3}) & L_\Sigma - L_\Delta\cos(2\vartheta_{me}-\frac{4\pi}{3}) & -\frac{L_\Sigma}{2} - L_\Delta\cos(2\vartheta_{me}) \\ -\frac{L_\Sigma}{2} - L_\Delta\cos(2\vartheta_{me}-\frac{4\pi}{3}) & -\frac{L_\Sigma}{2} - L_\Delta\cos(2\vartheta_{me}) & L_\Sigma - L_\Delta\cos(2\vartheta_{me}+\frac{4\pi}{3}) \end{bmatrix} \tag{1.57}$$

Assuming a general expression for the current as in (1.58), the flux can be calculated using (1.46). The resulting flux is described in (1.59) demonstrating that with the inductance matrix that has been considered the airgap flux distribution is sinusoidal.

$$\bar{i}_s = \begin{bmatrix} I\cos(\vartheta_{me} - \gamma + \frac{\pi}{2}) \\ I\cos(\vartheta_{me} - \gamma + \frac{\pi}{2} - \frac{2\pi}{3}) \\ I\cos(\vartheta_{me} - \gamma + \frac{\pi}{2} + \frac{2\pi}{3}) \end{bmatrix} \tag{1.58}$$

$$\bar{\lambda}_s = \begin{bmatrix} -I(L_\Sigma\sin(\vartheta_{me} - \gamma) + L_\Delta\sin(\vartheta_{me} + \gamma)) \\ -I(L_\Sigma\sin(\vartheta_{me} - \gamma - \frac{2\pi}{3}) + L_\Delta\sin(\vartheta_{me} + \gamma - \frac{2\pi}{3})) \\ -I(L_\Sigma\sin(\vartheta_{me} - \gamma + \frac{2\pi}{3}) + L_\Delta\sin(\vartheta_{me} + \gamma + \frac{2\pi}{3})) \end{bmatrix} \tag{1.59}$$

As previously done, the flux equation can be similarly derived for the equivalent two phase machine. In particular, by applying the Clarke transformation to (1.57) it is possible to express the inductance matrix in the stationary reference frame, obtaining (1.60).

$$\mathbf{L}_{\alpha\beta} = \begin{bmatrix} L_\Sigma - L_\Delta\cos(2\vartheta_{me}) & -L_\Delta\sin(2\vartheta_{me}) \\ -L_\Delta\sin(2\vartheta_{me}) & L_\Sigma + L_\Delta\cos(2\vartheta_{me}) \end{bmatrix} \tag{1.60}$$

The flux linkage can be obtained starting from (1.60) and (1.61) according to (1.50).

$$\bar{i}_{s,\alpha\beta} = \begin{bmatrix} -I\sin(\vartheta_{me} - \gamma) \\ I\cos(\vartheta_{me} - \gamma) \end{bmatrix} \tag{1.61}$$

$$\bar{\lambda}_{s,\alpha\beta} = \begin{bmatrix} I(-L_q\cos(\gamma)\sin(\vartheta_{me}) + L_d\sin(\gamma)\cos(\vartheta_{me})) \\ I(L_q\cos(\gamma)\cos(\vartheta_{me}) + L_d\sin(\gamma)\sin(\vartheta_{me})) \end{bmatrix} \tag{1.62}$$

Similarly, the equation of the two phase machine can be derived applying the Park transformation, i.e. expressing the quantities in the reference frame rotating synchronously with the rotor. The inductance matrix obtained with this transformation is

described in (1.63).

$$\mathbf{L}_{dq} = \begin{bmatrix} L_d & 0 \\ 0 & L_q \end{bmatrix} \tag{1.63}$$

In the *d-q* reference frame, the currents can be expressed as in (1.64). Finally, the flux linkage can be expressed as the product between (1.63) and (1.64), resulting in (1.65).

$$\bar{i}_{s,dq} = \begin{bmatrix} I\sin(\gamma) \\ I\cos(\gamma) \end{bmatrix} = \begin{bmatrix} I_d \\ I_q \end{bmatrix} \tag{1.64}$$

$$\bar{\lambda}_{s,dq} = \begin{bmatrix} IL_d\sin(\gamma) \\ IL_q\cos(\gamma) \end{bmatrix} = \begin{bmatrix} I_dL_d \\ I_qL_q \end{bmatrix} \tag{1.65}$$

In this case, i.e. with a sinusoidal winding distribution at the airgap, the self inductances are constant and the mutual inductances $L_{dq} = L_{qd}$ are null in the *d-q* reference.

It is worth noticing that (1.59), (1.62) and (1.65) take into account only the flux component generated by the stator three-phase winding itself. If a machine with a winding or a magnet in the rotor is analysed the flux component generated by the interaction between rotor and stator has to be added in the equations.

1.6. Interior permanent magnet machine

The IPM machine is a particular electrical machine which has permanent magnet on the rotor in place of the winding as shown in Figure 1.6 where a representation of an IPM rotor is reported. The model to describe an interior permanent magnet (IPM) synchronous machine is obtained by setting the excitation currents to represent the presence of the rotor magnets. It follows that, in the *dq* reference frame, the current vector is:

$$\bar{i}_{r,dq} = \begin{bmatrix} I_{mg} \\ 0 \end{bmatrix} \tag{1.66}$$

In (1.66) I_{mg} represents the rotor current required to produce a rotor flux linked with the stator windings equal to the magnet flux. The electrical equations can be expressed for the stator only as in (1.67) since the absence of rotor windings in this kind of machine.

$$\begin{aligned} u_{sd} &= R_s i_{sd} + \frac{d\lambda_{sd}}{dt} - \omega_{me}\lambda_{sq} \\ u_{sq} &= R_s i_{sq} + \frac{d\lambda_{sq}}{dt} + \omega_{me}\lambda_{sd} \end{aligned} \tag{1.67}$$

In case of linearity the flux and current relationship can be expressed as (1.68) according to (1.66).

$$\begin{aligned} \lambda_{sd} &= L_{s,dd}i_{sd} + L_{s,dq}i_{sq} + L_{sr,dd}I_{mg} \\ \lambda_{sq} &= L_{s,qd}i_{sd} + L_{s,qq}i_{sq} + L_{sr,qd}I_{mg} \end{aligned} \tag{1.68}$$

When a sinusoidal distribution of the windings is considered the flux equations can be further simplified as in (1.69) where $\Lambda_{mg} = L_{sr,dd}I_{mg}$ is used to indicate the magnet

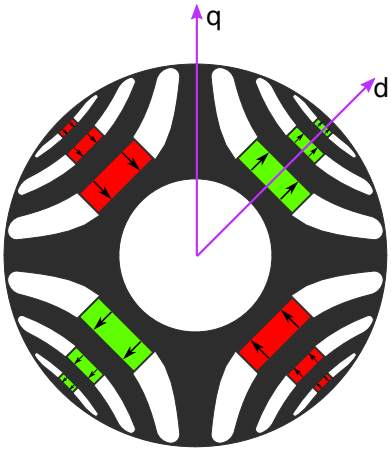

Figure 1.6: Rotor of a IPM machine

flux. The subscript s has been neglected since all the currents and fluxes refer to the stator.

$$\begin{aligned} \lambda_d &= L_d i_d + \Lambda_{mg} \\ \lambda_q &= L_q i_q \end{aligned} \tag{1.69}$$

The torque of the IPM machine can be expressed as (1.70) according to (1.66).

$$\begin{aligned} M = &\frac{3}{2} p(\lambda_{sd} i_{sq} - \lambda_{sq} i_{sd}) \\ &+ \frac{1}{2} p \frac{dL_{sd}}{d\vartheta_{me}} i_{sd}^2 + p \frac{dL_{sdq}}{d\vartheta_{me}} i_{sd} i_{sq} + \frac{1}{2} p \frac{dL_{sq}}{d\vartheta_{me}} i_{sq}^2 + \frac{1}{2} p \frac{dL_{srdd}}{d\vartheta_{me}} i_{sd} I_{mg} \\ &+ \frac{1}{2} p \frac{dL_{srdq}}{d\vartheta_{me}} i_{sq} I_{mg} + \frac{1}{2} p \frac{dL_{rdd}}{d\vartheta_{me}} I_{mg}^2 \end{aligned} \tag{1.70}$$

For a machine with sinusoidally distributed windings, since the inductances are constant or null the terms containing their derivative are null.

$$\begin{aligned} M &= \frac{3}{2} p[\Lambda_{mg} i_q + (L_d - L_q) i_d i_q] \\ &= \frac{3}{2} p \Lambda_{mg} i_q + \frac{3}{2} p (L_d - L_q) i_d i_q \end{aligned} \tag{1.71}$$

It is worth noticing that the torque of an IPM machine can be divided in two components. The former represents the electrodynamic torque produced by the interaction of the magnet flux linkage with the stator windings. The latter is a reluctance torque components generated by the anisotropic structure of the rotor of the IPM machine which is caused by the magnets insertion.

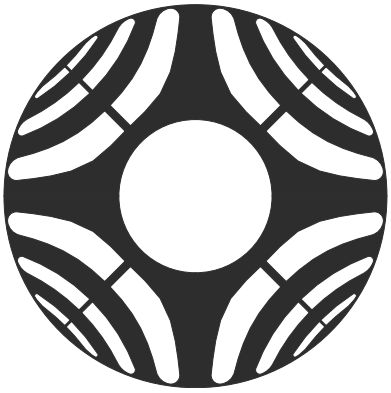

Figure 1.7: Rotor of a synchronous reluctance machine

1.7. Synchronous reluctance machine

A reluctance machine is a type of electric machine that has no windings or magnets on the rotor. A representation of the rotor of a SyRM is shown in Figure 1.7. The model to describe a reluctance machine is obtained setting the excitation currents of the rotor equal to zero. It follows that, in two phase system, the currents are:

$$\bar{i}_{r,dq} = \begin{bmatrix} 0 \\ 0 \end{bmatrix} \tag{1.72}$$

The electrical equations of the rotor can be neglected since the absence of rotor windings in this kind of machine. Therefore only the stator ones are reported in (1.73). The subscript s has been neglected since no rotor quantities are involved.

$$\begin{aligned} u_d &= R_s i_d + \frac{d\lambda_d}{dt} - \omega_{me}\lambda_q \\ u_q &= R_s i_q + \frac{d\lambda_q}{dt} + \omega_{me}\lambda_d \end{aligned} \tag{1.73}$$

According to (1.72) the flux and current relationship can be expressed as (1.74) and the torque as (1.75).

$$\begin{aligned} \lambda_d &= L_d i_d + L_{dq} i_q \\ \lambda_q &= L_{qd} i_d + L_q i_q \end{aligned} \tag{1.74}$$

$$\begin{aligned} M = &\frac{3}{2} p(\lambda_d i_q - \lambda_q i_d) \\ &+ \frac{1}{2} p \frac{dL_d}{d\vartheta_{me}} i_d^2 + p \frac{dL_{dq}}{d\vartheta_{me}} i_d i_q + \frac{1}{2} p \frac{dL_q}{d\vartheta_{me}} i_q^2 \end{aligned} \tag{1.75}$$

Under the hypothesis of sinusoidally distributed windings equations (1.74) and (1.75) can be further simplified.

$$\begin{aligned} \lambda_d &= L_d i_d \\ \lambda_q &= L_q i_q \end{aligned} \tag{1.76}$$

$$M = \frac{3}{2} p(L_d - L_q) i_d i_q \tag{1.77}$$

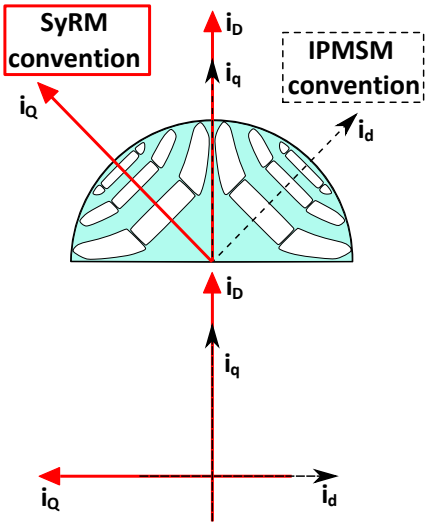

Figure 1.8: IPMSM and SyRM conventions

It can be noticed that the torque produced by a SyRM consists only on reluctance torque since no magnet or windings are present on the rotor. For this reason the rotor of the reluctance machine is intentionally designed in order to have an anisotropic structure and to feature a great difference between the

1.7.1. Synchronous reluctance d-q axes convention

A matter of lively discussion on synchronous reluctance motors is the choice of d and q axes with respect to the rotor anisotropy. Let us denote with d-q the axes normally used for an IPM motor and with D-Q those of a reluctance motor. When the reluctance motor is derived from an IPM motor by removing the permanent magnet, the d axis remains in the position where previously the permanent magnet was located and oriented, and therefore it results $L_d < L_q$. Conversely, considering the reluctance motor in itself, the D axis is naturally placed in the direction of the rotor along which the main flux occurs, and then where the reluctance is smaller, i.e. it results $L_D > L_Q$.

In this thesis the IPMSM convention is considered, i.e. the direct axis is placed along the axis of the flux barriers (where the permanent magnet could be mounted) as shown in Figure 1.8 for a four poles machine. This has been done since a control strategy described in this thesis work was initially designed for reluctance machines and after extended to the interior permanent magnet machine case. Therefore the use of the IPM convention allows a more intuitive and simple comprehension of the similarities and differences between the two cases. In Figure 1.8 the red solid axes D-Q represent the SyRM convention in which the direct axis identifies the main flux direction through the iron path and the black dotted axes d-q represent the IPMSM reference frame. The relationship linking the two systems is (1.78) and it can be easily understood looking at the lower representation in Figure 1.8. It is worth mentioning that with the considered convention, the SyRMs considered in this thesis present $L_d < L_q$.

$$i_D = i_q \qquad \text{and} \qquad i_Q = -i_d \tag{1.78}$$

1.8. Conclusions

In this chapter the models of the interior permanent magnet synchronous machines and the synchronous reluctance machine has been developed. At first, the model of a doubly-fed three phase machine featuring windings on both the stator and the rotor is considered. This is the most general representation of an electrical machine and could represent the behaviour of every kind of synchronous machine, including permanent magnet and reluctance machines. The machine model has been derived with the only assumption of no hysteresis and no eddy currents. After that, a transformation of the system into a doubly fed two phase machine is performed. The hypothesis of magnetic linearity and a sinusoidal winding distribution have been also considered. Finally specific models of IPMSM and SyRM have been developed by applying appropriate conditions on the rotor currents.

Chapter 2

Deep flux-weakening in synchronous reluctance motor drives

The synchronous reluctance motor drive features an inherent unlimited speed range capability. To exploit this particular characteristic the use of a flux-weakening strategy is necessary to drive the machine in compliance with current and voltage limits also at the higher speed. This chapter describes a control algorithm for the wide speed range operation of synchronous reluctance motor drives, including the maximum torque per voltage region.

2.1. Introduction

Synchronous reluctance machine drives exhibit an inherent unlimited speed range capability, in fact the maximum speed of this kind of machine is bounded only by mechanical limits. To exploit this peculiar characteristic of the drive while assuring the lowest power losses and complying with current and voltage limitations, a proper control algorithm has to be used. In particular, while the working speed is increasing, the control must be able to command the reluctance motor under maximum torque per ampere condition at first, into the flux-weakening region, and then along the maximum torque per voltage trajectory.

In literature the majority of the works that describe a control algorithm allowing the control of a reluctance machine also under MTPV operation are based on direct torque control [1–4]. Well-known drawbacks of DTC schemes are the high current ripple and the variable switching frequency. Besides, the control stability represents an issue and proper solutions have to be taken to prevent the performance deterioration at high speed. Moreover, some of the works mentioned so far [2–4] employ complex voltage loops based on the duty ratio monitoring [5] to drive the machine at high speed operation, increasing the computational burden of the control algorithm and making its implementation less attractive for industrial applications. Other wide-speed range solutions for SyRM based on the model predictive control can be found in literature [6,7]. MPC algorithms rely on a precise knowledge of the machine model and parameter in order to obtain good performances of the drive. This issue is particularly severe

in SyRM since the iron saturation greatly affects the inductances values. In [8, 9] a sensorless control for wide speed operation of a SyRM using direct flux vector control has been presented. The machine operation above the base speed is guaranteed by an appropriate limitation of the flux and current references according to the estimated speed of the machine. In this way the machine working point is always controlled to the intersection between the voltage and current limits, i.e. it is not able to achieve MTPV operation and exploit of the whole machine speed range. The work in [10] is an example of a current vector control scheme driving the SyRM in both FW and MTPV. The ease of CVC control structure makes this solution attractive for industrial application. However the algorithm proposed in this work decides whether to weaken the machine flux according to a SyRM model, current and speed measurement. If the machine model is not sufficiently precise the direct and quadrature current references could not be adjusted correctly according with the speed, for instance the FW could be commanded too early, leading to a reduction of the available torque before the base speed is reached, or too late, loosing the control of the machine.

To avoid this issue in interior permanent magnet synchronous machine drives the flux-weakening operation is often obtained through the feedback control of the voltage reference magnitude to a proper value [11–15]. The voltage loop is implemented together with the standard current control in the synchronous reference frame therefore it is widely used and attractive for its implementation simplicity. These techniques can be adapted to the SyRM drives; however they are not able to drive the machine into MTPV operation so they do not allow the exploitation of the whole speed range.

In this chapter, a CVC scheme, with conventional current loops and PWM inverter control, is coupled with a novel voltage loop that uses the polar coordinates representation of the reference current vector to drive reluctance machines in all the operating conditions including MTPV. The proposed voltage loop acts on both the phase and the amplitude of the reference current vector. Differently from other schemes combining a voltage loop with CVC, the proposed solution is able to exploit also the MTPV operation driving the SyRM at higher speed. The reason of this difference is that the voltage loop controls not only the phase of the current vector but even its amplitude. Besides, the algorithm is suitable for real-time applications, since it requires low computational effort in comparison with the aforementioned DTC solutions.

2.2. Proposed control scheme

The proposed control scheme is reported in Figure 2.1 and it consists of a speed control loop, two current regulators for the d and q components of the current vector and a voltage loop. The latter determines the reference working point in the i_d-i_q plane, namely the direct and quadrature current references, exploiting the polar coordinates representation of the current vector. The action of the voltage loop is twofold since it operates on (i) the amplitude and (ii) the phase by mean of two dedicated parameters. The first parameter acts on (i) modifying the limit of the speed controller output as explained in subsection 2.2.1. The second parameter manages (ii) as described in subsection 2.2.2.

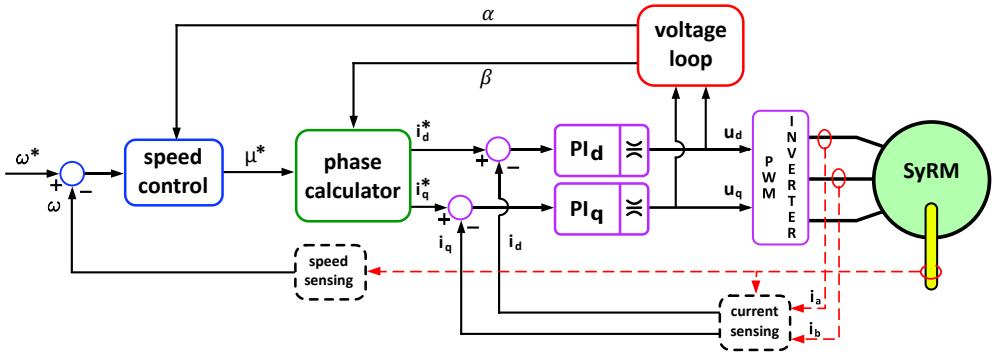

Figure 2.1: Control scheme overview.

2.2.1. Speed control

The speed controller, represented in Figure 2.2(a), provides $\mu^* = |i^*|\text{sign}(M^*)$ which is the current vector amplitude multiplied by the sign of the requested torque. The controller output μ^* is then limited between the values $\pm\alpha I_N$ where I_N is the nominal current and the parameter $\alpha \in [0;1]$ is calculated by the voltage loop. The closed-loop limitation of the speed regulator output μ^* allows the tracking of the MTPV trajectory while the observation of the voltage limit as explained in subsection 2.2.3.

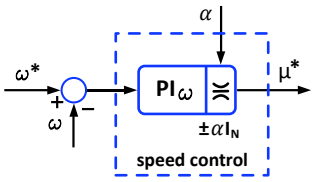

(a) Speed controller

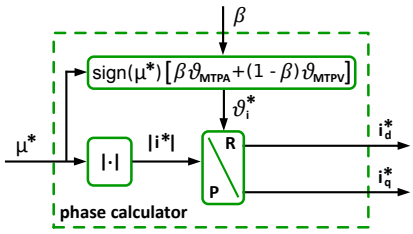

(b) Phase calculation

Figure 2.2: Schemes of the speed controller and of the phase calculation.

2.2.2. Phase calculation

A general representation of the current vector in the synchronous reference frame is $\bar{i} = i_d + \mathrm{j}i_q = |i|\mathrm{e}^{\mathrm{j}\vartheta_i}$. The MTPA and MTPV trajectories of the synchronous reluctance machine used in this chapter are reported in Figure 2.3. In the description of the control scheme a linear approximation of the machine is used. The effect of the iron saturation on the control stability and the extension of the control algorithm to a saturated machine are discussed further in subsection 2.3.3 and section 2.5 respectively. The MTPA and MTPV trajectories of a linear SyRM are straight lines through the origin and so they are univocally determined by the angles (2.1) measured between the lines themselves

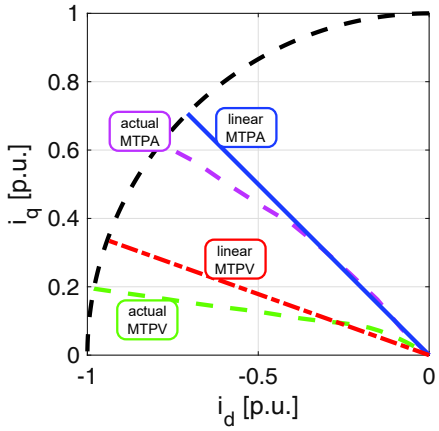

Figure 2.3: MTPA and MTPV trajectories of a saturated and a linear SyRM.

and the d axis, assuming motor operation (second quadrant of the d-q plane).

$$\begin{aligned} \vartheta_{\mathrm{MTPA}} &= \frac{3}{4}\pi \\ \vartheta_{\mathrm{MTPV}} &= \pi - \arctan\left(\frac{L_d}{L_q}\right) \end{aligned} \tag{2.1}$$

In the proposed control scheme the phase of the reference current vector is computed as in (2.2). This formulation allows working in all the lines obtained through a rotation of the MTPA towards the MTPV. In this way, the phase calculation block, represented in Figure 2.2(b), commands the MTPA, FW or MTPV operation by varying $\beta \in [0;1]$. According to the sign of μ^*, which is equal to the sign of the required torque M^*, the working point can be in the second (motor operation) or in the third (generator operation) quadrant.

$$\vartheta_i^* = \mathrm{sign}(\mu^*)\cdot[\beta\vartheta_{\mathrm{MTPA}} + (1-\beta)\vartheta_{\mathrm{MTPV}}] = \mathrm{sign}(\mu^*)[\vartheta_{\mathrm{MTPV}} + \beta(\vartheta_{\mathrm{MTPA}} - \vartheta_{\mathrm{MTPV}})] \tag{2.2}$$

Finally, given ϑ_i^* and $|i^*| = |\mu^*|$, the direct and quadrature current references can be easily calculated through a transformation from polar to Cartesian coordinates as in (2.3). It is worth highlighting that the latter is valid for both the motor and the generator operation.

$$\begin{aligned} i_d^* &= |i^*|\cos(\vartheta_i^*) \\ i_q^* &= |i^*|\sin(\vartheta_i^*) \end{aligned} \tag{2.3}$$

2.2.3. Voltage loop

The voltage control loop (Figure 2.4) is employed for the generation of proper current references that allow the transition between the different operating conditions. In particular it adjusts the d-q current references to values that are feasible at the actual operating speed. Therefore the voltage loop analyses the voltage vector amplitude, $|u|$, calculated starting from the voltage references u_d and u_q, and compares it to a limit value U_{lim}. The value of U_{lim} has to be lower than the available inverter output voltage in order to provide the necessary voltage margin during the transients.

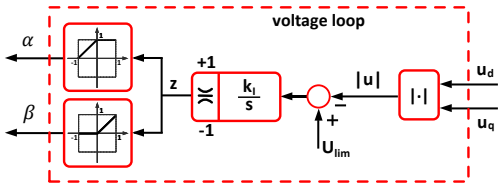

Figure 2.4: Scheme of the voltage loop.

The error $U_{\text{lim}} - |u|$ is then processed by an integral controller that generates the parameter z which is limited between ± 1. The latter is used for the calculation of the two coefficients α and β defined as in (2.4).

$$\alpha = \begin{cases} 1, & \text{if } z \geq 0 \\ 1+z, & \text{if } z < 0 \end{cases} \qquad \text{and} \qquad \beta = \begin{cases} z, & \text{if } z \geq 0 \\ 0, & \text{if } z < 0 \end{cases} \tag{2.4}$$

The parameter β is used for the rotation of the reference current vector from MTPA to MTPV, while the other coefficient, α, limits the speed controller output, as explained in subsection 2.2.2 and subsection 2.2.1 respectively. Figure 2.5 summarises the impact of the parameters z, α and β in the different working points of the direct and quadrature current plane. Until the voltage amplitude $|u|$ is lower than U_{lim}, the voltage loop integrator is saturated to its maximum $z = 1$ and then the drive is forced to operate along the MTPA line with a current amplitude depending on the required torque. When $|u|$ goes beyond the limit (for instance when the speed exceeds the base value at rated

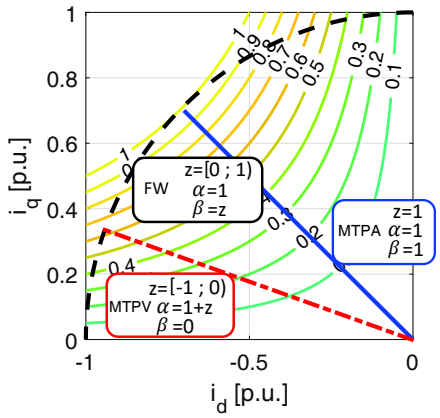

Figure 2.5: Operation of the voltage loop.

torque), the negative voltage error decreases the integrator output z and the current vector lies between MTPA and MPTV loci, the latter being reached at $z = 0$. Therefore with z ranging from 1 down to 0 the drive is commanded to work in a point of the FW region delimited by MTPA and MTPV lines and the current limit circumference according to the demanded torque. It is worth to notice that the operating point is the one exhibiting the smallest current amplitude and joule losses and then the maximum efficiency. When z ranges from 0 down to -1 the drive works on the MTPV line with a maximum current amplitude limited by z through the parameter α in order to comply with the voltage limitation.

2.3. Stability analysis

Aim of this section is to investigate the stability of the voltage control loop described in the previous section. The proposed control is highly non linear since it is based on the polar coordinate representation of the current vector. However the dynamical behaviour of the voltage control loop can be studied in the Laplace domain through a small-signal analysis and the linearisation about an operating point as suggested in [16]. Two different linear model for the flux-weakening and the MTPV operations are determined and analysed. The MTPA instead is not considered since in this working condition z, α and β are saturated to 1 and the voltage loop does not have any influence on the machine control.

2.3.1. Small-signal analysis in flux-weakening

During flux-weakening, the voltage control loop can be approximated as in Figure 2.6 considering motor operation. A first order approximation of the control delays has been considered. In particular a delay representing the effect of the inverter and of the pulse width modulation is introduced in the forward loop. Furthermore a second delay has been added in the feedback loop to take into account the discrete implementation of the control: at each execution of the control algorithm the reference voltage vector amplitude used as feedback of the voltage loop is the one calculated in the previous control cycle. Voltage and current regulators are also considered in the block scheme. Since the dynamic of electrical quantities is analysed, the rotor speed can be considered at

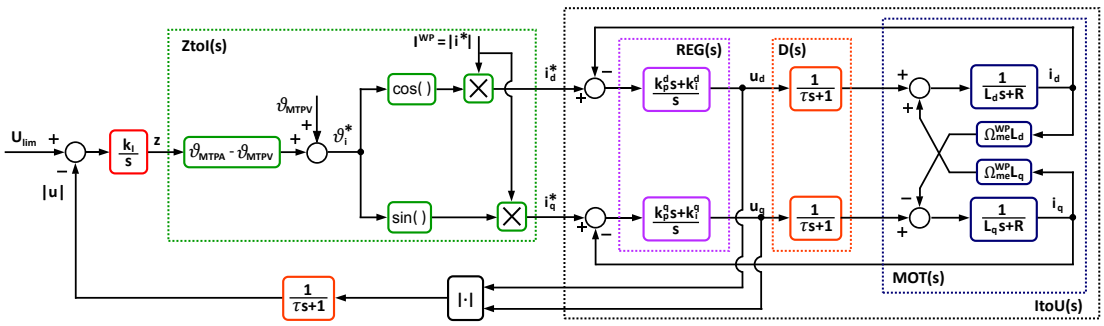

Figure 2.6: Simplified representation of the control scheme under flux-weakening operation.

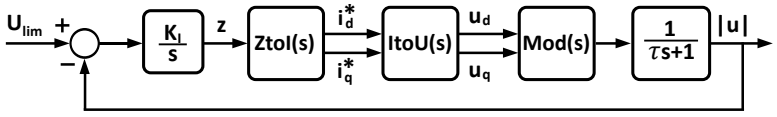

Figure 2.7: Transfer function representation of the voltage loop.

steady-state condition for the voltage loop stability analysis. So in the cross-coupling terms of the motor model represented in Figure 2.6 its value is approximated to a constant, $\Omega_{me}^{\mathrm{WP}}$. For a similar reason, during flux-weakening operations also the amplitude of the current reference space vector, $|i^*|$, can be approximated with a constant I^{WP}. In fact it is the output of the speed controller which has a slow dynamic compared to the voltage and current ones. Moreover the speed controller is often saturated during speed transients so the reference current amplitude is equal to its nominal value I_N. In the following analysis, for the sake of simplicity, it is assumed that the nominal current is required but the same results apply for different constant values of the current vector amplitude.

For the linearisation of the control scheme the working point of the machine has to be determined. Under the assumptions described so far, it can be calculated as the intersection between the current and voltage limits for each speed value $\Omega_{me}^{\mathrm{WP}}$. In particular the current vector, I^{WP}, ϑ^{WP}, and the voltage references, U_d^{WP} and U_q^{WP}, are determined.

A small variation of the control parameter z is considered. It causes, in turn, a similar variation of the current vector angle that affects the current references. The relation between the voltage loop parameter z and the current references can be expressed as in (2.5) employing a linear approximation of the sine and cosine functions. The symbol $\hat{}$ is used hereafter to indicate small variation of the signals.

$$\begin{bmatrix} \hat{i}_d^*(s) \\ \hat{i}_q^*(s) \end{bmatrix} = \underbrace{\begin{bmatrix} -(\vartheta_{\mathrm{MTPA}} - \vartheta_{\mathrm{MTPV}}) * I^{\mathrm{WP}} * \sin(\vartheta^{\mathrm{WP}}) \\ (\vartheta_{\mathrm{MTPA}} - \vartheta_{\mathrm{MTPV}}) * I^{\mathrm{WP}} * \cos(\vartheta^{\mathrm{WP}}) \end{bmatrix}}_{ZtoI(s)} \hat{z}(s) \tag{2.5}$$

The voltage references u_d and u_q are determined by the current regulators according to references and to the machine current response. Therefore to calculate the transfer function representing the interaction between the current and the voltage references, $ItoU(s)$, the machine behaviour has to be taken into account. Considering the motor electrical model in the rotor reference frame at fixed speed $\Omega_{me}^{\mathrm{WP}}$ the machine can be represented with a linear MIMO (Multiple Input Multiple Output) 2×2 dynamical system. The Laplace transfer function matrix that describes the motor is reported in (2.6).

$$\begin{bmatrix} \hat{i}_d(s) \\ \hat{i}_q(s) \end{bmatrix} = \underbrace{\begin{bmatrix} \left.\frac{\hat{i}_d(s)}{\hat{u}_d(s)}\right|_{\hat{u}_q(s)=0} & \left.\frac{\hat{i}_d(s)}{\hat{u}_q(s)}\right|_{\hat{u}_d(s)=0} \\ \left.\frac{\hat{i}_q(s)}{\hat{u}_d(s)}\right|_{\hat{u}_q(s)=0} & \left.\frac{\hat{i}_q(s)}{\hat{u}_q(s)}\right|_{\hat{u}_d(s)=0} \end{bmatrix}}_{MOT(s)} \begin{bmatrix} \hat{u}_d(s) \\ \hat{u}_q(s) \end{bmatrix} \tag{2.6}$$

$$\begin{aligned}
\left.\frac{\hat{i}_d(s)}{\hat{u}_d(s)}\right|_{\hat{u}_q(s)=0} &= \frac{L_q s + R}{L_d L_q s^2 + R(L_d + L_q)s + R^2 + (\Omega_{me}^{\mathrm{WP}})^2 L_d L_q} \\
\left.\frac{\hat{i}_d(s)}{\hat{u}_q(s)}\right|_{\hat{u}_d(s)=0} &= \frac{L_q \Omega_{me}^{\mathrm{WP}}}{L_d L_q s^2 + R(L_d + L_q)s + R^2 + (\Omega_{me}^{\mathrm{WP}})^2 L_d L_q} \\
\left.\frac{\hat{i}_q(s)}{\hat{u}_d(s)}\right|_{\hat{u}_q(s)=0} &= -\frac{L_d \Omega_{me}^{\mathrm{WP}}}{L_d L_q s^2 + R(L_d + L_q)s + R^2 + (\Omega_{me}^{\mathrm{WP}})^2 L_d L_q} \\
\left.\frac{\hat{i}_q(s)}{\hat{u}_q(s)}\right|_{\hat{u}_d(s)=0} &= \frac{L_d s + R}{L_d L_q s^2 + R(L_d + L_q)s + R^2 + (\Omega_{me}^{\mathrm{WP}})^2 L_d L_q}
\end{aligned} \tag{2.7}$$

The current regulators are PI and define the voltage references according to (2.8).

$$\begin{bmatrix} \hat{u}_d(s) \\ \hat{u}_q(s) \end{bmatrix} = \underbrace{\begin{bmatrix} \frac{k_P^d s + k_I^d}{s} & 0 \\ 0 & \frac{k_P^d s + k_I^d}{s} \end{bmatrix}}_{REG(s)} \begin{bmatrix} \hat{i}_d^*(s) - \hat{i}_d(s) \\ \hat{i}_q^*(s) - \hat{i}_q(s) \end{bmatrix} \tag{2.8}$$

The voltage applied to the machine windings are delayed with respect to the references due to the PWM calculation and the digital implementation of the control. The actual voltages can be expressed as in (2.9). A first order approximation with time constant $\tau = \frac{3}{2}T_c$ is used to represent the delay.

$$\begin{bmatrix} \hat{u}_d^{\mathrm{appl}}(s) \\ \hat{u}_q^{\mathrm{appl}}(s) \end{bmatrix} = \underbrace{\begin{bmatrix} \frac{1}{\tau s + 1} & 0 \\ 0 & \frac{1}{\tau s + 1} \end{bmatrix}}_{D(s)} \begin{bmatrix} \hat{u}_d(s) \\ \hat{u}_q(s) \end{bmatrix} \tag{2.9}$$

The closed loop transfer function of the current control loop can be calculated as in (2.10), where $I_{2\times 2}$ is the second order identity matrix.

$$\begin{bmatrix} \hat{i}_d(s) \\ \hat{i}_q(s) \end{bmatrix} = REG(s)D(s)MOT(s)\big[I_{2\times 2} + REG(s)D(s)MOT(s)\big]^{-1} \begin{bmatrix} \hat{i}_d^*(s) \\ \hat{i}_q^*(s) \end{bmatrix} \tag{2.10}$$

Substituting (2.10) into (2.8) the transfer function from the current references to the voltage ones can be calculated (2.11).

$$\begin{bmatrix} \hat{u}_d(s) \\ \hat{u}_q(s) \end{bmatrix} = \underbrace{REG(s)\big[I_{2\times 2} - REG(s)D(s)MOT(s)[I_{2\times 2} + REG(s)D(s)MOT(s)]^{-1}\big]}_{ItoU(s)} \begin{bmatrix} \hat{i}_d^*(s) \\ \hat{i}_q^*(s) \end{bmatrix} \tag{2.11}$$

A linear approximation through partial derivatives is used for the modulus function employed to calculate the voltage space vector amplitude (2.12).

$$|\hat{u}|(s) = \underbrace{\begin{bmatrix} \frac{U_d^{\mathrm{WP}}}{U_{\mathrm{lim}}} & \frac{U_q^{\mathrm{WP}}}{U_{\mathrm{lim}}} \end{bmatrix}}_{Mod(s)} \begin{bmatrix} \hat{u}_d(s) \\ \hat{u}_q(s) \end{bmatrix} \tag{2.12}$$

Finally including the voltage regulator and the feedback loop delay the voltage loop can be represented as a series of linearised transfer function Figure 2.7. For each working

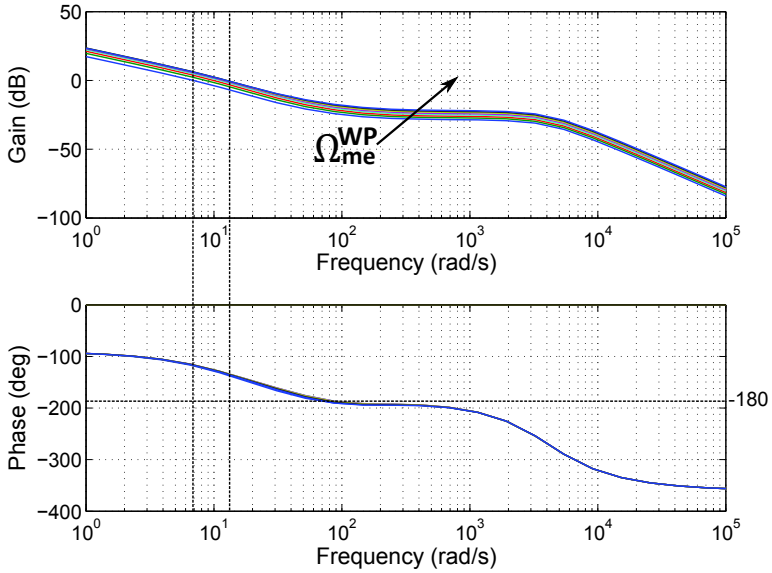

Figure 2.8: Bode diagrams of the voltage loop linearised transfer function under flux-weakening operation for different speed values.

speed the transfer function parameter can be easily calculated and thus the stability of the proposed control can be analysed.

In Figure 2.8 the Bode diagram of the voltage loop transfer function is reported for different values of the machine working speed. The open loop gain increases with the speed, however the system can be stabilised in the whole speed range by properly designing the voltage regulator. In fact in Figure 2.8 the Bode diagram is characterised by a high phase margin at every speed so the voltage loop is stable in the flux-weakening region.

2.3.2. Small-signal analysis in MTPV

The same small-signal analysis described for the flux-weakening can be carried out also for the MTPV operation of the machine. In this condition the voltage loop can be approximated as in Figure 2.9. The block scheme is the same as in the flux-weakening case except for the current reference generation part highlighted in green. In fact under flux-weakening operation the amplitude of the current vector was assumed to be constant while the phase was increasing, whereas in MTPV the amplitude is decreasing and the phase angle is fixed.

For the linearisation of the control scheme the working point of the machine has to be determined. It can be calculated for each speed value $\Omega_{me}^{\mathrm{WP}}$ as the intersection between the corresponding voltage limit ellipse and the MTPV trajectory.

A small variation of the control parameter z is considered and it causes a small reduction of the current vector amplitude according to (2.13). For the remaining part of the control loop the linearisation carried out for the flux-weakening case remains valid

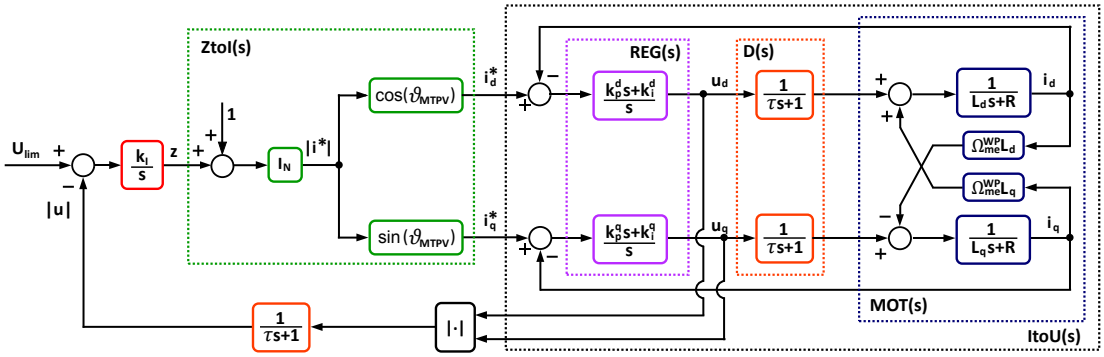

Figure 2.9: Simplified representation of the control scheme under MTPV operation.

also under MTPV operation.

$$\begin{bmatrix} \hat{i}_d^*(s) \\ \hat{i}_q^*(s) \end{bmatrix} = \underbrace{\begin{bmatrix} I^{\mathrm{WP}} * \cos(\vartheta_{\mathrm{MTPV}}) \\ I^{\mathrm{WP}} * \sin(\vartheta_{\mathrm{MTPV}}) \end{bmatrix}}_{ZtoI(s)} \hat{z}(s) \tag{2.13}$$

In Figure 2.10 the Bode diagram of the voltage loop transfer function is reported for different values of the machine working speed. In this case there is no significant variation of the open loop gain with the speed. The Bode diagram is characterised by a high phase margin so the stability of the voltage loop has been proven in every working condition.

The linearised analysis that has been presented is a useful tool for conveniently tuning voltage controller in order to achieve a stable voltage loop in the whole speed

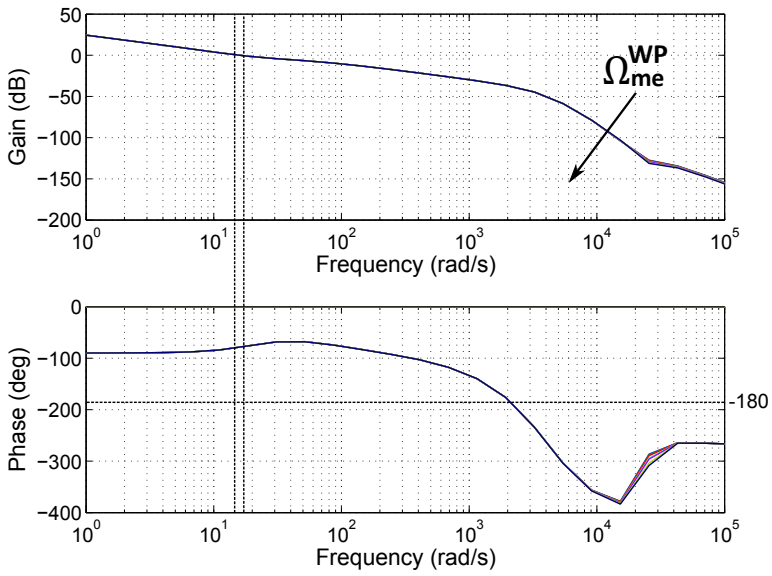

Figure 2.10: Bode diagrams of the voltage loop linearised transfer function under flux-weakening operation for different speed values.

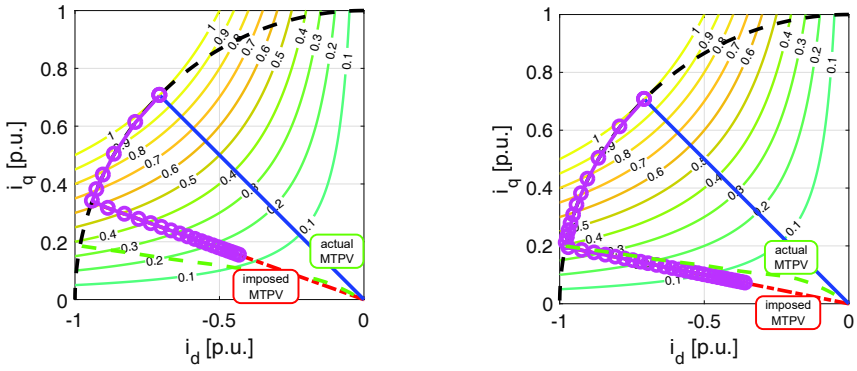

(a) $\vartheta_{\mathrm{MTPV}} = 160°$. (b) $\vartheta_{\mathrm{MTPV}} = 168°$.

Figure 2.11: Test with the motor dragged with a speed ramp with different values of $\vartheta_{\mathrm{MTPV}}$ (simulation).

range. Moreover, if necessary, this analysis can be used to design an adaptive controller, as proposed in [16].

2.3.3. Non linearities affecting the stability

Some possible causes of instability are related to non linearities of the drive therefore are not taken into account in the previous linearised analysis. First of all the voltage that can be applied to the machine is limited according to the DC-link voltage so the voltage references, i.e. the output of the current regulators, are consequently limited. Since the voltage loop is activated only when the reference voltage exceeds the voltage limit U_{lim} the latter can not be equal to the maximum available voltage U_N. On the contrary it should be chosen sufficiently lower than the available voltage in order to allow a proper control of the stator voltage amplitude. Typically about the 95% of U_N is considered. Differently if $\Delta U = U_{\mathrm{lim}} - U_N$ is not large enough the voltage loop could loose its capability of controlling promptly z. This is considered one of the main drawbacks of the feedback regulation of the voltage since it could lead to a non fully exploitation of the available DC-link voltage. However ΔU can be reduced by further increasing k_I according to the Bode diagrams.

Some FW control strategies that allow also the MTPV tracking could be prone to instability if the MTPV angle, $\vartheta_{\mathrm{MTPV}}$, used by the control algorithm greatly differs from the actual one [2] due to parameters mismatch. In synchronous reluctance machine the inductance varies greatly with the applied current so it is not unlikely that the nominal parameters give an incorrect description of the MTPV trajectory. In particular the instability may arise when $\vartheta_{\mathrm{MTPV}}$ is taken much higher than the actual one i.e. when the MTPV lies nearer to the direct axis. However if the iron saturation is neglected and a linear machine with the nominal inductance parameters is considered the resulting $\vartheta_{\mathrm{MTPV}}$ is much lower than the actual one at high current. So the machine working points are far from the instability region assuring safe operation of the drive. In Figure 2.11(a) the actual MTPV locus of the SyRM considered in this chapter is shown together with a linear MTPV trajectory obtained considering the nominal parameters of the machine. A simulation was carried out with the machine dragged with a speed ramp that starts

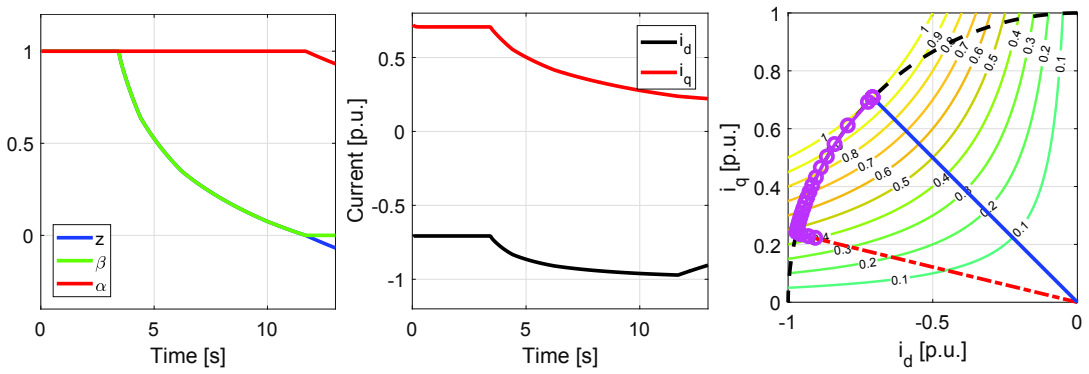

(a) Control parameters (b) d and q currents (c) Working points in i_d-i_q plane

Figure 2.12: Test with the motor dragged with a speed ramp (simulation).

from zero and goes beyond the base value. During the simulation the speed controller is artificially saturated so the maximum torque is required. It can be seen that the MTPV operation is achieved without loosing stability. In Figure 2.11(b) a different linearised MTPV is considered. It is the straight line that passes trough the intersection of the actual MTPV of the machine and the maximum current circumference. In this case part of the linearised MTPV is lower than the real one, however the test has been completed without instability issues. In order to further demonstrate the stability of this second solution, and to better approximate the real MTPV locus in the remaining part of the chapter $\vartheta_{\text{MTPV}} = 168°$ is used.

2.4. Simulation and experimental results

In order to validate the scheme proposed in the previous section a simulation model has been developed and the control algorithm has been implemented on a test bench.

The reluctance motor is a 4-poles machine with nominal torque and current of 4 Nm and 1.8 A_{pk} respectively. The value of phase resistance is $R = 15.6\ \Omega$ and the apparent inductances are equal to $L_d = 260$ mH and $L_q = 1070$ mH. The machine is fed by a voltage-source inverter controlled by a dSPACE fast-prototyping system with a DC-link voltage of $U_{\text{DC}} = 300$ V.

During the first test the machine is dragged by a master motor with a speed ramp that starts from zero and goes beyond the base value. The test is performed with the speed controller artificially saturated by imposing a reference speed higher than the operation speed, so the maximum torque is required. Both simulations and experimental measurements are carried out in this condition and the results are reported in Figure 2.12 and Figure 2.13 respectively. It is worth noticing that the MTPV operation begins at different instants in Figure 2.12(a) and Figure 2.13(a). This is due to a slight difference in the value of speed at the end of the FW between the two cases given by uncertainties in model parameters. Nevertheless a good agreement between the simulation and the experiment can be noticed. When the motor works at a speed lower than the base value all the coefficients, z, α and β, are unitary and the working point coincides with the base point since the maximum torque is required. When the speed goes beyond

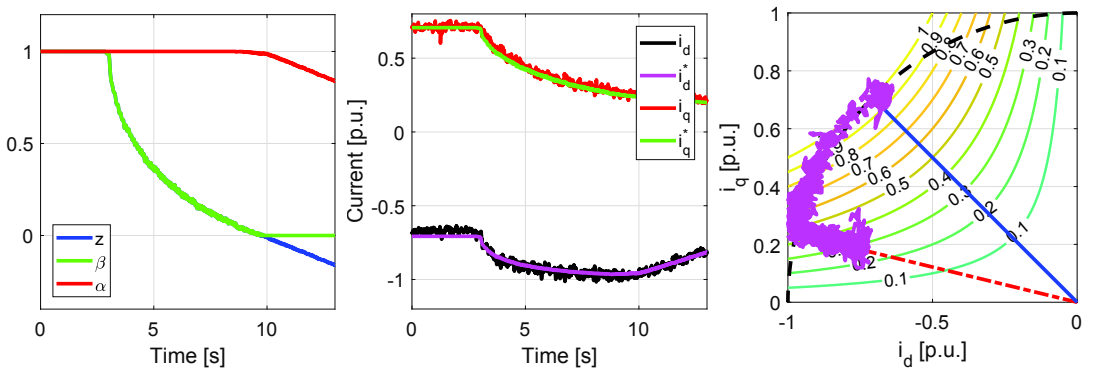

(a) Control parameters (b) d and q currents (c) Working points in i_d-i_q plane

Figure 2.13: Test with the motor dragged with a speed ramp (experimental).

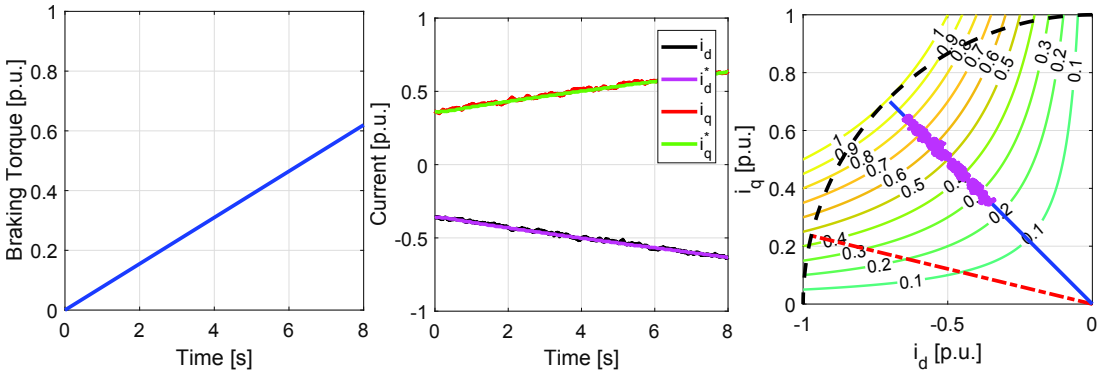

(a) Braking torque reference (b) d and q currents (c) Working points in i_d-i_q plane

Figure 2.14: Test with a braking torque ramp (experimental).

the base value, the voltage loop leads to a reduction of the parameters z, α and β so the motor flux is weakened by moving the working point along the maximum current circumference first and the MTPV later, as shown in Figure 2.12(c) and Figure 2.13(c). Therefore, both the experimental and the numerical results of the first test confirm that the proposed strategy is able to drive the machine in the different operating conditions and exploit the whole speed range. On the other hand, the results presented so far do not assure the correct operation of the voltage loop together with the speed regulator since the SyRM has been dragged by the master motor.

A second test, reported in Figure 2.14, has been carried out setting a constant speed reference to the reluctance machine drive with a value below the base speed. Then a ramp of braking torque from is provided through the master motor (Figure 2.14(a)). During this test the control parameters z, α and β are unitary so the motor works in MTPA condition. The speed is kept equal to the reference while the working point tracks the MTPA trajectory in order to provide an increasing torque and oppose the braking torque (Figure 2.14(c)).

Moreover a test with a speed ramp, reported in Figure 2.15, is performed under constant braking torque. The speed reference changes in a ramp shape from a value

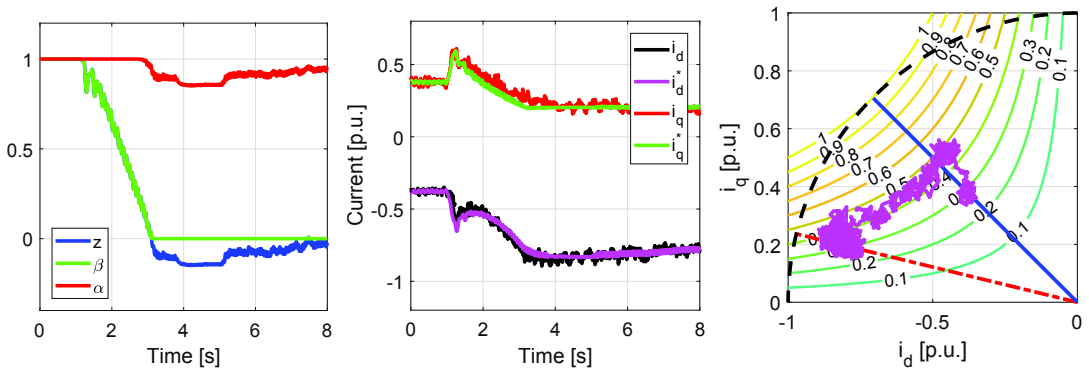

(a) Control parameters (b) d and q currents (c) Working points in i_d-i_q plane

Figure 2.15: Test with a speed ramp (experimental).

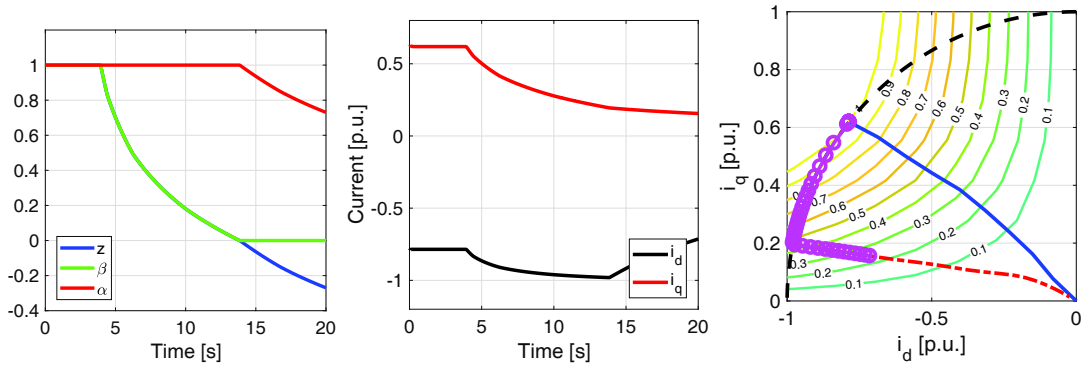

(a) Control parameters (b) d and q currents (c) Working points in i_d-i_q plane

Figure 2.16: Test with the motor dragged with a speed ramp with actual MTPA and MTPV trajectories (simulation).

lower to a value higher than the base speed. The increase of the speed causes a reduction of the control parameters z and β that determine the rotation of the reference current vector from the MTPA to the MTPV. It is worth noticing that when the speed ramp starts ($t = 1$ [s]), the working point is shifted upwards to produce an higher value of torque, namely the inertial component required to accelerate the machine. Then, the working point moves along the constant torque hyperbola up to the MTPV locus.

2.5. Extension to saturated machine

In case of saturation the MTPA and MTPV loci are deformed so ϑ_{MTPA} and ϑ_{MTPV} depend on the current amplitude as shown in (2.14) which replaces (2.1).

$$\vartheta_{\text{MTPA}} = f(|i|) \qquad \text{and} \qquad \vartheta_{\text{MTPV}} = g(|i|) \tag{2.14}$$

The curves in (2.14) can be calculated by FE analysis or measured. The proposed control strategy can be easily extended to this case given the real MTPA and MTPV curves of the machine. In particular knowing the relations described in (2.14), it is possible to

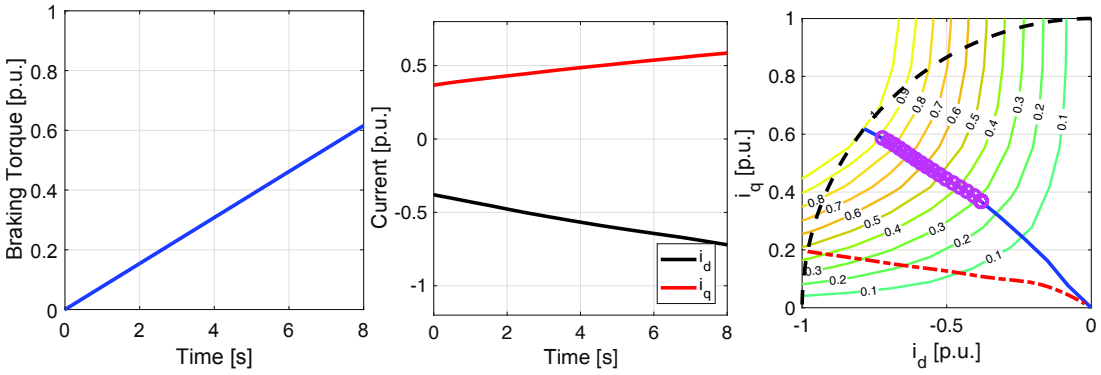

(a) Braking torque reference (b) d and q currents (c) Working points in i_d-i_q plane

Figure 2.17: Test with the motor dragged with a speed ramp with actual MTPA and MTPV trajectorie (simulation).

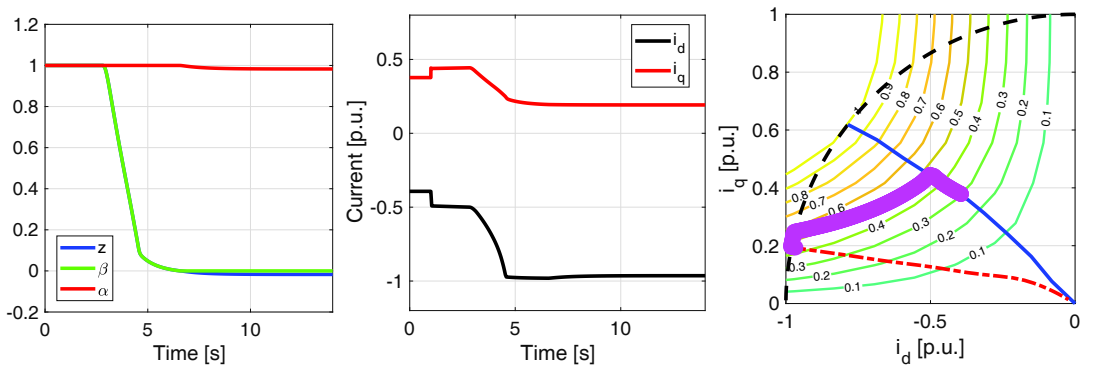

(a) Control parameters (b) d and q currents (c) Working points in i_d-i_q plane

Figure 2.18: Test with the motor dragged with a speed ramp with actual MTPA and MTPV trajectorie (simulation).

build a look up table that can be used for computing (2.2). In order to demonstrate the feasibility of the extension to the saturated model the same tests carried out in the previous section are repeated in simulation implementing the actual MTPA and MTPV curves of the SyRM. The results are reported in Figure 2.16, Figure 2.17 and Figure 2.18. The behaviour of the control algorithm is the same of the linear case but working point precisely tracks the actual MTPA and MTPV trajectories of the machine.

2.6. Conclusions

This chapter presented a control scheme for wide speed range operation of a SyRM drive that exploits the polar coordinate representation of the reference current vector. A voltage loop has been used together with CVC in the synchronous *d-q* reference frame making it perfectly suitable for integration with traditional control schemes. The resulting control algorithm is able to drive the machine in the whole speed range while achieving the lowest power losses in every working condition. Besides, the voltage and the current limits are inherently observed. Moreover the algorithm can be used both with a linear approximation of MTPA and MTPV trajectories and with the actual ones. A small signal analysis confirmed the stability of the control in every working condition. A simulation model has been developed and the proposed control algorithm has been implemented on a test bench. Both simulations and experimental tests confirmed the validity and effectiveness of the scheme. In particular it has been shown that the proposed control algorithm is able to drive the machine in MTPA, FW and MTPV allowing the exploitation of its whole operating speed range.

Chapter 3

Extended voltage loop for deep flux-weakening in IPMSM drives

Interior permanent magnet synchronous motor drive can be employed for wide speed range operation. To guarantee the maximum efficiency of the drive and exploit the whole speed range of machines with the short circuit current within the current limit, the maximum torque per voltage locus has to be tracked. This chapter extends the algorithm for wide speed range operation of reluctance machine presented in the previous chapter to the case of interior permanent magnet motor drives.

3.1. Introduction

Similarly to SyRM drives, also interior permanent magnet synchronous motor drives can be employed for wide speed range operations. Analogously to what has been described in chapter 2 for the reluctance machine, also in IPMSM drives the control should command the machine under different operating regions of the current plane. While the machine works below the base speed, the maximum efficiency is obtained along the maximum torque per ampere trajectory. Increasing the speed above the base value, the control algorithm should drive the motor along the flux-weakening region to provide the maximum available torque complying with the current limit of the drive and the voltage limit imposed by the power converter and the maximum current. An infinite speed is theoretically achievable if the origin of the voltage ellipse is within the current limit circle, as often happens in IPMSM. In this case, to exploit this inherent feature of the drive the maximum torque per voltage locus should be tracked to maximise the torque at the highest speed.

To achieve FW operation of IPMSM drive voltage control loops based on feedforward, feedback or mixed techniques are usually employed for their ease of implementation. In [17] an exhaustive description of the most common schemes is reported. In some FW strategies the output of the voltage controller acts directly on the reference current vector phase [11, 16, 18] while in other cases the rotation of the vector is obtained by changing the d current component [14]. Although the aforementioned schemes drive the machine above the base speed by weakening the flux of the permanent magnets, they

are not able to control the point of work along the MTPV trajectory. These techniques can exploit the whole speed range of the machine if its voltage ellipse origin is outside the current limit circle. However, when the origin of the voltage ellipse is within the maximum current limit the use of this FW strategies limits the theoretically infinite speed range of the drive.

In literature some works allowing the MTPV operation of IPMSM can be found. [19] and [20] propose a solution based on direct flux vector control. Two components are controlled: the flux linkage amplitude and the quadrature current. Limiting the flux linkage amplitude allows the flux-weakening while a closed loop limitation of the flux angle is used to enable the MTPV operation. Although direct flux vector control is inherently suitable for FW applications the use of this strategy would force in many industrial cases a deep modification of the existing controls based on the d and q current regulations. Besides a flux linkage observer has to be added to supply feedbacks both to the flux amplitude regulator and to the flux angle limitation.

Solutions based on a standard current vector control scheme with regulation of the d and q components of the current have been also proposed [21, 22]. These control strategies can be easily merged with the existing and wide-spread solutions. However they often rely on a linear model of the machine to determine the reference working point and the iron saturation is not taken into account. The machine operating region change is controlled by a voltage control loop as in [11,14,16,18]. Therefore these control algorithms can be considered as enhancements of the CVC based techniques allowing only FW operations.

These last solutions share some common features, such as the use of a voltage regulator, with the control for reluctance machines proposed in chapter 2. Therefore in this chapter the possibility to extend the presented scheme for SyRM to the case of an IPMSM drive is investigated. The possibility to include the effect of iron saturation in the proposed control using look-up tables is also analysed since the knowledge of the actual magnetic characteristics allows a proper current reference generation which in turn guarantees the maximum efficiency of the machine in every working condition.

3.2. Proposed control scheme

For a linear IPMSM, neglecting the resistive voltage drop, the MTPA and the MTPV loci can be expressed as in (3.1). The curves calculated with (3.1) are reported in Figure 3.1 with circular and square markers respectively.

$$\begin{aligned} i_d^{\mathrm{MTPA}}(i_q) &= \frac{-\Lambda_{mg} + \sqrt{\Lambda_{mg}^2 + 4(L_d - L_q)^2 \cdot i_q^2}}{2(L_d - L_q)} \\ i_d^{\mathrm{MTPV}}(i_q) &= -\frac{\Lambda_{mg}}{L_d} + \frac{L_q}{L_d} \cdot i_d^{\mathrm{MTPA}}(i_q) \end{aligned} \tag{3.1}$$

The proposed control scheme, reported in Figure 3.2, is based on the knowledge of the expressions (3.1). It consists of a speed regulator, two current regulators for the d and q components of the current vector and a voltage loop. The latter determines the reference point of work in the d-q current plane, namely the direct and quadrature current references. The voltage loop outputs two parameters, namely α and β both in the interval

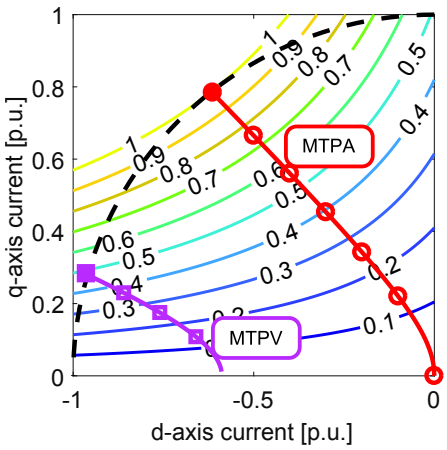

Figure 3.1: MTPA and MTPV trajectories of an IPM machine.

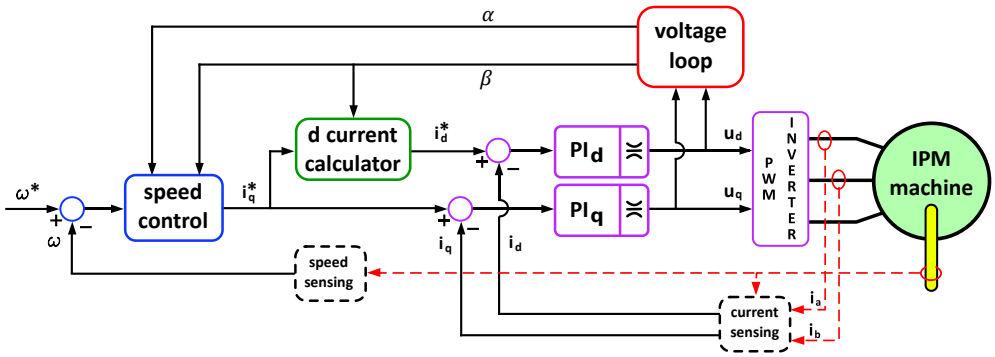

Figure 3.2: Control scheme.

$[0; 1]$. As can be seen in Figure 3.2, they act together with the speed regulator to determine the quadrature current reference and β is also used in the calculation of the direct current reference, as explained in subsection 3.2.2 and subsection 3.2.1 respectively. The detailed description of the voltage loop operation is reported in subsection 3.2.3.

3.2.1. Direct current calculation

In Figure 3.3 the scheme of the direct current calculation is reported. For a given quadrature current i_q^*, the corresponding values of the d current on the MPTA (i_d^{MTPA}) and on the MTPV (i_d^{MTPV}) curves are computed with (3.1). The direct current reference

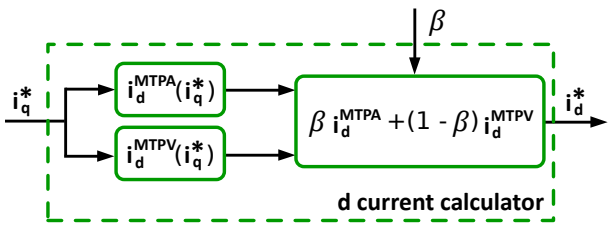

Figure 3.3: Scheme of the direct current calculation.

i_d^* is obtained as the weighted sum of the latter as shown in (3.2), where $\beta \in [0;1]$ is the parameter provided by the voltage loop. When β is equal to the upper limit the direct current reference is $i_d^* = i_d^{\mathrm{MTPA}}$, while with $\beta = 0$ the condition $i_d^* = i_d^{\mathrm{MTPV}}$ is obtained. For all the other values of β, the point of work belongs to a curve in the region delimited by the MTPA and the MTPV loci. In Figure 3.4 the current trajectory is plotted for different values of β.

$$i_d^*(\beta) = \beta \cdot i_d^{\mathrm{MTPA}} + (1-\beta) \cdot i_d^{\mathrm{MTPV}} \tag{3.2}$$

It is worth noticing that the direct current reference obtained with (3.2) could exceed the maximum current I_N bound. To avoid overheating or permanent damage of the machine, a proper limitation has to be chosen for the quadrature current as explained in subsection 3.2.2.

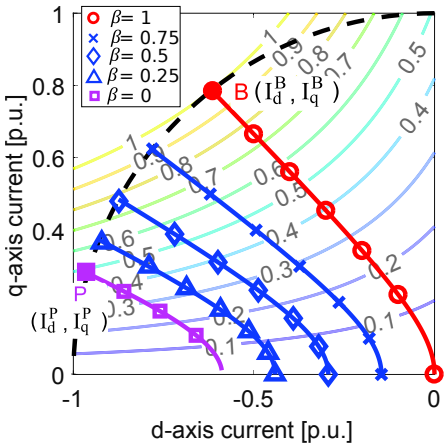

Figure 3.4: Action of the parameter β.

3.2.2. Speed control

The speed controller provides the quadrature current reference i_q^* which must be limited to a proper value $\pm i_q^{\mathrm{lim}}$. The limitation is necessary (i) to comply with the maximum current bound and (ii) to track the MTPV trajectory. These two tasks are accomplished by mean of the voltage loop parameters β and α respectively.

The maximum admissible i_q^* to observe the current limit circle is obtained as the intersection between the set of curves expressed as a function of β in (3.2) and the circle itself, as shown in (3.3). In this way it is possible to express the limit as a function $g(\beta)$. For the sake of clarity, expression (3.2) can be rewritten in the form $i_q^2 = h(i_d, \beta)$ as shown in the first equation of (3.3). The coefficients ξ_1, ξ_2 and ξ_3 depend on β and are reported in (3.4). The curve is plotted (blue solid line with markers) in Figure 3.5 for $\beta = 0.5$.

$$\begin{cases} i_q^2 = \xi_1 i_d^2 + \xi_2 i_d + \xi_3 \\ i_d^2 + i_q^2 = I_N^2 \end{cases} \tag{3.3}$$

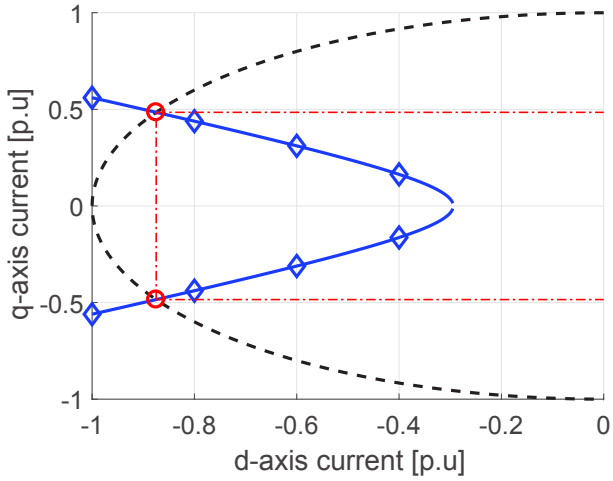

Figure 3.5: Graphical solution of (3.3) for the maximum i_q^* calculation

$$\begin{aligned}
\xi_1 &= \left[\frac{L_d}{\beta L_d + (1-\beta)L_q}\right]^2 \\
\xi_2 &= \left[2\frac{(1-\beta)}{L_d}\xi_1 + \frac{1}{L_d - L_q}\sqrt{\xi_1}\right]\Lambda_{mg} \\
\xi_3 &= \frac{(1-\beta)}{L_d}\left[\frac{(1-\beta)}{L_d}\xi_1 + \frac{1}{L_d - L_q}\sqrt{\xi_1}\right]\Lambda_{mg}^2
\end{aligned} \tag{3.4}$$

Combining the two curves in (3.3), it is possible to obtain the second order equation (3.5), which solution is $i_{d,\mathrm{sol}}(\beta)$ reported in (3.6). It is worth highlighting that only the negative value has to be saved since IPMSMs are operated in the second and third quadrants where the direct current is negative.

$$(1+\xi_1)i_d^2 + \xi_2 i_d + (\xi_3 - I_N^2) = 0 \tag{3.5}$$

$$i_{d,\mathrm{sol}}(\beta) = \frac{-\xi_2 - \sqrt{\xi_2^2 - 4(1+\xi_1)(\xi_3 - I_N^2)}}{2(1+\xi_1)} \tag{3.6}$$

The exact formulation of $g(\beta)$ can be finally expressed as in (3.7). Both positive and negative values have to be considered depending on the sign of the torque demand.

$$g(\beta) = \pm\sqrt{I_N^2 - i_{d,\mathrm{sol}}(\beta)^2} \tag{3.7}$$

With reference to Figure 3.4 ,when $\beta = 1$ the limit is equal to the quadrature current at the base point I_q^B (point B). When $\beta = 0$ the limit is the quadrature current at the beginning of the MTPV I_q^P (point P). In this way, by limiting the quadrature current with $g(\beta)$ and computing the direct current as in (3.2), the current limit is inherently observed.

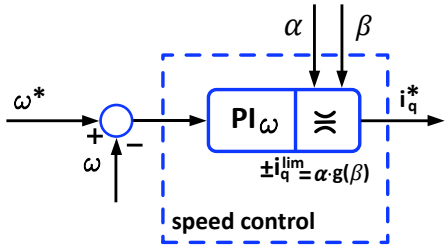

Figure 3.6: Scheme of the speed controller.

The MTPV locus is characterized by a quadrature current in the interval $[0; I_q^P]$. In order to track this trajectory, the function $g(\beta)$ is multiplied by $\alpha \in [0; 1]$. The overall limitation is expressed in (3.8) where the values of $i_q^{\lim}$ are explicitly expressed for the boundaries of the voltage loop parameter. The resulting scheme of the speed control is reported in Figure 3.6.

$$\begin{aligned} i_q^{\lim} &= \alpha \cdot g(\beta) \\ i_q^{\lim} &= \begin{cases} I_q^B & \text{if } \alpha = 1, \quad \beta = 1 \\ I_q^P & \text{if } \alpha = 1, \quad \beta = 0 \\ 0 & \text{if } \alpha = 0, \quad \beta = 0 \end{cases} \end{aligned} \tag{3.8}$$

3.2.3. Voltage loop

The voltage control loop is employed for the generation of proper current references that allow the transition between the different operating conditions. As already mentioned, its action is performed by mean of two different parameters α, $\beta \in [0; 1]$.

The scheme of the voltage loop is reported in Figure 3.7. From the output of the two current regulators, i.e. the voltage references u_d and u_q, the voltage vector amplitude $|u|$ is calculated and compared to the limit value $U_{\lim}$. The error $U_{\lim} - |u|$ is then processed by an integral controller with gain k_I that generates the parameter z which is limited between ± 1. The latter is used for the calculation of the two coefficients α and β defined as in (3.9).

$$\begin{aligned} \beta &= \begin{cases} z, & \text{if } z \geq 0 \\ 0, & \text{if } z < 0 \end{cases} \\ \alpha &= \begin{cases} 1, & \text{if } z \geq 0 \\ 1 + z, & \text{if } z < 0 \end{cases} \end{aligned} \tag{3.9}$$

The first parameter β is used for the computation of the direct current reference and, together with the second coefficient α, for the limitation of the speed controller output, as explained in subsection 3.2.1 and subsection 3.2.2 respectively. Figure 3.8 summarises the behaviour of the parameters z, α and β for the different working points in the direct and quadrature current plane.

Until the stator voltage is lower than $U_{\lim}$, the voltage loop integrator is saturated to its maximum $z = 1$. In this situation $\alpha = \beta = 1$ and the drive is controlled to work along the MTPA locus. The value of the quadrature current i_q^* depends on the torque

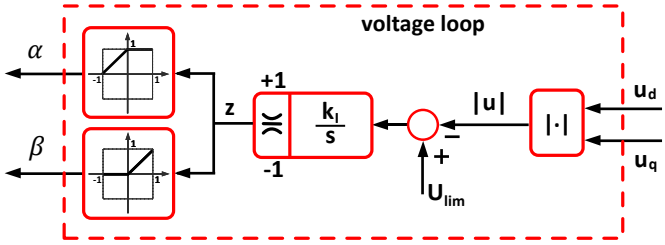

Figure 3.7: Scheme of the voltage loop.

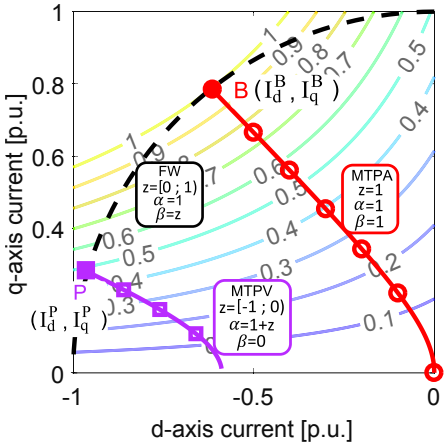

Figure 3.8: Operation of the voltage loop.

required to follow the input speed reference and it is limited in the interval $[0; I_q^B]$. The reference of the d axis current is $i_d^*(i_q^*) = i_d^{\text{MTPA}}$ and it is in the interval $[0; I_d^B]$.

When the stator voltage goes beyond the limit (for instance when the speed exceeds the base value at the rated torque), the negative voltage error decreases the integrator output z. Therefore with z ranging from 1 down to 0, the parameter α is kept equal to 1 while $\beta = z$. As a consequence the drive is commanded to work in a point of the FW region delimited by MTPA and MTPV lines, the latter being reached at $z = 0$, and the current limit circumference according to the demanded torque. It is worth to notice that the operating point is the one exhibiting the smallest current amplitude and joule losses and then the maximum efficiency.

When z ranges from 0 down to -1, since β is fixed to 0 the d axis reference is $i_d^*(i_q^*) = i_d^{\text{MTPV}}$. Besides the quadrature current is limited with α varying in $[0; 1]$ and $g(\beta) = I_q^P$, i.e. $i_q^* \in [0 : I_q^P]$. In other words, the drive works on the MTPV curve with a maximum current amplitude limited by z through the parameter α in order to comply with the voltage limitation.

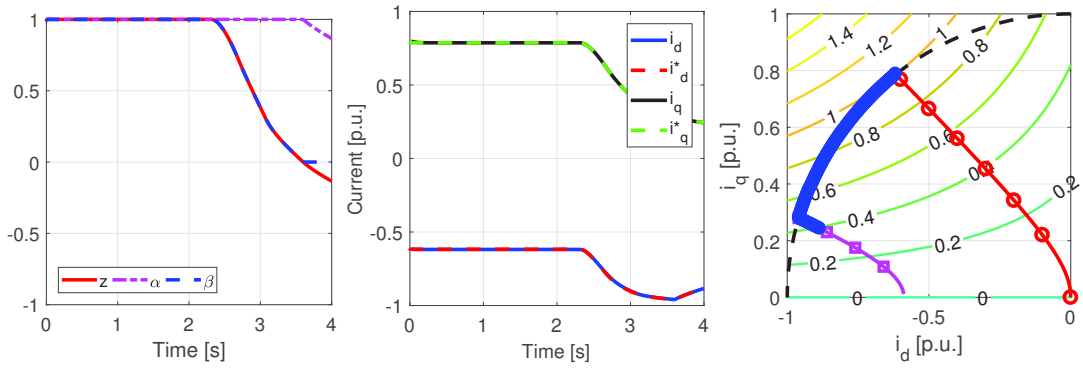

(a) Control parameters (b) d and q currents (c) Working points in i_d-i_q plane

Figure 3.9: Test with the motor dragged with a speed ramp (simulation).

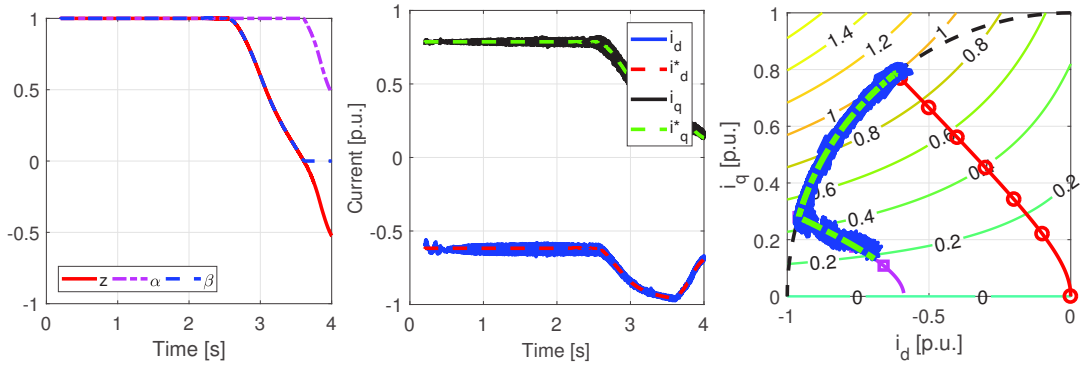

(a) Control parameters (b) d and q currents (c) Working points in i_d-i_q plane

Figure 3.10: Test with the motor dragged with a speed ramp (experimental).

3.3. Model validation

The proposed scheme has been tested by mean of numerical simulations and experiments as well. The results are reported in this section.

The magnetic characteristics of the machine have been experimentally evaluated and used in the numerical model to include the effects of iron saturation. On the contrary, the current references in both the simulations and the experiments are obtained considering the ideal behaviour of the machine, i.e. iron saturation is neglected in the control algorithm. For the sake of simplicity, the constant torque hyperbole, the MTPA and the MTPV loci in the following results are referred to the ideal machine case.

The IPMSM under test is a 8-poles machine. The value of phase resistance is $R = 1.5\ \Omega$ and the apparent unsaturated inductances are equal to $L_d = 34\ mH$ and $L_q = 86\ mH$.

During the first test the machine is dragged by the master motor with a speed ramp that starts from zero and goes beyond the base value, while the speed controller is artificially saturated so that the maximum torque is required. The results of the simulation and of the experimental test are reported in Figure 3.9 and Figure 3.10 respectively. As

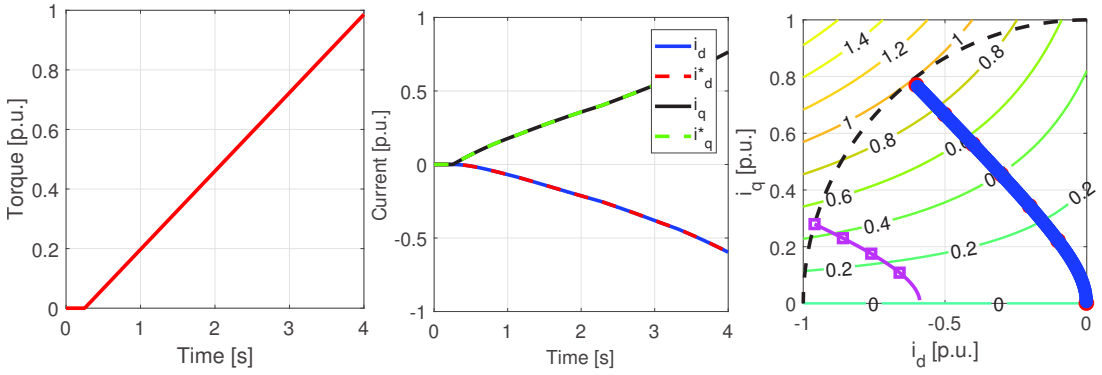

(a) Control parameters (b) d and q currents (c) Working points in i_d-i_q plane

Figure 3.11: Test with a braking torque ramp (simulation).

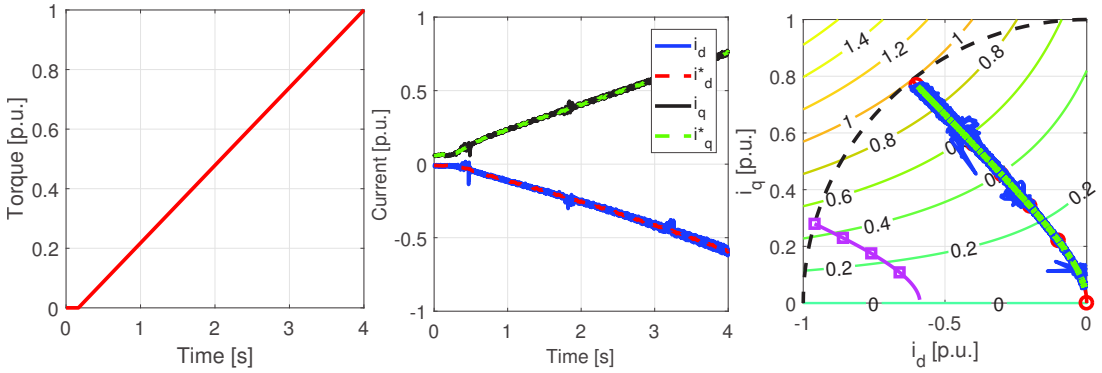

(a) Control parameters (b) d and q currents (c) Working points in i_d-i_q plane

Figure 3.12: Test with a braking torque ramp (experimental).

long as the speed is lower than the base value, the working point coincides with the base point and all the voltage loop parameters are unitary. When the base speed is exceeded, the voltage loop decreases the value of z and the parameters α, β. In this way, the point of work is shifted achieving the FW and the MTPV operation while observing the maximum current limit. It is worth noticing that there are admissible differences between the simulation and the experimental results due to slight inaccuracies in the numerical model, e.g. cross-saturation effect and parameters variation with the temperature are not considered. Nevertheless, there is a good agreement between the numerical results and the experiments. The first test confirmed the expectations and verified the correct operation of the control algorithm in all the operating conditions. Further tests are needed to deeply investigate the performance of the proposed scheme and in particular to evaluate the interaction between the speed and the voltage loop.

A second test, reported in Figure 3.11 and Figure 3.12, has been carried out giving a constant speed reference below the base value and providing an increasing braking torque with the master motor. Since the voltage loop parameters are unitary, the d and q axes currents closely track the ideal MTPA trajectory. The measured currents of Figure 3.12b present a visible periodic disturbance that is given by the non ideal synchronization of the switching frequency in the two inverters, namely the one of the

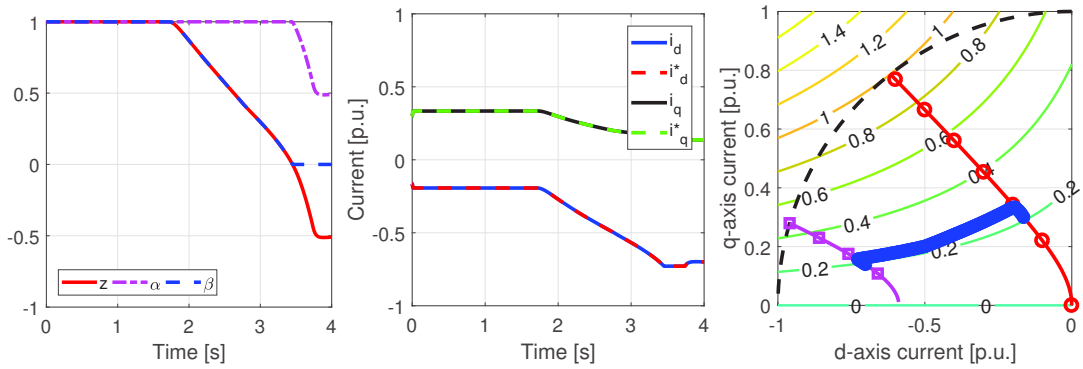

(a) Control parameters (b) d and q currents (c) Working points in i_d-i_q plane

Figure 3.13: Test with a speed ramp (simulation).

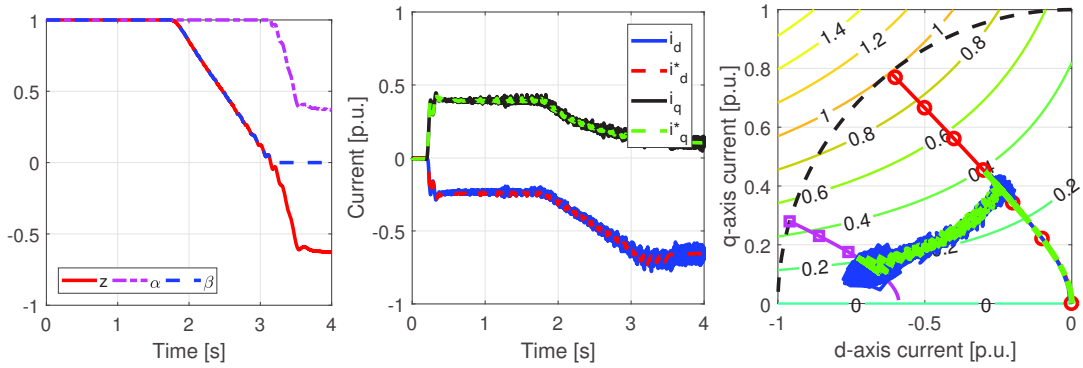

(a) Control parameters (b) d and q currents (c) Working points in i_d-i_q plane

Figure 3.14: Test with a speed ramp (experimental).

master machine and the one of the IPMSM under test.

The goal of the last test reported in this abstract is to evaluate the algorithm during a transition from the MTPA to the MTPV. In particular a speed ramp is provided while the master machine produces a constant braking torque. The results are reported in Figure 3.13 and Figure 3.14. As can be seen in both simulation and experimental test, the point of work does not track the ideal constant torque hyperbole plotted in the background but its position depends on the true characteristics of the machine. It is worth highlighting the effectiveness of the algorithm in this test and in particular the smooth transition between the different operating conditions.

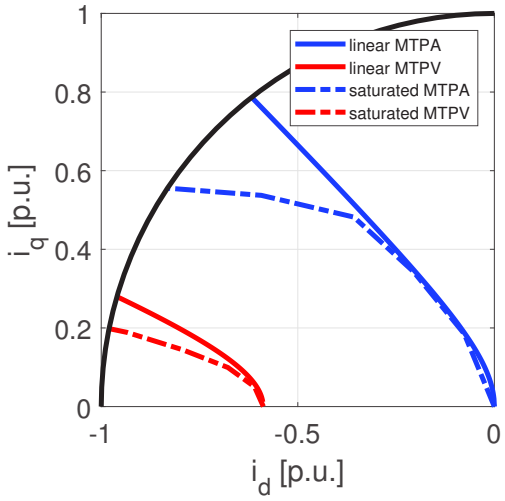

Figure 3.15: MTPA and MTPV loci for a linear and saturated machine.

3.4. Extension to saturated machine

The proposed scheme has been presented and tested considering an ideal linear machine allowing clarity and ease of explanation. However, a suitable control algorithm should be able to cope with the real magnetic characteristics of the machine. For this reason, in this section, a detailed description of how it is possible to include this aspect in the algorithm is presented.

In case of saturation the MTPA and MTPV loci are deformed and deviate from the ones obtained considering a linear machine model. This can be noticed in Figure 3.15, where the linear trajectories are plotted with solid line and the actual with dashed line. The latter have been obtained by measurements.

The knowledge of the actual magnetic characteristics is required for (i) the current reference generation, since equations (3.1) are not valid under the effect of iron saturation, and for (ii) the exact quadrature current limitation. Both these aspects are crucial for the effective operation of the drive and a non precise observation of them could strongly affect its performance. Surely, if (i) is not properly designed, the machine will not work at the point of maximum efficiency. Besides, (ii) guarantees the safe working of the machine in compliance with the maximum current limit and it avoids harmful operations or permanent damages.

Subsection 3.4.1 deals with the proper inclusion of the effect of iron saturation in the current reference generation while subsection 3.4.2 describes how to limit the quadrature current at the speed regulator output.

3.4.1. Current reference generation

The MTPA and MTPV trajectories can be calculated using the flux and current characteristics that can be derived by measurements or determined by means of finite element analysis. The results are then used to build two Look-Up Tables (LUT), namely $\mathrm{LUT}_{\mathrm{MTPA}}$ and $\mathrm{LUT}_{\mathrm{MTPV}}$ in (3.10).

$$\begin{aligned} i_d^{\mathrm{MTPA}}(i_q) &= \mathrm{LUT}_{\mathrm{MTPA}}(i_q) \\ i_d^{\mathrm{MTPV}}(i_q) &= \mathrm{LUT}_{\mathrm{MTPV}}(i_q) \end{aligned} \tag{3.10}$$

The two look up tables are used to replace (3.1), i.e. to compute the direct current reference i_d^* knowing the quadrature current reference i_q^* and the voltage loop parameter β. In other words, they are utilized for the implementation of equation (3.2).

3.4.2. Quadrature current limitation

As the MTPA and MTPV loci vary, the quadrature current limitation at the speed controller output has to change accordingly to comply with the maximum current constraint. For this purpose another look up table, stated with $\mathrm{LUT}_{q-\max}$ in (3.11), is used to substitute the function $g(\beta)$. This look up table implements the relationship between the control parameter β and the maximum admissible i_q^* to observe the current limit circle.

$$i_q^*(\beta) = \mathrm{LUT}_{q-\lim}(\beta) \tag{3.11}$$

The maximum acceptable current i_q^* can be calculated as the intersection between the set of curves expressed as a function of β in (3.2) and the current limit circumference, similarly to the linear case, discussed in subsection 3.2.2. Combining the two curves the second order equation (3.12), whose coefficients are reported in (3.13), is obtained.

$$\sigma_1\beta^2 + \sigma_2\beta + \sigma_3 = 0 \tag{3.12}$$

$$\begin{aligned} \sigma_1 &= (i_d^{\mathrm{MTPA}} - i_d^{\mathrm{MTPV}})^2 \\ \sigma_2 &= 2i_d^{\mathrm{MTPV}}(i_d^{\mathrm{MTPA}} - i_d^{\mathrm{MTPV}}) \\ \sigma_3 &= [i_q^2 + (i_d^{\mathrm{MTPV}})^2 - I_N^2] \end{aligned} \tag{3.13}$$

It is worth to notice that in the case of saturation i_d^{MTPA} and i_d^{MTPV} in (3.13) are calculated by means of the look up tables $\mathrm{LUT}_{\mathrm{MTPA}}$ and $\mathrm{LUT}_{\mathrm{MTPV}}$. So with the equation (3.12), given a value of the quadrature current the corresponding value of β can be determined. It is important to clarify that (3.12) provides two values of the parameter β but only one of them is positive and in the range $[0; 1]$ and thus has to be considered. In this way a look up table that provides β given the maximum admissible i_q^* to observe the current limit has been built and it can be easily inverted in order to obtain the required $\mathrm{LUT}_{q-\max}$.

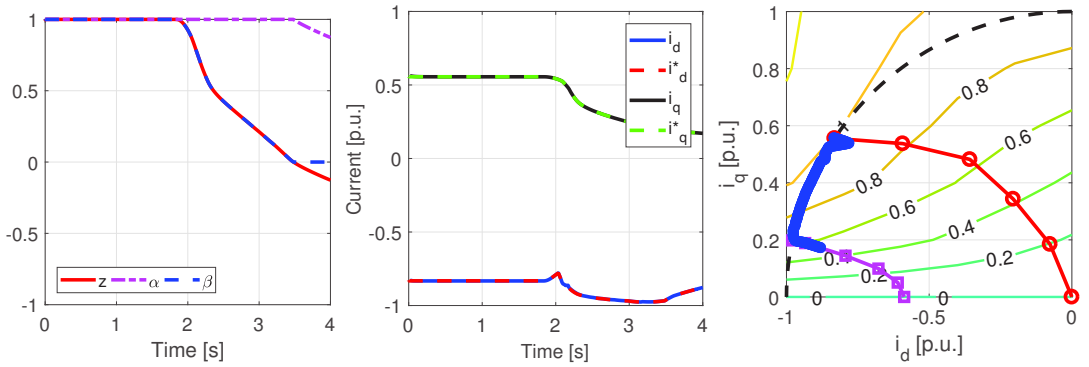

(a) Control parameters (b) d and q currents (c) Working points in i_d-i_q plane

Figure 3.16: Test with the motor dragged with a speed ramp with actual MTPA and MTPV trajectories (simulation).

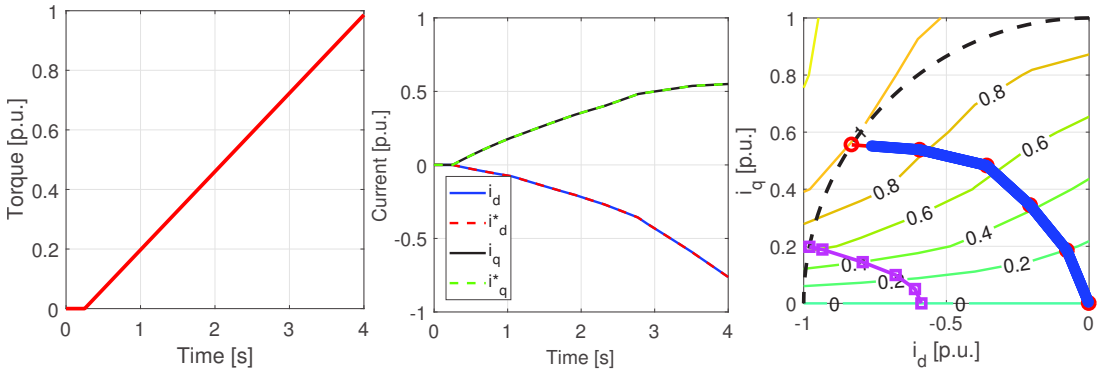

(a) Control parameters (b) d and q currents (c) Working points in i_d-i_q plane

Figure 3.17: Test with a braking torque ramp with actual MTPA and MTPV trajectories (simulation).

3.4.3. Test with saturated machine

Some simulation tests have been carried out to verify the effectiveness of the control algorithm when the saturation of the machine is taken into account. The same test of Figure 3.9 has been repeated, i.e. the machine is dragged by the master motor with a speed ramp. Furthermore the speed controller is artificially saturated so that the maximum torque is required. This represents the most significant test to verify the correct current tracking and limitation. In Figure 3.16 the simulation results are reported. Figure 3.16b shows the current waveforms and the voltage loop parameters, while Figure 3.16c reports the actual constant torque loci, the MTPA and the MTPV trajectories and the point of work in the dq current plane. It can be noticed that at the beginning of the simulation the machine works at the actual base point, i.e. at the intersection of the current limit and the saturated MTPA trajectory. Then the quadrature current limitation performed by means of $\mathrm{LUT}_{q-\mathrm{lim}}$ allows to comply with the current limit circumference that is closely followed by the working point. Finally the working point tracks the actual MTPV trajectory.

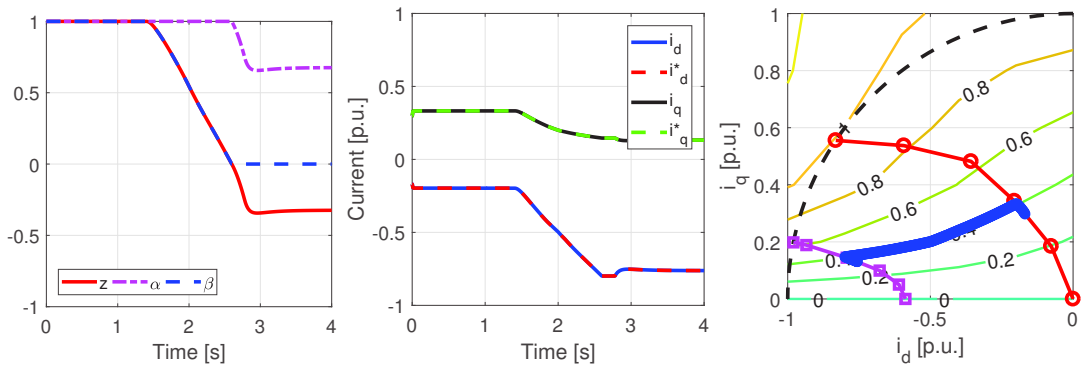

(a) Control parameters (b) d and q currents (c) Working points in i_d-i_q plane

Figure 3.18: Test with a speed ramp with actual MTPA and MTPV trajectories (simulation).

Also the tests shown in Figure 3.11 and Figure 3.13 have been repeated including the actual MTPA and MTPV trajectories of the machine. The results are reported in Figure 3.17 and Figure 3.18. The behaviour of the control algorithm does not change whether the ideal or the actual MTPA and MTPV curves are used, however in the second case the Joule losses are reduced and a higher efficiency is achieved. It is worth noticing that, differently from Figure 3.13(c), in Figure 3.18(c) the working point closely tracks the constant torque hyperbola since the actual constant torque loci are plotted.

3.5. Conclusions

This chapter presented a control scheme for the wide speed operation of IPMSM drives. The development of the control algorithm started from the solution for SyRM described in chapter 2 therefore also this control strategy is based on a voltage loop coupled with CVC in the *d*-*q* reference frame. This control algorithm has been implemented on a test bench and a reliable numerical model has been developed. Moreover a method to include the iron saturation in the control scheme by mean of look-up tables has been suggested. In particular, the actual magnetic characteristics have been considered in both the current reference generation and in the quadrature current limitation. The latter guarantees the maximum efficiency and safe operation of the machine. Both simulations and experimental tests confirmed the effectiveness of the control scheme and its ability to drive the machine in MTPA, FW and MTPV allowing the exploitation of the whole speed range.

Chapter 4

HF voltage injection position estimation and polarity detection

The rotor position estimation of anisotropic machines, such as interior permanent magnet or reluctance machines, is often obtained through the injection of high frequency voltage signals in the stator windings. This estimation algorithm is not able to determine the polarity of the magnet, leading to control issues in permanent magnet motor drives. This chapter provides an introduction to high frequency voltage injection estimation and describes a magnet polarity detection procedure relying on the mutual inductance behaviour.

4.1. Introduction

Synchronous machines require the knowledge of the rotor position for an efficient control in all the operating points. Therefore position sensors such as resolvers or absolute encoders should be installed leading to significant disadvantages in terms of cost and reliability of the drive. Sensorless drives use estimated rotor position in place of the measured one and thus allow to avoid all the cited disadvantages caused by the shaft sensors.

The existing sensorless control techniques can be classified in two main groups. The first group concerns the estimation of the rotor electrical position at medium and high speed; it is based on the reconstruction of the permanent magnet flux or back electromotive force (or, more in general, the reconstruction of the extended active flux or bemf) from the stator voltages and current measurements [23–27]. Both open loop and closed loop [28–32] schemes are implemented, the latter exhibiting higher performance at the cost of more complicated design, implementation and commissioning. However all of them do not work at zero or low speed where any electromotive force tends to disappear, voltage blends in with the resistive voltage drop and signal to noise ratio in the voltage measurement worst dramatically.

The motor starting of this first category of sensorless drives is performed in an open loop way, applying a stator voltage with an increasing ramp of frequency and amplitude,

provided that the mechanical load reaction is not too much severe. In order to enhance the drive performance, these sensorless techniques are often combined with an initial rotor position estimation technique with the aim of improving the starting capability and/or fastening the closed loop estimator convergence. Some examples can be found in [33–36] where a series of rectangular voltage pulses are injected in the motor phases and the peak of the current response is evaluated to recognise the inductance variation and thus the rotor position. Since the inductance varies according to the rotor position, these techniques allow to locate the magnetic axis of the motor. This additional control algorithm however increases drive control complexity and implementation cost.

The second group of sensorless control techniques produces an estimation not only at standstill but also in the low working speed range up to a speed that allows an estimator of the first group to operate. The estimation is based on the injection of additional high frequency voltages in the stator winding and it exploits the presence of a high frequency rotor anisotropy; so it is particularly suitable for interior permanent magnet synchronous machines [37, 38] or ringed pole machines [39]. There are several techniques that differ from the typology of the signals that are employed for the anisotropy recognition: high frequency sinusoidal [37, 40–42] or square-wave [43] carriers are often adopted since the current that is generated by them is dependent on the rotor electrical position.

All these techniques suffer from an ambiguity in the electrical position estimation of π rad, that is in the d axis polarity. This possible error can cause starting failure or temporary inverse rotation, so a d axis polarity detection is necessary for a smooth and effective starting of the motor. The above mentioned initial rotor position estimation methods could be employed to solve the polarity ambiguity; however their capability could be excessive, as only the d axis direction has to be found. Therefore several dedicated methods to distinguish the magnet polarity have been developed. Also in this case there exists a distinction between different techniques proposed in literature. A possible strategy consists in feeding the motor with alternating direct voltage or direct reference current and recognise the different magnetisation of the rotor from the resulting current feedback or voltage reference respectively [43–46]. The high frequency d current amplitude variation also indicates the magnet polarity [47]. Finally the current second harmonic for both rotating and pulsating voltage carrier injection can be analysed to determine the d axis polarity [40–42].

The cross-saturation effect interferes with the rotor position estimation by using high frequency injection technique, so several studies were done to understand how it affects the estimation precision. To further analyse the question the properties of the cross-saturation inductance were also investigated [48–52].

In this chapter an overview of the High Frequency (HF) voltage injection position estimation is reported. Moreover the possibility to exploit the knowledge of the cross-saturation inductance properties for magnet polarity detection is investigated leading to the design of a new estimation procedure. The proposed polarity detection method is more suitable for applications in which the rotor may be locked. Its main advantage is that it employs the same scheme of high frequency voltage injection used for position estimation without the need of extra filtering stages and demodulation.

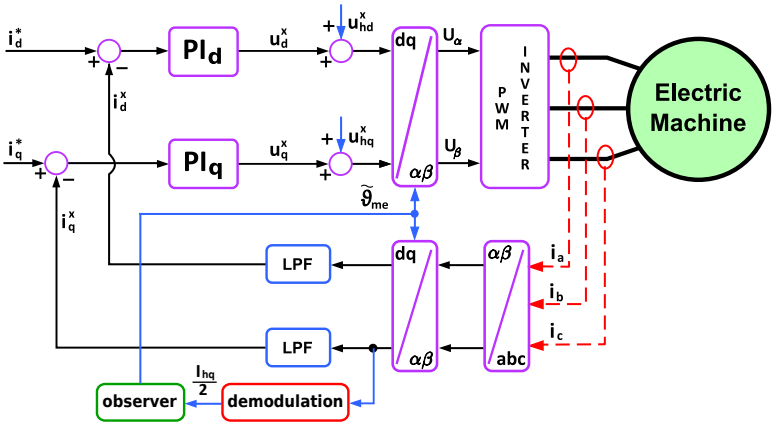

Figure 4.1: Block scheme of the sensorless drive with HF injection.

4.2. Overview of HF Voltage injection based estimation

This section explains the basis of the high frequency voltage injection for the position estimation at low speed or at standstill.

4.2.1. Estimation scheme

An estimation of the rotor speed and position at low speed or at standstill can be obtained through the injection in the stator windings of additional high frequency voltage signals. This estimation technique exploits the presence of a high frequency rotor anisotropy so it is particularly suitable for interior permanent magnet synchronous machines, synchronous reluctance machines or ringed pole motors.

In Figure 4.1 the scheme of the sensorless drive is represented. Low-pass filters are employed to separate the fundamental power components of the current, that are needed as feedback for the current control loops, from the high frequency ones that are caused by the voltage injection. The filtering stage is necessary otherwise the current regulators compensate for the high frequency currents compromising the estimation feasibility.

Hereafter the reference frames described in Figure 4.2 are considered. In addition to the stator α-β and rotor d-q reference frames, a third axes system d^x-q^x is considered. It indicates the estimated rotor reference frame which is obtained from α-β through a rotation of the estimated rotor position $\tilde{\vartheta}_{me}$. The d^x-q^x reference differs from the actual rotor one d-q by the angle $\Delta\vartheta = \tilde{\vartheta}_{me} - \vartheta_{me}$ which is the estimation error.

The voltage signals in (4.1) are employed to sense the machine rotor position. The superscript x indicates that the signal are expressed in the estimated reference frame while the subscript h is used for the high frequency signals.

$$\begin{aligned} u^x_{hd} &= U_h cos(\omega_h t) \\ u^x_{hq} &= 0 \end{aligned} \tag{4.1}$$

A model of the machine at high frequency (4.2) is necessary to calculate the expres-

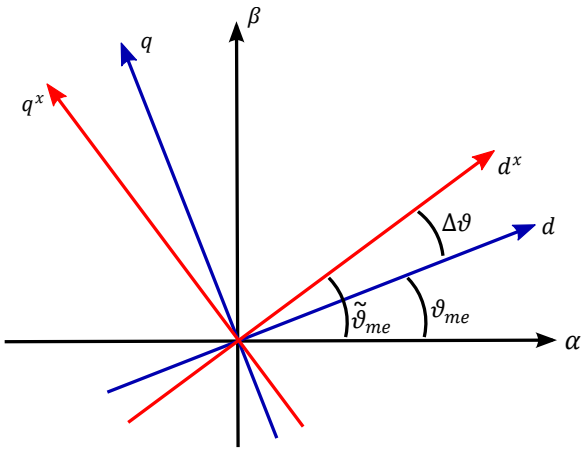

Figure 4.2: Actual and estimated rotor reference frame.

sion of the currents i^x_{hd} and i^x_{hq} induced in the stator windings.

$$\begin{aligned} u_{hd} &= \ell_d(i_d, i_q)\frac{\mathrm{d}i_{hd}}{\mathrm{d}t} + \ell_{dq}(i_d, i_q)\frac{\mathrm{d}i_{hq}}{\mathrm{d}t} \\ u_{hq} &= \ell_{dq}(i_d, i_q)\frac{\mathrm{d}i_{hd}}{\mathrm{d}t} + \ell_q(i_d, i_q)\frac{\mathrm{d}i_{hq}}{\mathrm{d}t} \end{aligned} \tag{4.2}$$

The differential inductances defined in (4.3) are considered since the high frequency response is analysed.

$$\ell_d(i_d, i_q) = \frac{\partial \lambda_d(i_d, i_q)}{\partial i_d} \qquad \text{and} \qquad \ell_q(i_d, i_q) = \frac{\partial \lambda_q(i_d, i_q)}{\partial i_q} \tag{4.3}$$

In order to have an accurate model of the machine the iron saturation phenomenon should be taken into account. It leads to a non-linear relationship between current and fluxes and consequently to inductances that change with the machine current. Besides the current of one axis can saturate the magnetic circuit of both axes leading to a reduction of the inductances and to a magnetic linkage between the direct and quadrature axes. Therefore to accurately represent the iron saturation the d and q differential inductances has to be considered as function of the working point on the rotor reference frame $\ell_d(i_d, i_q)$ and $\ell_q(i_d, i_q)$ and the cross-saturation differential inductances $\ell_{dq}(i_d, i_q)$ and $\ell_{qd}(i_d, i_q)$, defined in (4.4), have to be introduced.

$$\ell_{dq}(i_d, i_q) = \frac{\partial \lambda_d(i_d, i_q)}{\partial i_q} = \frac{\partial \lambda_q(i_d, i_q)}{\partial i_d} = \ell_{qd}(i_d, i_q) \tag{4.4}$$

The speed dependent terms in the model can be neglected considering the machine at standstill or working at a very low speed. Moreover if high frequency signals are fed to the motor winding the resistive voltage drop is much smaller with respect to the inductive terms and thus can be neglected.

The resulting high frequency currents are sinusoidal signals, as expressed in (4.5), whose amplitudes I_{hd} and I_{hq} are defined in (4.6) where $\ell_\Delta(i_d, i_q) = \frac{[\ell_q(i_d,i_q) - \ell_d(i_d,i_q)]}{2}$ and $\ell_\Sigma = \frac{[\ell_q(i_d,i_q) + \ell_d(i_d,i_q)]}{2}$.

$$\begin{aligned} i^x_{hd} &= I_{hd}\sin(\omega_h t) \\ i^x_{hq} &= I_{hq}\sin(\omega_h t) \end{aligned} \tag{4.5}$$

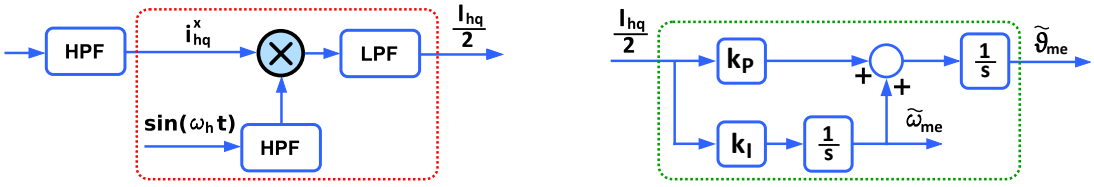

(a) Demodulation (b) Two-state observer

Figure 4.3: Estimation schemes.

$$
\begin{aligned}
I_{hd} &= \frac{U_h[-\ell_\Sigma(i_d,i_q) - \ell_\Delta(i_d,i_q)\cos(2\Delta\vartheta) + \ell_{dq}(i_d,i_q)\sin(2\Delta\vartheta)]}{\omega_h(\ell^2_{dq}(i_d,i_q) - \ell_d(i_d,i_q)\ell_q(i_d,i_q))} \\
I_{hq} &= \frac{U_h[\ell_\Delta(i_d,i_q)\sin(2\Delta\vartheta) + \ell_{dq}(i_d,i_q)\cos(2\Delta\vartheta)]}{\omega_h(\ell^2_{dq}(i_d,i_q) - \ell_d(i_d,i_q)\ell_q(i_d,i_q))}
\end{aligned}
\tag{4.6}
$$

For the sake of simplicity a linear machine is considered at first. An ideal model of the motor allows to explain and understand the basic operation principle of the high frequency position estimation. Later in this chapter and in chapter 5 the effects of the iron saturation will be deeply discussed. For a linear machine the current amplitudes can be simplified as in (4.7). Under the assumption of no iron saturation the inductances are constant and independent on the working point and the cross-coupling term ℓ_{dq} is null.

$$
\begin{aligned}
I_{hd} &= \frac{U_h}{\omega_h \ell_d \ell_q}[\ell_\Sigma + \ell_\Delta \cos(2\Delta\vartheta)] \\
I_{hq} &= -\frac{U_h}{\omega_h \ell_d \ell_q}[\ell_\Delta \sin(2\Delta\vartheta)]
\end{aligned}
\tag{4.7}
$$

It can be noticed that the amplitudes of the current responses are dependent on the estimation error $\Delta\vartheta$ and thus contain information about the rotor position. In particular if the estimation is correct $\Delta\vartheta = 0$ no high frequency current is present in the estimated quadrature axis, i.e. $I_{hq} = 0$. Therefore the estimation can be obtained by nullifying I_{hq} trough a two-state (Figure 4.3(b)) or three-state observer. In order to get the value of I_{hq} the quadrature current i_q is processed using the demodulation scheme in Figure 4.3(a). Firstly a high-pass filter is used to eliminate the fundamental current components and extract i^x_{hq}. Then i^x_{hq} is multiplied by a sinusoidal wave that was previously filtered using the same high-pass filter. This is done in order to obtain the same delay for the two signals. The result of this operation is reported in (4.8).

$$
i^x_{hq}\sin(\omega_h t) = I_{hq}\sin^2(\omega_h t) = \frac{I_{hq}}{2}[1 - \cos(2\omega_h t)] \tag{4.8}
$$

Afterwards, a low pass filter is applied to eliminate the component at $2\omega_h$ frequency and finally get $I_{hq}/2$.

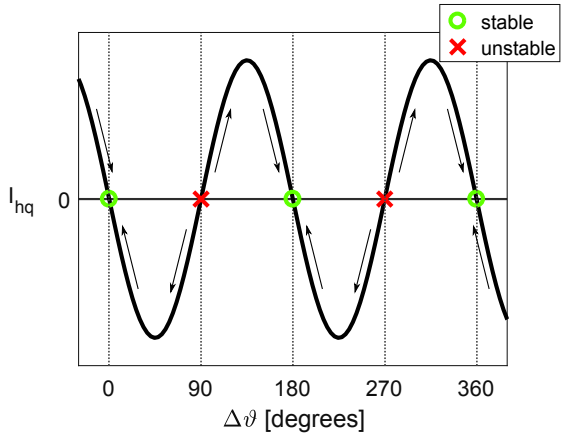

Figure 4.4: Stable and unstable convergence of the estimator.

4.2.2. Magnet polarity detection issue

Since the current I_{hq} that the observer is trying to nullify is dependent on $\sin(2\Delta\vartheta)$ there exist different positions to which the estimation could converge. In particular all the values of $\Delta\vartheta$ that correspond the zeros of the sine function, i.e. $\Delta\vartheta = k\pi/2$ for $k = 0, 1, ...$, are possible convergence points for the observer. However only the ones characterised by a negative derivative, obtained with $k = 0, 2, ...$, are stable convergence solution of the estimation algorithm as shown in (Figure 4.4). So there exist two stable positions to which the estimation could converge: the correct one, $\Delta\vartheta = 0$, and $\Delta\vartheta = \pi$. This ambiguity is not an issue in the case of a synchronous reluctance machine since it features a symmetrical rotor. On the contrary for an IPMSM or a permanent magnet assisted reluctance motor the presence of two possible solutions means that the estimation technique is not capable to determine the magnet polarity, as it can be seen in Figure 4.5. For these machine typologies an incorrect identification of the d axis orientation may cause unacceptable troubles during the motor starting. Therefore a technique to recognise the polarity is necessary and for this purpose the magnetic saturation effect is exploited. In particular the technique proposed in this chapter relies upon the cross-saturation effect.

4.2.3. Estimation error

Iron saturation has been neglected so far in order to describe the desired ideal operation of the position estimation. However the saturation effect is always present in a real machine so in order to evaluate the algorithm performance it has to be taken into account. The cross-saturation, in particular, has an unwanted effect that worsens the estimation accuracy. As it has been explained, the estimated position is achieved by nullifying I_{hq}. If the expression in (4.6), that takes into account the saturation, is considered instead of (4.7), which represents the linear case, it can be noticed that for a saturated machine I_{hq} is null for $\Delta\vartheta = \epsilon$.

$$\epsilon = \frac{1}{2}\operatorname{atan}\left(-\frac{\ell_{dq}(i_d, i_q)}{\ell_{\Delta}(i_d, i_q)} \right) \tag{4.9}$$

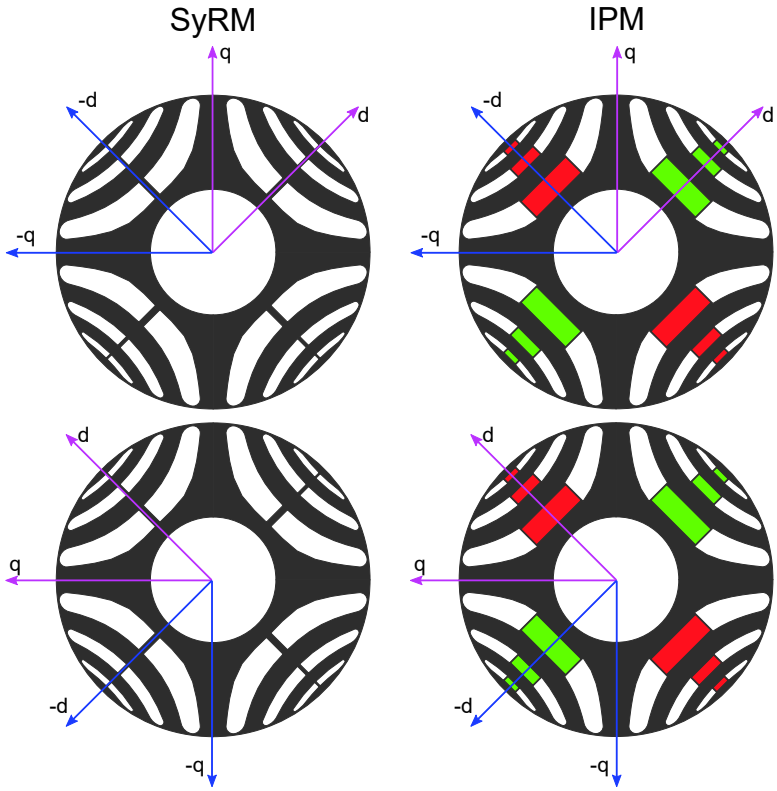

Figure 4.5: Ambiguity in the d axis direction in SyRM and IPMSM.

This means that in presence of cross-saturation the estimation algorithm does not converge to the correct position. It is worth highlighting that the estimation error depends on the working point of the machine. When the machine is not heavily saturated the estimation error is moderate and the sensorless drive can operate correctly. Differently, in presence of a strong saturation effect some compensation techniques have to be adopted in order to obtain reliable position information.

4.3. Magnet polarity detection principle

Cross-saturation effect, on one hand affects the estimation accuracy worsening the performance of the sensorless drive, but, on the other hand, it can be useful for detecting the magnet polarity. The remaining part of this chapter is dedicated to the description of a polarity detection procedure that exploits the cross-saturation.

The cross-saturation inductance ℓ_{dq} follows the trend reported in Figure 4.6 in IPM and PM assisted reluctance machine [52]. In particular ℓ_{dq} is zero along the d axis and for i_d equal to the so called characteristic current $I_{ch} = -\Lambda_{mg}/L_d$ where Λ_{mg} is the flux due to the permanent magnet and L_d is the unsaturated direct axis inductance. Moreover it can be seen that the $\ell_{dq} = 0$ locus divides the i_d-i_q plane in four regions where the sign of the cross-saturation inductance is defined according to Table 4.1.

In the case of correct position estimation the estimated direct and quadrature axes coincide with the actual ones and as a consequence the behaviour of ℓ_{dq} is the same

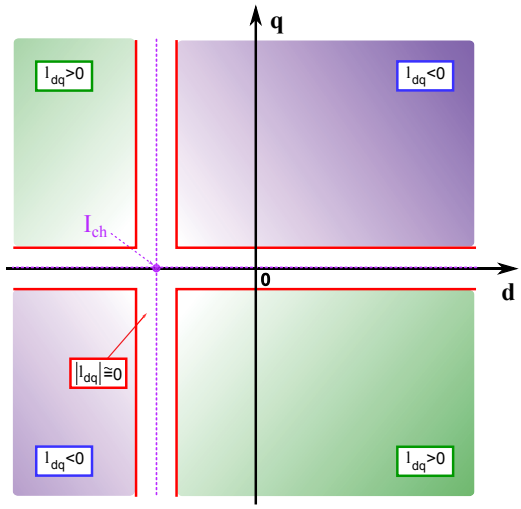

Figure 4.6: Voltage pulses for polarity detection.

Table 4.1: Cross-saturation inductance sign in the i_d-i_q plane.

	$i_d < I_{ch}$	$i_d > I_{ch}$
$i_q > 0$	$\ell_{dq} > 0$	$\ell_{dq} < 0$
$i_q < 0$	$\ell_{dq} < 0$	$\ell_{dq} > 0$

in the two reference frames, as shown in Figure 4.7(a). On the contrary, if an error of π is present in the estimated rotor electrical position the ℓ_{dq} map with respect to the estimated reference frame will appear as in Figure 4.7(b). Along the q axis ℓ_{dq} assumes both positive and negative values depending on the sign of the applied i_q^x current. Specifically, referring to the test points represented with circles in Figure 4.7, if the initial position estimation is correct a negative ℓ_{dq} corresponds to a positive i_q^x and vice versa, while when a polarity error occurs ℓ_{dq} has the opposite behaviour. The strategy for polarity detection proposed in this chapter is based on the identification of the cross-saturation inductance sign along the q^x axis.

Since during the test i_q current is applied to the motor windings, torque is produced. Different test points have been considered in order to avoid the torque generation when the polarity identification is performed. In an IPMSM the zero torque locus ($M = 0$) includes (i.) the d axis and (ii.) the line defined in (4.10).

$$i_d = \Lambda_{mg}/(L_q - L_d) \tag{4.10}$$

Along (i.) the cross-saturation inductance is equal to zero so the polarity detection test can not be performed. Differently if the test points are chosen along (ii.), as indicated by the crosses in Figure 4.7, ℓ_{dq} is different from zero. However if $L_d > \frac{L_q}{2}$ the cross-saturation inductance does not change its sign according to the correctness of the initial polarity estimation so the d axis direction can not be detected. This is the situation represented in Figure 4.7 and it can be noticed that in the two cases, $\Delta\vartheta = 0$ and $\Delta\vartheta = \pi$, the ℓ_{dq} sign in the working points indicated with the crosses is the same.

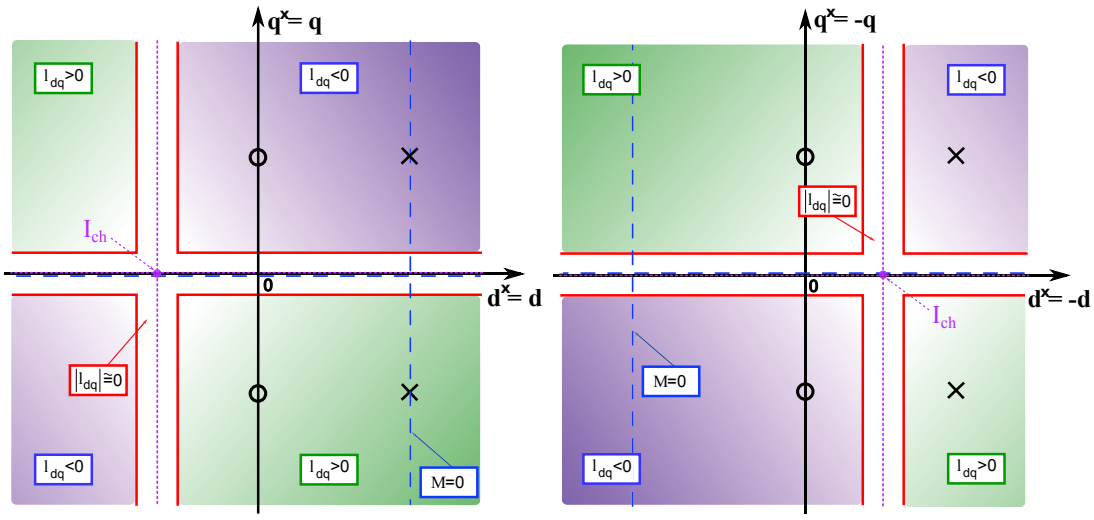

(a) Correct initial estimation (b) Incorrect initial estimation

Figure 4.7: ℓ_{dq} behaviour over the estimated current plane i_d^x-i_q^x of an IPMSM.

Furthermore in the case of a wrong estimation, the test point are not on the zero torque locus, as it can be seen from Figure 4.7(b), thus the IPMSM produces torque. So, even choosing the test points along the zero torque locus can not prevent the polarity detection test from producing torque. For these reasons the proposed technique employs test points along the q^x axis and it is apt for application in which the rotor is locked when it is at standstill such as wind generators, elevators, cranes and traction applications.

Some experimental measurements have been carried out on an IPMSM in order to investigate the applicability of the cross-saturation inductance properties for polarity detection. The machine considered in this work is a 8-pole and 9-slot machine able to deliver 8Nm of nominal torque. The value of apparent inductances, at nominal current (6 A_{rms}), are $L_d = 15mH$ and $L_q = 23mH$. The ℓ_{dq} map calculated using the measured flux-current characteristics of the machine is reported in Figure 4.8(a). It can be noticed that the behaviour of ℓ_{dq} on the current plane is similar to the theoretical one described in Figure 4.7(a).

The reciprocal inductance Γ_{dq} defined by (4.11) has been introduced and its values on the i_d-i_q plane are shown in Figure 4.8(b). The comparison of these two maps confirms that Γ_{dq} and ℓ_{dq} have the same sign on the i_d-i_q plane as the denominator of (4.11) is always positive. Therefore the polarity detection procedure can be based on the parameter Γ_{dq} instead than on ℓ_{dq}, the former being easier to be measured as will be described in section 4.4.

$$\Gamma_{dq} = \frac{\ell_{dq}}{\ell_q \ell_d - \ell_{dq}^2} \tag{4.11}$$

To sum up, the proposed technique consists in

- locking the rotor,
- activating the rotor position estimation and estimating the d axis position, apart from a possible π error,

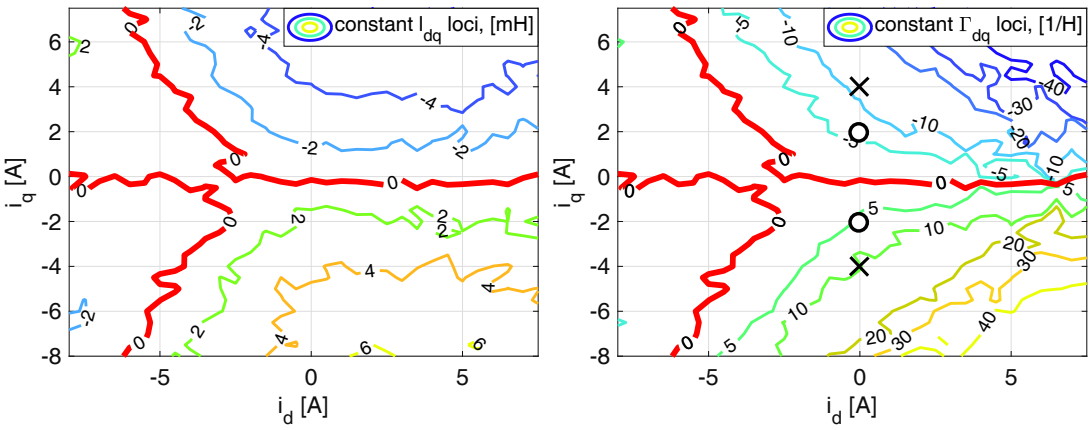

(a) ℓ_{dq} (b) Γ_{dq}

Figure 4.8: ℓ_{dq} and Γ_{dq} of an IPM-SM.

- freezing the position estimation (this condition is necessary for the correct measurement of Γ_{dq} as explained in section 4.4),
- measuring the reciprocal inductance Γ_{dq} on the estimated quadrature axis for a positive i_q^x, while the current i_d^x is controlled to zero, obtaining the value Γ_{dq}^+,
- repeating the Γ_{dq} measurement with negative current i_q^x getting the value Γ_{dq}^-.

Comparing these two measurements, the correct orientation of the direct axis can be recognised. In fact in the case of correct position estimation the quantity $\Delta\Gamma = \Gamma_{dq}^+ - \Gamma_{dq}^-$ is negative. Differently, if the position estimation is affected by an error of π, $\Delta\Gamma$ will be positive.

4.4. Parameter Γ_{dq} measurement

The parameter Γ_{dq} can be easily measured through high frequency signal injection exploiting the same scheme that is usually adopted for the position estimation. Considering the iron saturation, the high frequency current response caused by the voltage injection is the one described in (4.5) and (4.6). If $\Delta\vartheta = 0$ or $\Delta\vartheta = \pi$ the q^x high frequency current amplitude is the one described in (4.12). So from I_{hq} it is possible to determine Γ_{dq} and its sign easily.

$$I_{hq} = \frac{\ell_{dq}}{\ell_{dq}^2 - \ell_d \ell_q} \frac{U_h}{\omega_h} = -\Gamma_{dq} \frac{U_h}{\omega_h} \tag{4.12}$$

Figure 4.9 shows the block scheme of the high frequency carrier injection together with the measurement of Γ_{dq}. From this schematic representation can be noticed that the reciprocal inductance measurement is apt to be easily combined with the position estimation. Figure 4.9 also shows that the sign of I_{hq} gives the same information of that of Γ_{dq}. However in order to compare the measured quantity with that of the inductance maps the remaining part of the chapter will continue to refer to Γ_{dq}.

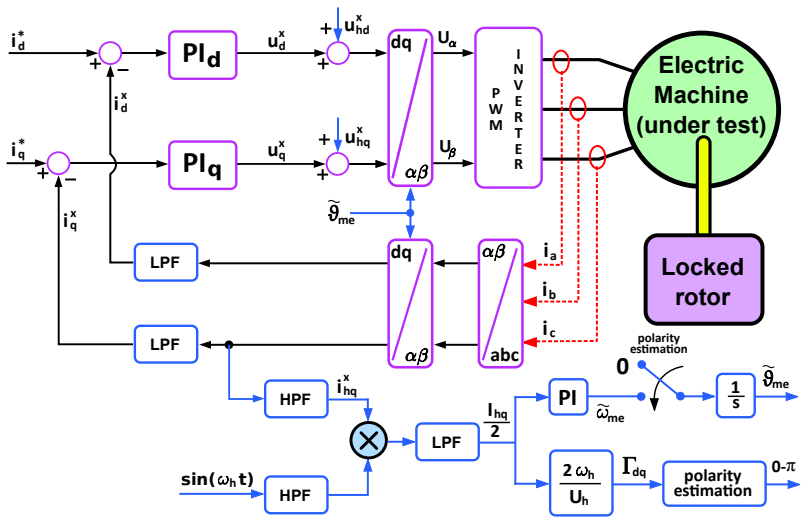

Figure 4.9: Scheme of position estimation and Γ_{dq} measurement.

The proposed scheme has been used to measure the parameter Γ_{dq} for an entire electrical period of the motor in order to investigate the rotor position effect. The results are reported in Figure 4.10(a) and Figure 4.10(b). The figures show the parameter in correspondence of both positive and negative quadrature current. A reversal in the sign of the parameter can be noticed caused by a similar change in the current applied to the stator windings, confirming what was stated in section 4.3. Furthermore the measurement is done for several current values proving the same behaviour so the polarity detection can be performed employing different testing currents. The test points used to obtain Figure 4.10(a) and Figure 4.10(b) are indicated in Figure 4.8(b) by dots and crosses respectively. It can be noticed that the values of Γ_{dq} in Figure 4.10,

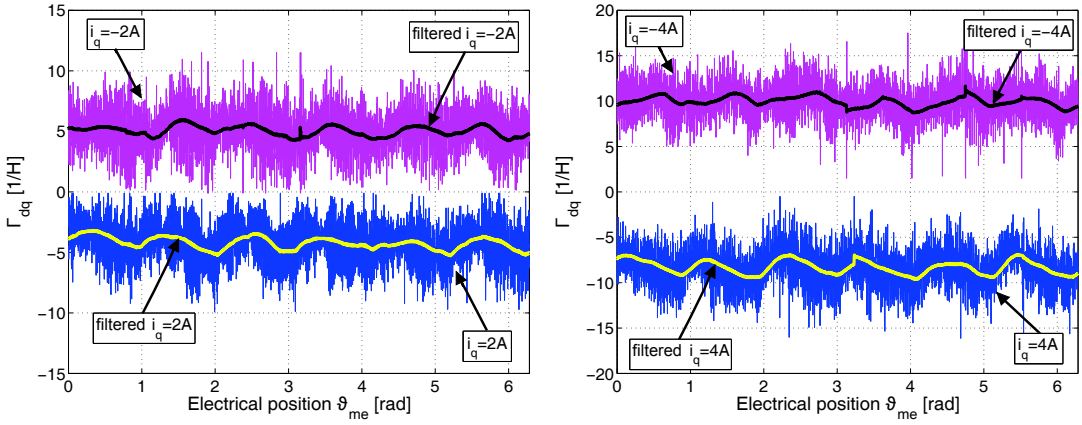

(a) $i_q^x = \pm 2A$ (b) $i_q^x = \pm 4A$

Figure 4.10: Γ_{dq} measurement in the case of correct initial estimation.

measured through the high frequency injection, correspond to the ones in Figure 4.8(a) confirming the validity of the employed measurement scheme. Finally in Figure 4.11 the same measure is performed in the case of an initial position estimation affected by

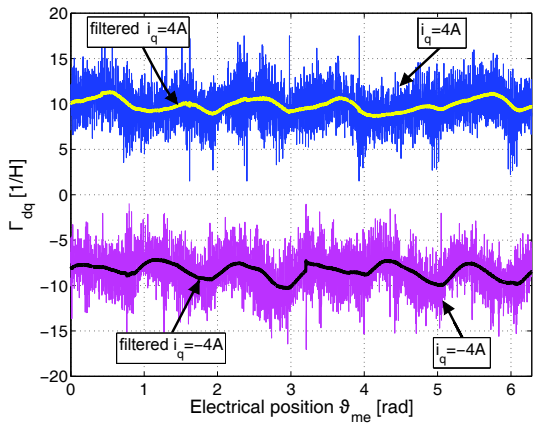

Figure 4.11: Γ_{dq} measurement in the case of incorrect initial estimation ($i_q^x = \pm 4A$).

an error of π. A comparison with Figure 4.10(b) highlights a sign reversal of Γ_{dq} based on the correctness of the initial position estimation that can be exploited, as stated in section 4.3, for magnet polarity detection. Some fluctuations due to the airgap magneto motive force harmonics can be noticed, however they do not reverse the sign of Γ_{dq} that can be easily discerned in correspondence of every ϑ_{me} proving that the proposed method for polarity detection can be applied independently of the particular position of the rotor.

In addition to its simplicity and high signal-to-noise ratio, the main advantage of the method is that it can be fully integrated with the high frequency carrier injection, as shown in Figure 4.9. However during the polarity detection test the estimated position can not be updated. In fact if the position is estimated while i_q current is applied to the motor, i.e. while ℓ_{dq} is not zero, the observer converges to $\Delta\vartheta = \epsilon \neq 0$ while Γ_{dq} must be measured only at $\Delta\vartheta = 0$ or $\Delta\vartheta = \pi$. Therefore if the rotor position is estimated during the Γ_{dq} measurement the polarity detection test could give a wrong result. Furthermore the position estimation algorithm nullifies the high frequency current I_{hq} which is at the base of the Γ_{dq} measurement as can be seen from equations (4.12). So the parameter Γ_{dq} can not be measured while the position estimation algorithm is operating. For these reasons during the polarity detection test the rotor position must be frozen.

4.5. Polarity detection procedure implementation

Some simulations and experimental tests have been carried out in order to validate the proposed procedure. The IPMSM described in section 4.3 has been considered. During the experimental test a dSPACE fast-prototyping system has been used to control a voltage-source inverter. The rotor position was measured and compared with the estimated one for validating the strategy described so far. Figure 4.12 and Figure 4.13 illustrates the procedure of polarity identification in the cases of a correct and incorrect initial rotor position estimation. Both simulation and experimental tests are reported.

In the initial part the position is estimated. During this process the low frequency components of the current are controlled to zero. In this condition the cross-saturation inductance is null, as shown in section 4.3, and the possible estimation error caused by

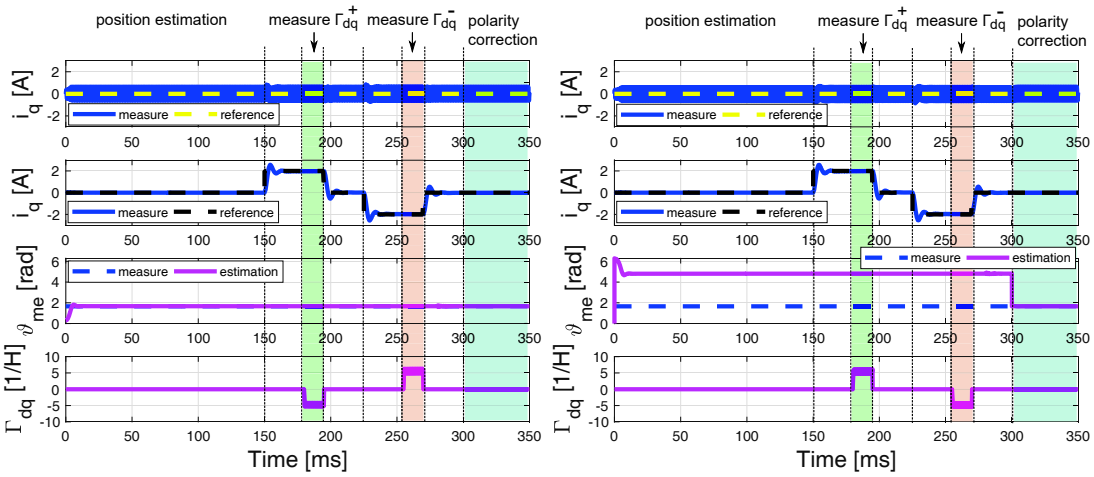

(a) Correct initial estimation (b) Incorrect initial estimation

Figure 4.12: Position and polarity estimation (simulation).

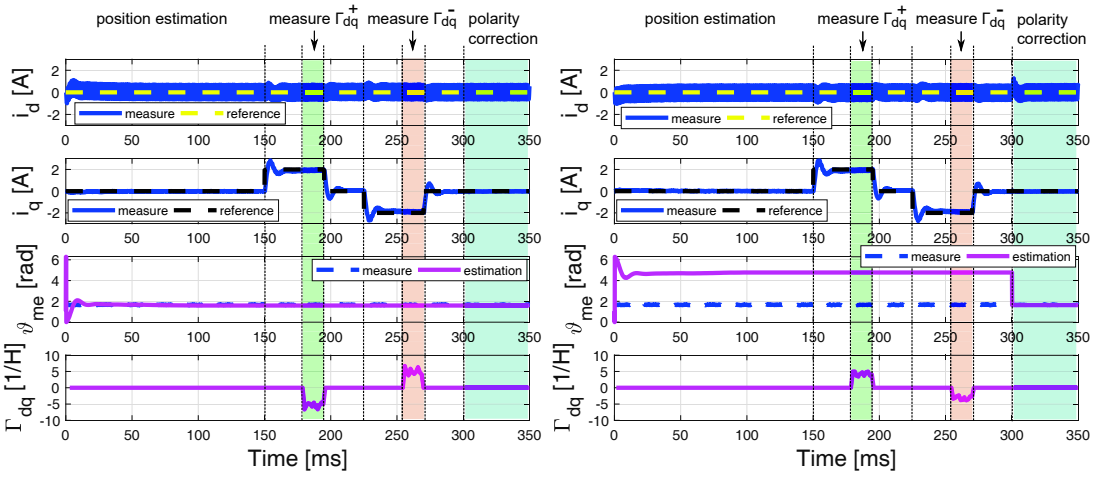

(a) Correct initial estimation (b) Incorrect initial estimation

Figure 4.13: Position and polarity estimation (experimental).

the saturation is avoided. Once a position estimation is achieved, its updating is stopped and the polarity recognition procedure starts. In Figure 4.12(a) and Figure 4.13(a) the correct initial estimation case is represented. A positive quadrature current reference is set and, only when the current is settled to the reference value, the parameter Γ_{dq} is measured obtaining a negative Γ_{dq}^{+}. Later by the repetition of this step with a negative current reference a positive Γ_{dq}^{-} is obtained. While these measurements are performed the d^x axis current is controlled to zero so that its value does not influence the parameter Γ_{dq}. In fact in Figure 4.12 and Figure 4.13 only the high frequency current component is present in the direct axis. Finally the measurements Γ_{dq}^{+} and Γ_{dq}^{-} are compared through the computation of $\Delta\Gamma$ that is negative in this situation so no polarity correction is needed. On the contrary when the initial polarity is wrong (Figure 4.12(b) and Figure 4.13(b)) the measurements of Γ_{dq}^{+} and Γ_{dq}^{-} result in a positive $\Delta\Gamma = \Gamma_{dq}^{+} - \Gamma_{dq}^{-}$

therefore the polarity is corrected by adding π in the estimated electrical position.

Once again it is worth to notice how Γ_{dq} reverses its sign according to the one of the current. Moreover also the comparison between Figure 4.12 and Figure 4.13 confirms that, for the same current reference, Γ_{dq} reverses its sign depending on the correctness of the initial position estimation. Finally a good agreement between the simulation and experimental results should be noticed.

4.6. Extension to non locked rotor case

Since the rotor position can not be estimated while the polarity detection is performed and the parameter Γ_{dq} can be measured correctly only with $\Delta\vartheta = 0$ e $\Delta\vartheta = \pi$, only limited movement of the rotor are allowed during the proposed procedure. In order to determine whether the rotor has to be locked two parameters are introduced: the start-up time (i.) and the Γ_{dq} measurement time (ii.). The parameter (i.) is defined in (4.13) as the time necessary to accelerate a motor of inertia J from standstill to the rated speed Ω_N, applying the rated torque M_N.

$$T_A = \frac{\Omega_N J}{M_N} \tag{4.13}$$

The second parameter (ii.) is the minimum time necessary to measure Γ_{dq}. Since Γ_{dq} is measured considering the amplitude of a sinusoidal signal with frequency ω_h, at least ten periods have to be acquired. Therefore (ii.) is defined as in (4.14).

$$T_\Gamma = 10\frac{2\pi}{\omega_h} = \frac{10}{f_h} \tag{4.14}$$

The machine used for the experimental results is characterised by a low inertia $J = 2 \times 10^{-4}$ kgm^2 while the maximum ω_h achievable with a sinusoidal injection and a switching frequency of the inverter of 10 kHz is $f_h = 1$ kHz so (i.) and (ii.) are respectively $T_A = 3.8$ ms and $T_\Gamma = 10$ ms. Since $T_A < T_\Gamma$ it is not possible to perform the polarity detection unless the rotor moves excessively and the rotor has to be locked. This can be done for all the applications provided with a brake, such as wind turbine and elevators. However if the machine inertia is sufficiently higher the test can be carried out with no locked rotor. The simulations in Figure 4.14 has been done considering a machine with a higher inertia $J = 5 \times 10^{-2}$ kgm^2. It can be seen that during the test the rotor electrical speed does not exceed 1 rad/s leading to a movement of some electrical degrees of the rotor. In this condition $\Delta\vartheta \approx 0$ or $\Delta\vartheta \approx \pi$ and the test can be performed without loosing effectiveness.

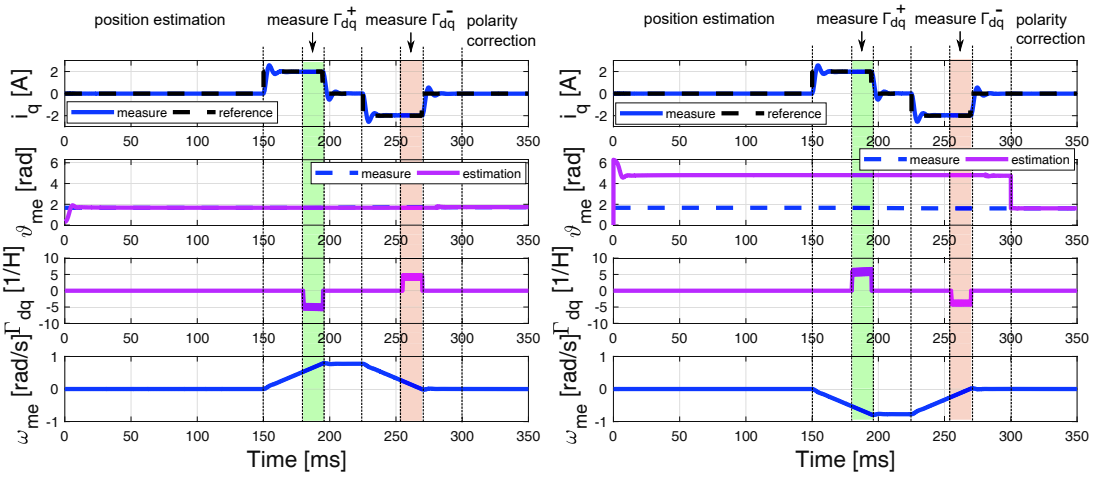

(a) Correct initial estimation

(b) Incorrect initial estimation

Figure 4.14: Polarity estimation with no locked rotor (simulation).

4.7. Conclusions

This chapter described a new method for polarity detection in locked rotor IPMSM. It has been demonstrated that the properties of the differential cross-saturation inductance can be exploited to extract information about the correct direction of the estimated d axis. In particular it has been shown through experimental results that the sign of the mutual inductance, or equivalently the one of the reciprocal inductance, changes when the quadrature current sign reverses and when the initial polarity estimation is incorrect. Therefore measuring the reciprocal inductance allows to effectively recognise and correct a possible error in the initial position estimation. The experimental tests confirmed the effectiveness of the suggested polarity detection method and that it is valid for every rotor electrical position. Moreover it has been shown that the proposed strategy can be easily combined with the high frequency voltage injection based sensorless technique.

Chapter 5

Convergence of HF voltage injection in heavily saturated machines

Iron saturation affects the high frequency voltage injection position estimation worsening its performance. In case of heavily saturated machine the estimation algorithm could even become unstable due to the absence of convergence points. This chapter examines the problem of convergence in synchronous reluctance motors since this kind of machine is considerably affected by iron saturation. Moreover it proposes a comparison between different methods to enhance the high frequency voltage injection estimation convergence range.

5.1. Introduction

It is well known that iron saturation, and in particular the resulting cross-saturation, reduces the effectiveness of the high frequency voltage injection position estimation algorithm. In particular the mutual coupling between the d and q axes causes a constant position estimation error [50, 51, 53]. This error depends on the saturation condition of the machine and thus on its working point.

In literature the position estimation error influence on the working point of the machine is usually neglected. Due to the presence of an estimation error, the machine operating point does not correspond to the reference leading to a different saturation condition that the expected one. The different machine saturation, and consequently its inductances value, modify in turn the estimation error. So there exists a loop interaction between the estimation error and the actual machine operating point that has to be investigated in order to deeply understand the convergence of the high frequency voltage injection algorithm. To the author's best knowledge the only paper addressing this effect is [54]. This work investigate the case an IPMSM in heavily saturation condition showing the lack of the self-sensing capability in overload condition.

The most common technique used to limit the effect of iron saturation on the estimation algorithm consists in adding a compensation angle, or equivalently tilt the high frequency voltage vector, in order to correct the estimated position [55–57]. A

different method relying on a twofold compensation was proposed in [54]. This solution was demonstrated to effective in both correcting the estimation error and extending the self-sensing feasibility range. It is worth noticing that all these compensations and analysis rely on a precise knowledge of the magnetic characteristics of the machine.

In this chapter the convergence of the high frequency voltage injection position estimation algorithm is examined in depth. The analysis is focus on synchronous reluctance machines. This kind of motors are a perfect case study since among the synchronous machines are the most affected by the iron saturation phenomenon. In fact, from a design point of view, in a SyRM the iron saturation of the rotor channels is desirable in order to obtain a high power factor. Finally a comparison between different compensations to enhance the self-sensing convergence range is proposed.

5.2. Position estimation convergence existence

The performance of the high frequency voltage injection position estimation is strongly related to the iron saturation effect. In fact it is well known that in presence of cross-saturation the estimation is affected by an error since the algorithm converges to an incorrect position, as explained in chapter 4. In this section a deep analysis of the position estimation convergence is carried out. At the beginning some simplifying assumptions, such as no iron saturation and constant inductances, are considered in order to ease the comprehension of the topic and allow to accustom the reader to the graphs used in this chapter. These assumptions are subsequently removed and an investigation of the algorithm convergence when applied to a real machine is given. As the analysis carried out in this chapter is focused on synchronous reluctance machines the high frequency voltage injection is carried out along the estimated quadrature axis q^x in order to limit the ripple induced in the torque. The estimation algorithm will thus nullify the high frequency direct component of the current I_{hd} which has the same expression of I_{hq} described in (4.6), therefore the general analysis of the estimation algorithm in chapter 4 stands also in this case. More details and a comparison between the injection on direct and quadrature axis is reported in the Appendix.

5.2.1. Ideal case: constant inductances

First of all the dependence of the inductance on the working point is neglected and a model of a linear machine with constant inductances ℓ_d, ℓ_q and ℓ_{dq} is considered. The inductance ℓ_Δ is defined as $(\ell_q - \ell_d)/$. In this case the amplitude of the high frequency d current response is (5.1). It is worth noticing that in this case, once that the injection parameters ω_h and U_h are fixed, I_{hd} depends only on the estimation error $\Delta\vartheta$.

$$I_{hd} = \frac{U_h[\ell_\Delta \sin(2\Delta\vartheta) + \ell_{dq}\cos(2\Delta\vartheta)]}{\omega_h(\ell_{dq}^2 - \ell_d\ell_q)} \tag{5.1}$$

Since the observer tries to nullify I_{hd} the estimation algorithm converges to the values of $\Delta\vartheta$ that are solutions of the equation (5.2).

$$\tan(2\Delta\vartheta) = -\frac{\ell_{dq}}{\ell_\Delta} \tag{5.2}$$

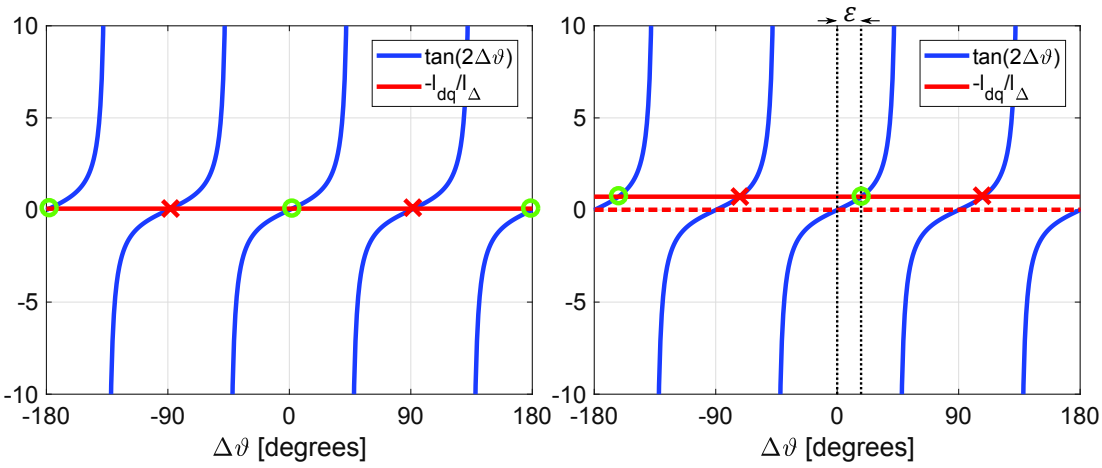

(a) $\ell_{dq} = 0$ (b) $\ell_{dq} \neq 0$

Figure 5.1: Graphical solutions of (5.2).

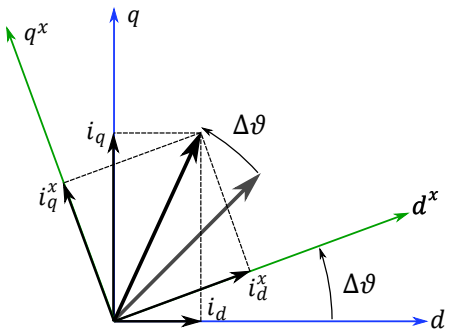

Figure 5.2: Working point in presence of estimation error.

Figure 5.1 shows the graphical solutions of the equation. The first member is reported in blue while the red line represents the second one. In Figure 5.1(a) the case in which the cross-coupling is not present, i.e. $\ell_{dq} = 0$, is represented. It can be noticed that the two curves cross in four points which are the four convergence points of the algorithm: two stable, corresponding to $\Delta\vartheta = 0°$ and $\Delta\vartheta = \pm 180°$, and two unstable, corresponding to $\Delta\vartheta = 90°$ and $\Delta\vartheta = -90°$, as already described in chapter 4. So when $\ell_{dq} = 0$ the algorithm converges to the correct rotor position (except for the magnet polarity ambiguity that, in the case of an IPMSM, can be solved as explained in chapter 4). Figure 5.1(b) shows the case of mutual coupling between d and q axes, i.e. $\ell_{dq} \neq 0$. In this case the red line representing $-\ell_{dq}/\ell_{\Delta}$ is shifted upwards so it does not cross the curve $\tan(2\Delta\vartheta)$ in correspondence of $\Delta\vartheta = 0°$ and error $\epsilon = \frac{1}{2}\operatorname{atan}(-\ell_{dq}/\ell_{\Delta})$ affects the position estimation.

The sensorless drive works in the estimated reference frame $d^x q^x$ where the current components, i_d^x, i_q^x, are forced to track their references i_d^*, i_q^*. So, assuming steady state operation for the current loops, $i_d^x = i_d^*$ $i_q^x = i_q^*$. Therefore actual currents i_d and i_q are

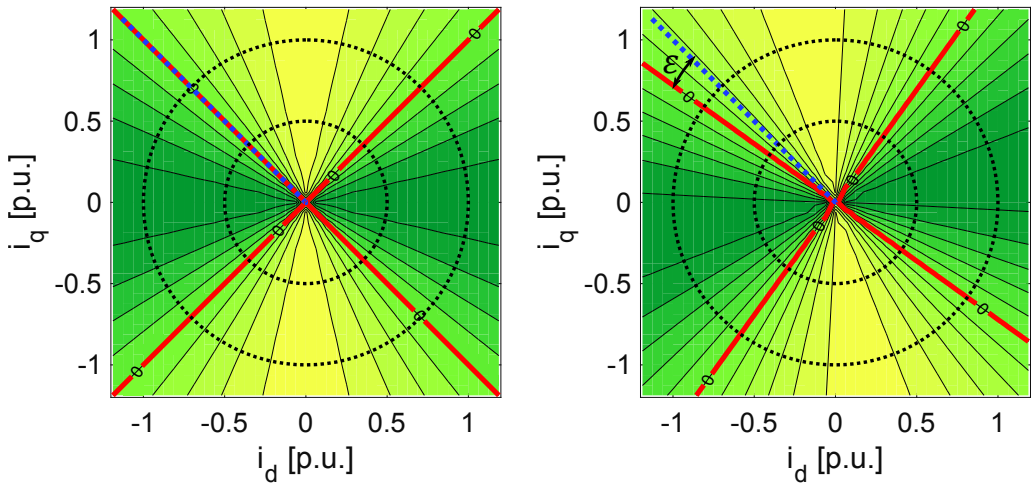

(a) $\ell_{dq} = 0$ (b) $\ell_{dq} \neq 0$

Figure 5.3: Theoretical I_{hd} map.

related to the desired one i_d^* and i_q^* through a rotation of $\Delta\vartheta$ according to (5.3).

$$\begin{bmatrix} i_d \\ i_q \end{bmatrix} = \begin{bmatrix} \cos(\Delta\vartheta) & -\sin(\Delta\vartheta) \\ \sin(\Delta\vartheta) & \cos(\Delta\vartheta) \end{bmatrix} \begin{bmatrix} i_d^* \\ i_q^* \end{bmatrix} = \begin{bmatrix} f(\bar{i}^*, \Delta\vartheta) \\ g(\bar{i}^*, \Delta\vartheta) \end{bmatrix} \tag{5.3}$$

For each value of required current torque, the reference working point $\bar{i}^* = (i_d^*, i_q^*)$ is univocally determined to achieve the MTPA operation, while the working point in the actual rotor reference frame, $\bar{i} = (i_d, i_q)$, tracks a circumference counter-clockwise as $\Delta\vartheta$ is increasing starting from the MTPA point, as shown in Figure 5.2. The circumference amplitude increases with the modulus of the required torque. Therefore each point of the i_d-i_q current plane could be reached during sensorless operation varying $\Delta\vartheta$ and the required torque level, even if the reference is forced along the MTPA.

Figure 5.3 represents a I_{hd} map on the current plane i_d-i_q in the reference frame synchronous with the rotor. The figure was obtained considering a synchronous reluctance machine and its MTPA trajectory, indicated with a dotted blue line, as reference for the current vector. The red lines highlight the points of the plane where $I_{hd} = 0$, so all the possible convergence points of the estimation algorithm. In particular the stable converge points are the ones characterised by a negative derivative. The two dotted black circumferences indicate the working points obtained for different required torque level varying the estimation error $\Delta\vartheta$. It can be noticed that each circumference intersects the $I_{hd} = 0$ locus four times showing once again that the estimation algorithm features four convergence point. In Figure 5.3(a) the case in which $\ell_{dq} = 0$ is analysed. Part of the $I_{hd} = 0$ locus coincides with the MTPA trajectory. It means that for every torque request the algorithm converges at $\Delta\vartheta = 0$, as expected, and that during the sensorless operation the actual machine working point is correctly controlled and coincides with its reference. In Figure 5.3(b) the case of mutual coupling between the axes, i.e. $\ell_{dq} \neq 0$, is reported. It can be noticed that the effect of ℓ_{dq} is to rotate the I_{hd} map. In this case the $I_{hd} = 0$ locus does not cross the MTPA meaning that a constant error ϵ affects the position estimation leading to an incorrect control of the machine. In particular the

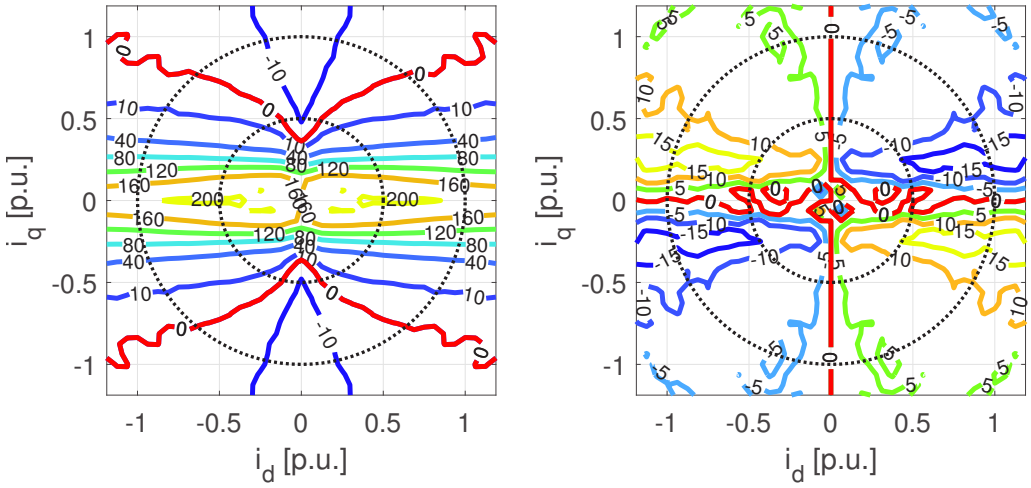

(a) ℓ_Δ[mH] (b) ℓ_{dq}[mH]

Figure 5.4: Differential inductances map of a SyRM according to IPMSM *d-q* axes convention.

actual machine working point (red lines) is different from the desired one (blue dotted line, i.e. MTPA points).

5.2.2. General case: real machine

Constant inductances have been considered so far, however in a real machine the inductances depend on the working point (5.4), as explained in chapter 4.

$$\ell_d(i_d, i_q) \qquad \ell_q(i_d, i_q) \qquad \ell_{dq}(i_d, i_q) \qquad \ell_\Delta(i_d, i_q) \tag{5.4}$$

During sensorless operations the presence of an estimation error causes a difference between the desired currents and the actual ones implying that the saturation condition of the machine changes with the estimation error. In particular the inductances can be rewritten according to (5.3) as functions of the reference current vector and of the estimation error $\Delta\vartheta$ (5.5). The dependence on the current angle can be neglected since it is assumed to be chosen equal to the MTPA angle which is fixed for every current amplitude.

$$\ell_d(|i^*|, \Delta\vartheta) \qquad \ell_q(|i^*|, \Delta\vartheta) \qquad \ell_{dq}(|i^*|, \Delta\vartheta) \qquad \ell_\Delta(|i^*|, \Delta\vartheta) \tag{5.5}$$

The behaviour of ℓ_Δ and ℓ_{dq} of the SyRM considered in this chapter are reported in Figure 5.4(a) and Figure 5.4(b) respectively. The differential inductance values are obtained from the measured magnetic characteristics of the machine. In the figures two circumferences are plotted: they correspond to the possible machine working points varying $\Delta\vartheta$ when the nominal current, $|i^*| = 1$ p.u., and half of the nominal current, $|i^*| = 0.5$ p.u., is required. In Figure 5.5 the inductances along the two circumferences are reported: a great excursion of the inductance values can be noticed.

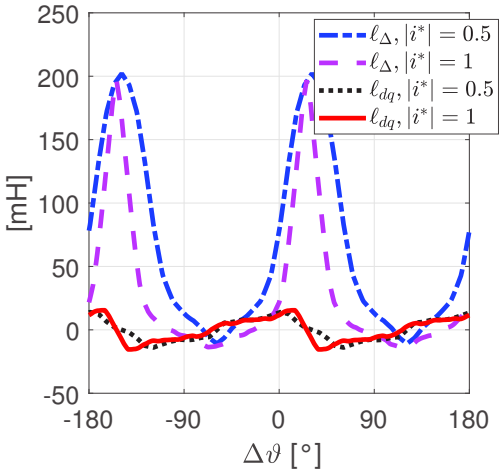

Figure 5.5: ℓ_Δ and ℓ_{dq} as functions of the estimation error $\Delta\vartheta$.

The high frequency d current amplitude I_{hd} can be rewritten, in light of (5.5), as in (5.6) where the dependence on the estimation error and on the desired current vector amplitude is highlighted.

$$I_{hd}(|i^*|, \Delta\vartheta) = \frac{U_h[\ell_\Delta(|i^*|, \Delta\vartheta)\sin(2\Delta\vartheta) + \ell_{dq}(|i^*|, \Delta\vartheta)\cos(2\Delta\vartheta)]}{\omega_h[\ell_{dq}^2(|i^*|, \Delta\vartheta) - \ell_d(|i^*|, \Delta\vartheta)\ell_q(|i^*|, \Delta\vartheta)]} \tag{5.6}$$

The observer tries to nullify I_{hd} so the estimation algorithm converges to values of $\Delta\vartheta$ which are solutions of the equation (5.7). If for a fixed $|i^*|$ the inductances ℓ_Δ and ℓ_{dq} are constant there always exist a value of $\Delta\vartheta$ for which (5.7) is satisfied, as shown previously. However in this case the convergence existence of the estimation algorithm deeply relies on the ℓ_Δ and ℓ_{dq} behaviour varying $\Delta\vartheta$.

$$\tan(2\Delta\vartheta) = -\frac{\ell_{dq}(|i^*|, \Delta\vartheta)}{\ell_\Delta(|i^*|, \Delta\vartheta)} \tag{5.7}$$

Figure 5.6 shows the graphical solutions of equation (5.7) for different values of the reference current amplitude $|i^*|$. In Figure 5.6(a) half of the nominal current is required, i.e. $|i^*| = 0.5$ p.u.. In this case four solutions of (5.7) can be found and an error ϵ due to the cross-saturation affects the position estimation similarly to what was described in Figure 5.1(b). Differently in Figure 5.6(b) where $|i^*| = 1$ p.u. the curves representing $\tan(2\Delta\vartheta)$ and $-\ell_{dq}(|i^*|, \Delta\vartheta)/\ell_\Delta(|i^*|, \Delta\vartheta)$ never cross meaning that in this condition the position estimation does not have any convergence point.

Knowing the inductances behaviour from the measured magnetic characteristics, the current I_{hd} has been calculated in each different point of the i_d-i_q plane using (5.6). The I_{hd} map is reported in Figure 5.7(a) and it is obtained considering $\bar{i}^*$ on the MTPA locus on the first quadrant in order to obtain a positive torque. Specular and sign-inverted map applies for negative torque. The same I_{hd} map has been measured applying a reference current vector and injecting hf voltages along an estimated q^x axis that rotates with respect to the actual q axis in order to simulate an increasing estimation error. The position of q^x has been used for the transformation of the current from stator to rotor reference frame recreating the sensorless working condition of the

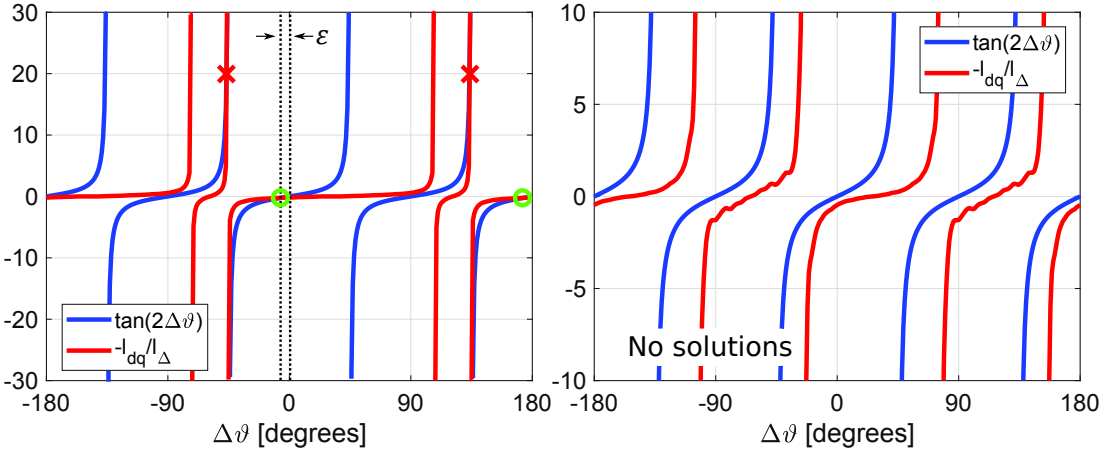

(a) $|i^*| = 0.5$ p.u. (b) $|i^*| = 1$ p.u.

Figure 5.6: Differential inductances of the SyRM.

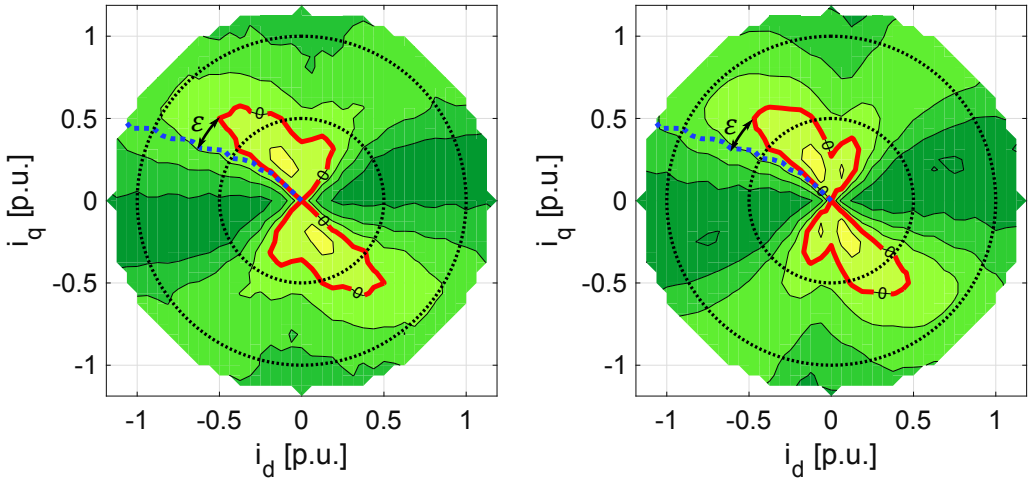

(a) Theoretical (b) Measured

Figure 5.7: I_{hd}[mA] map.

drive. This I_{hd} map is reported in Figure 5.7(b). Slight differences between the two figures can be due to the discretisation and interpolation of the magnetic characteristics used to obtain Figure 5.7(a). As this figure has been calculated theoretically using (5.6) it neglects some effects such as resistive voltage drop due to the hf injection or the inverter non-linearities. Moreover Figure 5.7(b), differently from Figure 5.7(a), does not take into account the airgap flux harmonics since the measurement has been carried out with the rotor fixed in a particular position. In both Figure 5.7(a) and Figure 5.7(b) the MTPA locus is indicated in blue. Furthermore the $I_{hd} = 0$ locus is highlighted in red. The possible stable convergence points are included in this locus and precisely are the ones in which I_{hd} has a negative derivative. The inner circumference is obtained for a required current $|i^*| = 0.5$ p.u. and crosses the $I_{hd} = 0$ locus in correspondence of four different $\Delta\vartheta$ values. The four zero crossing points can be noticed also in Figure 5.8 where I_{hd} along the two circumferences is plotted. The two stable points are the ones with a negative derivative. Differently the outer circumference, which is obtained at $|i^*| = 1$ p.u., does not cross the $I_{hd} = 0$ locus since the current is negative for each $\Delta\vartheta$, as can be seen in Figure 5.8, so the self-sensing algorithm does not converge. In the SyRM considered in this chapter the position estimation algorithm converges only when the torque is lower or equal to the 68% of the nominal value. So it can be noticed that the convergence issue can be more severe in SyRMs that in IPMSM. In fact in [54] the overload operation is considered while in this chapter the position estimation does not converge within the nominal operation range of the machine.

It is important to highlight that the convergence analysis carried out in this chapter is done assuming the current reference on the MTPA. If another reference is chosen the functions describing the inductances ℓ_{dq} and ℓ_{Δ} varying $\Delta\vartheta$ change. Therefore the convergence analysis has to be repeated since the solutions of (5.7) could be different and the convergence range could even increase or decrease.

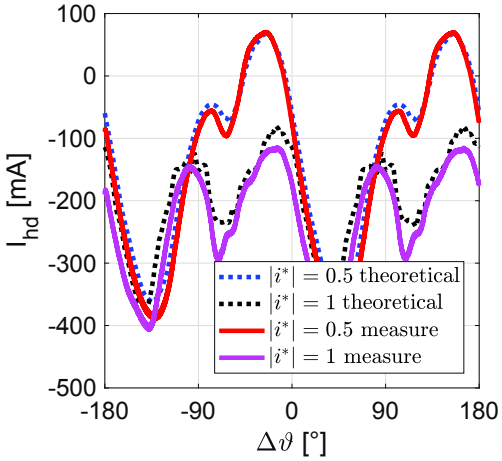

Figure 5.8: I_{hd}^{in} along the circumferences.

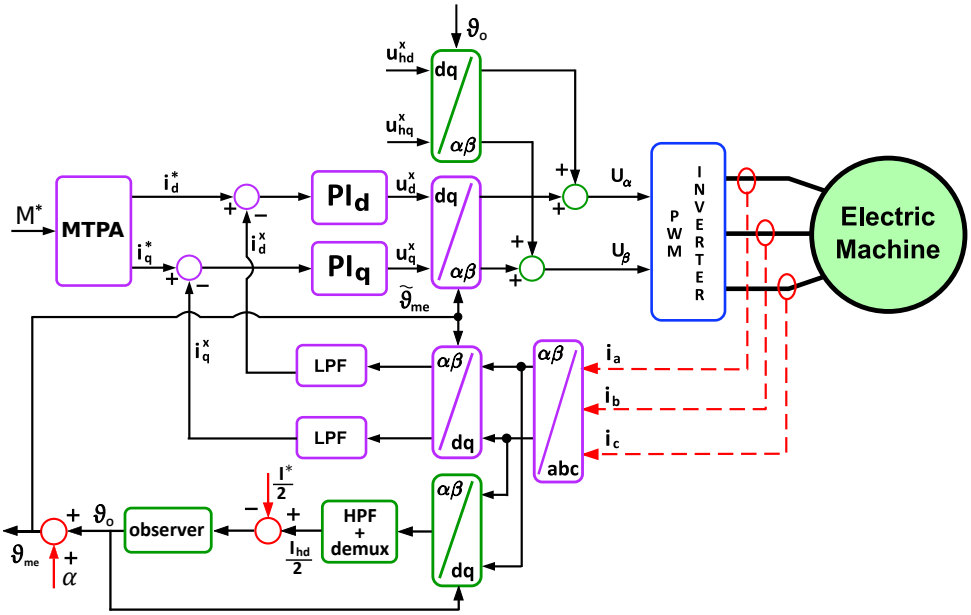

Figure 5.9: Control scheme with compensations.

5.3. Extension of the convergence range

In this section different techniques to solve the convergence problem are analysed. The compensations analysed in this chapter are shown in Figure 5.9 where they are highlighted in red. They consists of a current and an angle compensation and they are examined both individually and together. The compensations purpose is to modify the waveform of the observer input I_{hd}^{in} in order to guarantee the estimation convergence in $\Delta\vartheta = 0$.

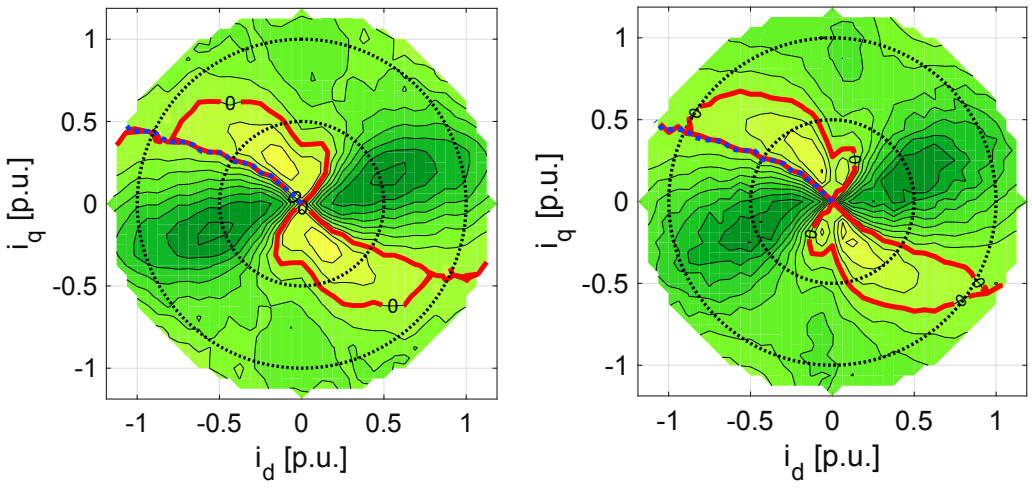

(a) Theoretical (b) Measured

Figure 5.10: I_{hd}^{in}[mA] map with angle compensation.

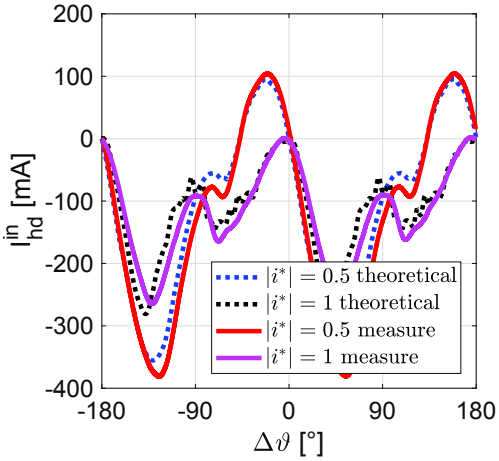

Figure 5.11: I_{hd}^{in} along the circumferences with angle compensation.

The convergence issue of the high frequency self-sensing algorithm is closely related to the cross-saturation effect. In fact, if ℓ_{dq} is identically zero, I_{hd} presents zero-crossing points for each torque value and the estimation error at the convergence point ϵ is null. In many papers [55–57] the cross-saturation effect and the consequent estimation error are compensated calculating the estimated position $\tilde{\vartheta}_{me}$ as the sum of an angle α and the output of the two-state observer ϑ_o as shown in Figure 5.9. In this case the high frequency current amplitude expression is the one in (5.8).

$$I_{hd}^{\text{in}}(|i^*|,\Delta\vartheta,\alpha) = \frac{U_h[\ell_\Delta(|i^*|,\Delta\vartheta)\sin(2(\Delta\vartheta-\alpha)) + \ell_{dq}(|i^*|,\Delta\vartheta)\cos(2(\Delta\vartheta-\alpha))]}{\omega_h[\ell_{dq}^2(|i^*|,\Delta\vartheta) - \ell_d(|i^*|,\Delta\vartheta)\ell_q(|i^*|,\Delta\vartheta)]} \tag{5.8}$$

The angle α should be calculated in order to obtain a null I_{hd}^{in} in correspondence of a correct estimation, i.e. the condition $I_{hd}^{\text{in}}(|i^*|,0,\alpha) = 0$ has to be satisfied. It can be

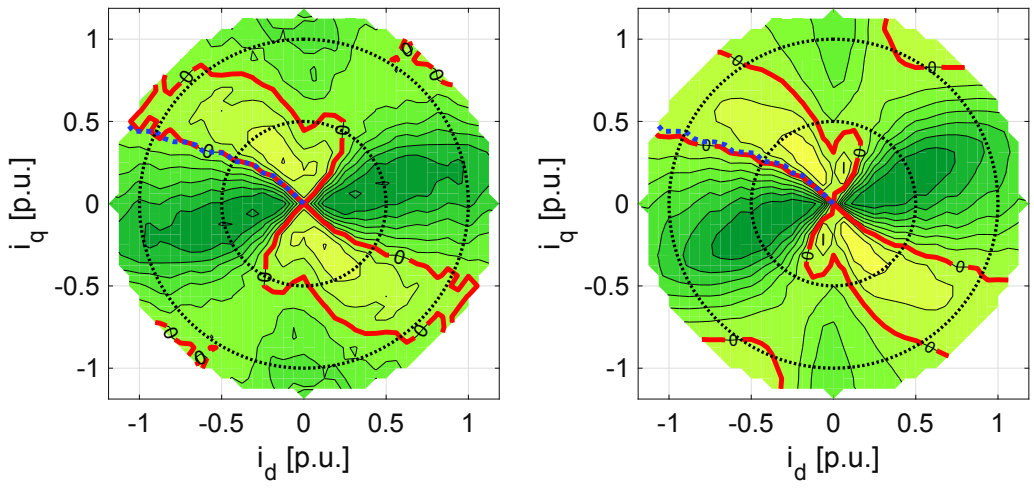

(a) Theoretical (b) Measured

Figure 5.12: I_{hd}^{in}[mA] map with current compensation.

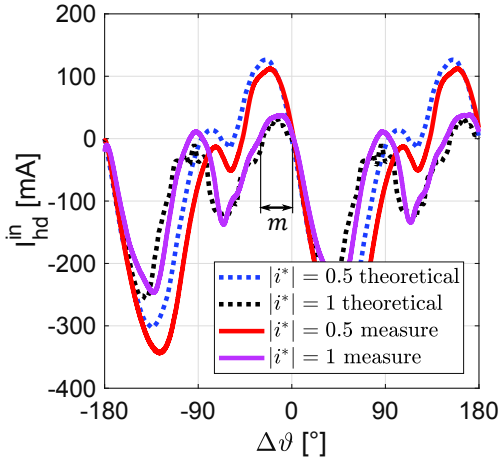

Figure 5.13: I_{hd}^{in} along the circumferences with current compensation.

proved that this condition leads to the compensation angle in (5.9) that is twice the opposite of the expected estimation error ϵ in the desired working point $|i^*|$.

$$\alpha(|i^*|) = -\epsilon(|i^*|, 0) \tag{5.9}$$

For every torque request is always possible to determine a compensation angle such that nullifies the high frequency current amplitude when the estimation error is zero. In Figure 5.10(a) and Figure 5.10(b) the theoretical and measured I_{hd}^{in} map are reported. The zero crossing points exist for every torque reference and the MTPA coincides with the $I_{hd}^{\text{in}} = 0$ locus however this compensation is not sufficient to guarantee the convergence of the estimation algorithm. In fact the I_{hd}^{in} zero crossing point must also be stable, i.e. the I_{hd}^{in} must have a negative derivative in $\Delta\vartheta = 0$. In Figure 5.11 the high frequency current amplitude obtained with the angle compensation at the nominal current has been plotted. In $\Delta\vartheta = 0$ the current is zero but it is not a stable convergence point.

The second compensation strategy which is analysed consists on introducing a sort of high frequency current amplitude reference I^* as described in Figure 5.9. The input of the two-state observer I_{hd}^{in} is calculated as the difference between I_{hd} and I^*. With this second type of compensation the high frequency current amplitude is as in (5.10).

$$I_{hd}^{\text{in}}(|i^*|, \Delta\vartheta, I^*) = \frac{U_h[\ell_\Delta(|i^*|, \Delta\vartheta)\sin(2\Delta\vartheta) + \ell_{dq}(|i^*|, \Delta\vartheta)\cos(2\Delta\vartheta))]}{\omega_h[\ell_{dq}^2(|i^*|, \Delta\vartheta) - \ell_d(|i^*|, \Delta\vartheta)\ell_q(|i^*|, \Delta\vartheta)]} - I^* \tag{5.10}$$

Taking the current reference I^* as in (5.11) allows to fulfil the condition $I_{hd}^{\text{in}}(|i^*|, 0, I^*) = 0$ and thus obtain a null current at the 2-state observer input in correspondence of a null estimation error.

$$I^*(|i^*|) = I_{hd}(|i^*|, 0) \tag{5.11}$$

Figure 5.12(a) and Figure 5.12(b) show the I_{hd}^{in} map where zero crossing points exist for every reference torque value. In Figure 5.13 the resulting high frequency current amplitude at the nominal current is reported. The convergence point in $\Delta\vartheta = 0$ is stable. To further analyse the stability of this solution the concept of convergence interval m is introduced. It is defined as the distance of the convergence point from the nearest zero-crossing point and it is indicated in Figure 5.13. It is very important to

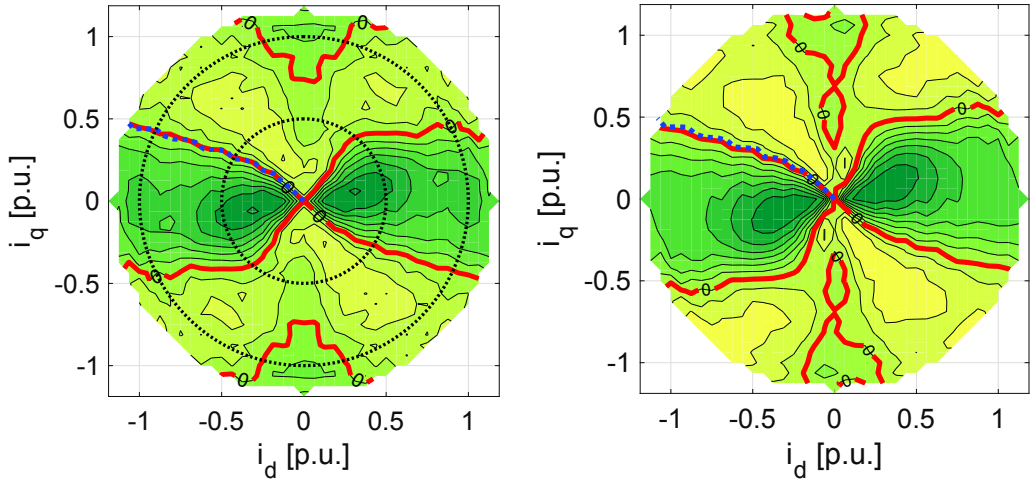

(a) Theoretical (b) Measured

Figure 5.14: I_{hd}^{in}[mA] map with both the compensations.

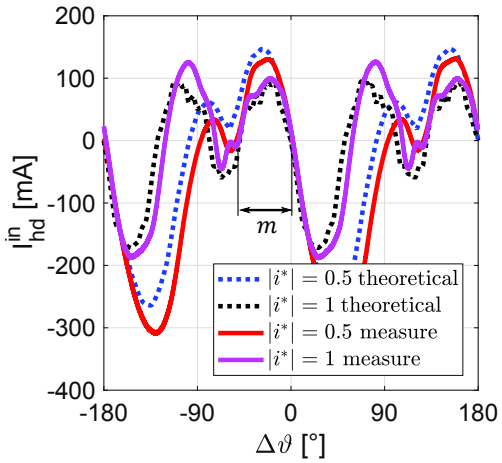

Figure 5.15: I_{hd}^{in} along the circumferences with both the compensations.

have a sufficiently large convergence interval in order to keep $\Delta\vartheta$ inside this interval also during transients. Otherwise the working point slides till the next convergence point and this is not acceptable during the drive operation. With only one compensation parameter (α or I^*) it is possible to force a zero crossing point in $\Delta\vartheta = 0$ but not to impose its stability or maximise its convergence interval.

In [54] a solution consisting in a twofold action that combines the angle compensation and the high frequency current amplitude reference is proposed. In this case the high frequency current amplitude expression is the one in (5.12).

$$I_{hd}^{\text{in}}(|i^*|, \Delta\vartheta, \alpha, I^*) = \frac{U_h[\ell_\Delta(|i^*|, \Delta\vartheta)\sin(2(\Delta\vartheta - \alpha)) + \ell_{dq}(|i^*|, \Delta\vartheta)\cos(2(\Delta\vartheta - \alpha))]}{\omega_h[\ell_{dq}^2(|i^*|, \Delta\vartheta) - \ell_d(|i^*|, \Delta\vartheta)\ell_q(|i^*|, \Delta\vartheta)]} - I^* \tag{5.12}$$

Differently from what happen with the compensations described so far, where only one

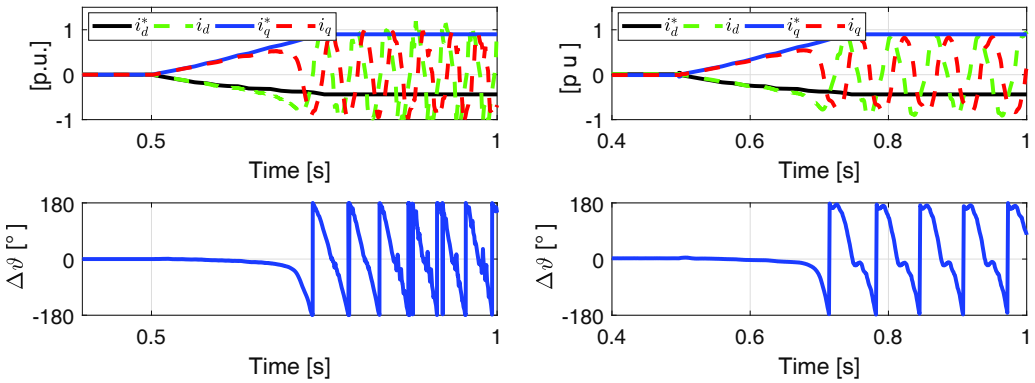

(a) Simulation (b) Experimental

Figure 5.16: Torque ramp simulation without compensation.

possible solution can be found, by forcing $I_{hd}^{\text{in}}(|i^*|, 0, \alpha, I^*) = 0$ a set of different solutions can be determined, as shown in (5.13).

$$\begin{aligned} I^*_{\text{max}} &= \frac{U_h \sqrt{\ell^2_\Delta(|i^*|, 0) + \ell^2_{dq}(|i^*|, 0)}}{\omega_h [\ell^2_{dq}(|i^*|, 0) - \ell_d(|i^*|, 0)\ell_q(|i^*|, 0)]} \\ I^*(|i^*|) &\in [-I^*_{\text{max}}; I^*_{\text{max}}] \\ \alpha(|i^*|) &= -\epsilon(|i^*|, 0) + \frac{1}{2}\text{asin}\left(\frac{I^*(|i^*|)}{I^*_{\text{max}}}\right) \end{aligned} \tag{5.13}$$

The stable solution with the highest convergence interval has been chosen and the correspondent I_{hd}^{in} map has been reported in Figure 5.14(a) and Figure 5.14(b) while in Figure 5.15 the high frequency current amplitude at the nominal torque is reported. In both the maps stable solutions characterised by a high convergence interval can be noticed. Once again the small differences between the theoretical and the measured I_{hd}^{in} are due to the discretisation and interpolation of the magnetic characteristics to the effect of the flux harmonics taken into account only in the first case.

5.4. Simulations and experiments

Some simulation and experimental tests have been carried out in order to validate the results presented so far. In Figure 5.16(a) a simulation with a required current varying from zero to the nominal value is performed. For the simulation a machine model that implements the measured magnetic characteristic has been realised. During the simulation the speed of the motor is kept equal to zero. The loss of the self-sensing capability can be noticed when the required current reaches the 70% of the nominal value, confirming the prediction made in section 5.2. In Figure 5.16(b) the same test has been carried out experimentally leading to similar results.

The angle compensation has been implemented both in simulation and on the test bench and a similar test is carried out. The required current is increased with a ramp along the MTPA locus in the first quadrant until the nominal current is reached. Then

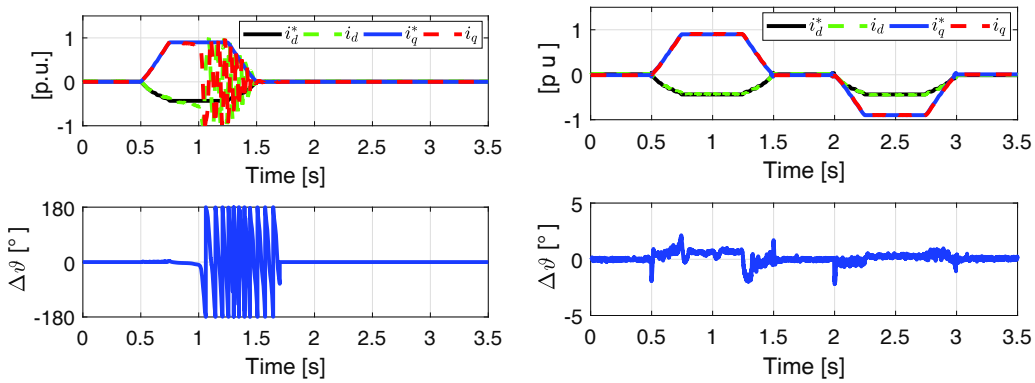

(a) Simulation (b) Experimental

Figure 5.17: Torque ramp simulation with angle compensation.

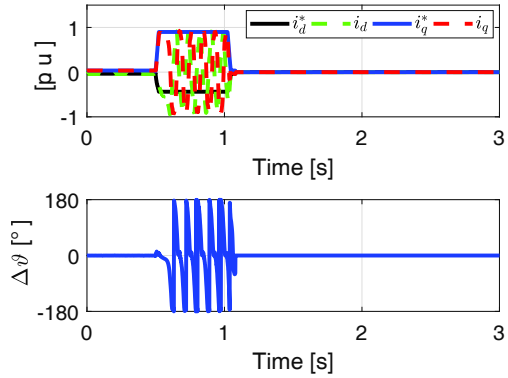

Figure 5.18: Fast torque ramp with angle compensation (experimental).

the ramp is repeated tracking the MTPA in the second quadrant in order to produce negative torque. In Figure 5.17(a) and Figure 5.17(b) the results of the simulation and of the experimental test are reported and have quite different results. In the simulation when the nominal current is applied after some time the position estimation fails and the control of the drive is lost. Differently the experimental test has been completed maintaining a precise position tracking. This difference can be explained comparing Figure 5.10(a) and Figure 5.10(b): in the first one m is null at the nominal current while in the second one a small convergence interval is still present. However the implementation on the test bench of the angle compensation is hardly stable. In fact in Figure 5.18, where a higher current dynamic is required, the position estimation fails and the system becomes unstable.

The current compensation has been also implemented and the test is repeated. As expected thanks to the compensation the estimation algorithm converges in the whole torque range of the machine with a limited position error both in simulation Figure 5.19(a) and during the experimental test Figure 5.19(b). Therefore the currents i_d and i_q are correctly regulated to their respective references. In Figure 5.20 a test with a faster current dynamic is reported. It can be notice that in this case the test is carried out without loosing stability differently from what happened with the angle compensation.

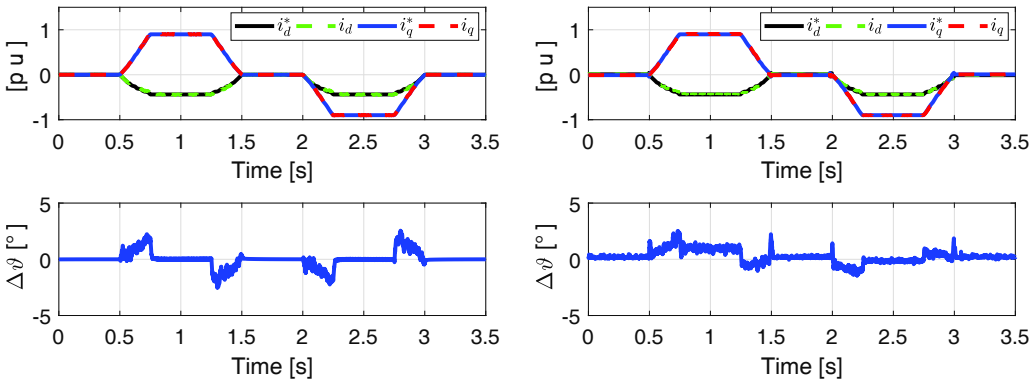

(a) Simulation (b) Experimental

Figure 5.19: Torque ramp simulation with current compensation.

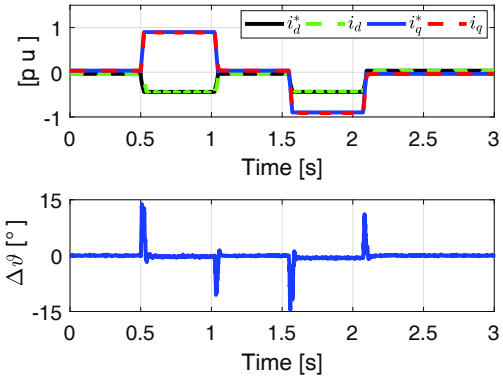

Figure 5.20: Fast torque ramp with current compensation (experimental).

The two compensations have been also applied together and the results are reported in Figure 5.21(a) and Figure 5.21(b). Also in this case the algorithm converges to the correct position in the whole current range allowing a precise control of the machine currents i_d and i_q. Only during transients a limited estimation error can be noticed. Figure 5.22 shows an experimental test where a higher current dynamics is required. Also in this case the double compensation is able to guarantee the stability of the sensorless drive. In Figure 5.23 a torque ramp is performed while the machine is dragged at a constant speed by a master motor. Some harmonics can be seen in the estimation error differently from the case of the test reported in Figure 5.21(b). They are due to magneto motive force spatial harmonics that lead to the variation of the inductances with the rotor position. As a consequence the high frequency d current amplitude I_{hd} depends on the position as shown in Figure 5.24 where a sixth harmonic can be noticed.

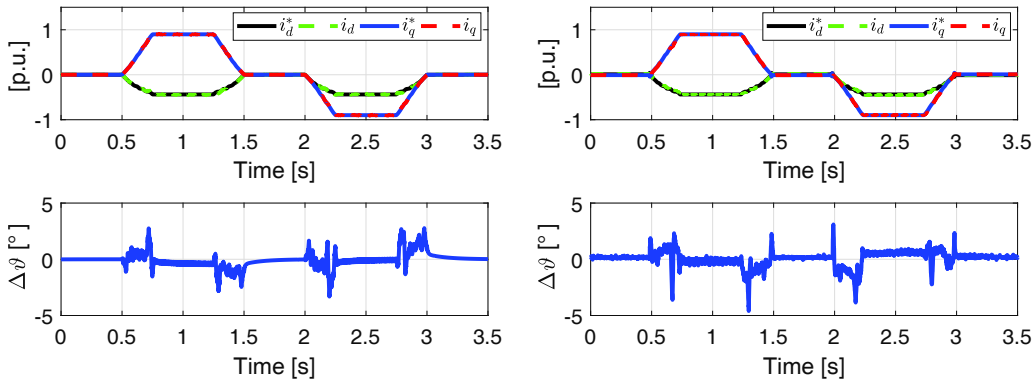

(a) Simulation (b) Experimental

Figure 5.21: Torque ramp simulation with both the compensations.

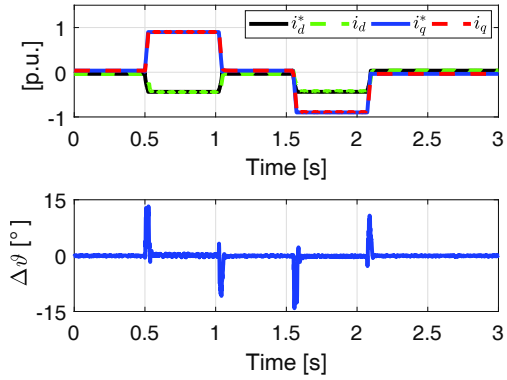

Figure 5.22: Fast torque ramp with both the compensations (experimental).

The dependency of the inductances and consequently of I_{hd} on the position has been neglected so far since it mildly affects the position estimation error as Figure 5.23 shows. However it is also possible to compensate this effect if the inductance behaviour varying the position is known [54].

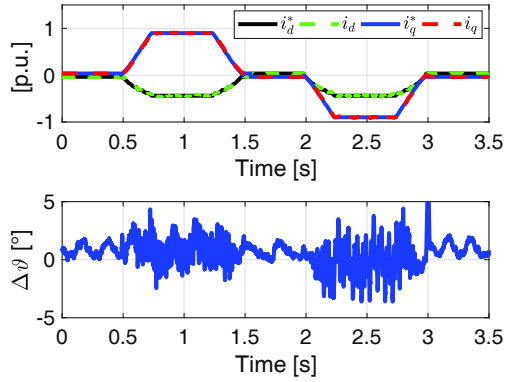

Figure 5.23: Torque ramp with both the compensations at $\omega_{me} = 20$ rad/s (experimental).

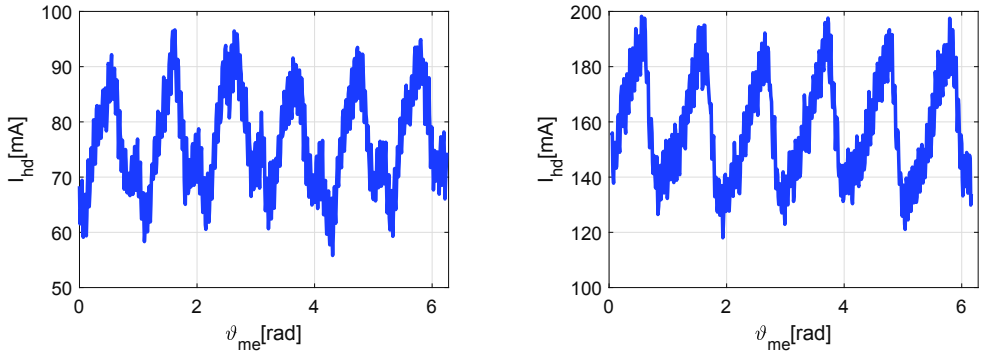

(a) $|i^*| = 0.5$ p.u. (b) $|i^*| = 1$ p.u.

Figure 5.24: Flux harmonics.

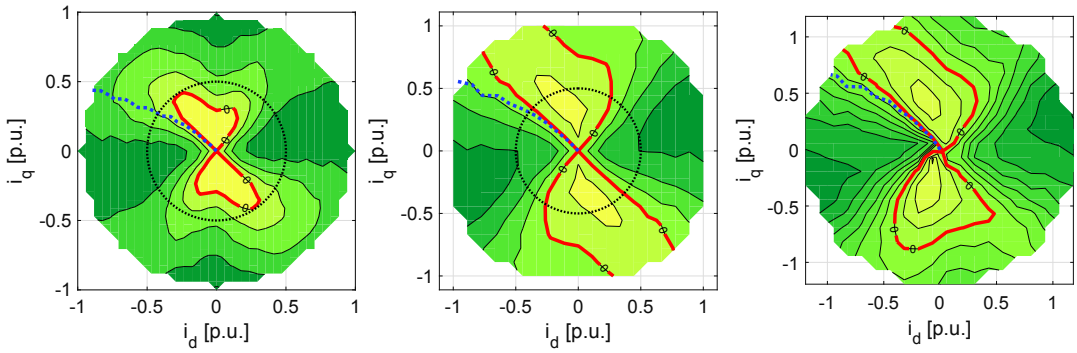

(a) SyRM 1 (b) SyRM 2 (c) IPMSM

Figure 5.25: Convergence map of other machines.

Finally the magnetic characteristics of other three machines have been used to study the convergence of the estimation algorithm and the resulting convergence maps for positive torque are reported in Figure 5.25. In the first case a SyRM is analysed and its convergence region hardly reaches half of the machine nominal current Figure 5.25(a). Differently the convergence region of the SyRM machine analysed in Figure 5.25(b) covers all the current range. The third map in Figure 5.25(c) refers to a IPMSM. It can be notices that the presence of the magnet makes the map asymmetric and that the convergence points are present also at the nominal torque. In the last two cases the angle compensation can be sufficient to obtain a stable and robust sensorless drive.

5.5. Conclusions

This chapter proposed a study and a deep insight of the convergence of the HF voltage injection position estimation algorithm in case of heavily saturated machines. Synchronous reluctance motors have been chosen as the case study since the iron saturation strongly affects this kind of machines. It has been shown that some SyRM lose their self-sensing capabilities also below their nominal current value. Moreover a comparison between different existing compensation methods to enhance the convergence range of the position estimation has been proposed. The results showed that the angle compensation, which is often used to correct the estimation error caused by the cross-saturation effect, could not be sufficient to make the sensorless drive stable and robust also when high torque is commanded. In this case also a current compensation has to be implemented.

Conclusions

In the first part of this work, a control scheme for wide speed range operation of a SyRM drive has been designed. The latter exploits the polar coordinate representation of the reference current vector to drive the machine along the most suitable trajectories according to torque and speed commands. An innovative voltage loop has been implemented together with CVC in the synchronous d-q reference frame, making it perfectly suitable for integration with traditional control schemes that are well-established in industry. The resulting control algorithm can drive the machine in the whole speed range while achieving the lowest power losses in every working condition. Besides, the algorithm can be used both with a linear approximation of MTPA and MTPV trajectories and with the actual ones considering iron saturation. A small signal analysis confirmed the stability of the control algorithm in every working condition.

This control strategy has been extended and adapted to the case of an IPMSM. The developed control algorithm keeps all the advantages of the one designed for SyRM drives: it can exploit the MTPV operation, the maximum efficiency is achieved at every working point, the structure of the proposed voltage loop can be easily integrated with standard control schemes and it is characterised by a low computational effort. Both simulations and experimental tests confirmed the effectiveness of the schemes.

Part of the research work was focused on the analysis of sensorless operation of synchronous machine drives. The high frequency voltage injection position estimation has been studied, and particular attention has been given to its convergence in case of heavily saturated machine. A method to analyse the self-sensing capability of synchronous machines and to predict their convergence range has been studied. A comparison between different compensation methods to enhance the convergence range in heavily saturated machine has been presented. The angle compensation, which is often used to correct the estimation error caused by the cross-saturation effect, could not be enough to make the sensorless drive stable and robust also when high current is commanded. In this case also a current compensation must be implemented. Different machines have been analysed with both simulation and experimental test.

Finally, a new method for polarity detection has been proposed for locked rotor IPMSM. It has been demonstrated that the properties of the differential cross-saturation inductance can be exploited to extract information about the correct direction of the estimated d axis. The experimental tests confirmed the effectiveness of the suggested polarity detection method and that it can be correctly applied for every rotor electrical

position. The main advantage of this strategy is that it can be easily combined with the high frequency voltage injection based sensorless technique without the need of extra filtering stage.

This thesis has described the work done during the three years of Ph.D. studies. The topics analysed in this work could be object of further research activities since there still is room for improvement. Hereafter some ideas for future works and developments are reported.

First, the compensations used to enhance the convergence range of the position estimation are based on the knowledge of the magnetic characteristic of the machine. To measure the machine fluxes a test bench with a master motor or a brake are necessary. However, in many industrial applications they are not available. To allow these compensation methods to spread in industry it would be interesting to study an identification procedure allowing to estimate the magnetic characteristics without the need of a dedicated test bench.

I believe that a natural development of this thesis is to realize a wide speed range sensorless drive for IPMSM and SyRM combining the control techniques analysed so far with a high-speed position estimation algorithm.

Appendix

This Appendix compares the high frequency voltage injection along the estimated d and q axes focusing on their effects on the position estimation algorithm and on the torque production.

Injection along the estimated direct axis

The high frequency voltage signals used to estimate the rotor position are described in (a). The signals are expressed in the estimated reference indicated with the superscript x.

$$\begin{aligned} u_{hd}^{x} &= U_h cos(\omega_h t) \\ u_{hq}^{x} &= 0 \end{aligned} \tag{a}$$

The high frequency machine model in (b) is used to derive the expression of the currents i_{hd}^{x} and i_{hq}^{x} induced in the stator windings. The speed dependent terms can be neglected since the estimation algorithm works at standstill or low speed. As the model aim is to describe the machine response to high frequency voltages the differential inductances are considered and the resistive voltage drop can be neglected. For the sake of simplicity the inductances dependence on the machine working point is omitted.

$$\begin{aligned} u_{hd} &= \ell_d \frac{\mathrm{d}i_{hd}}{\mathrm{d}t} + \ell_{dq} \frac{\mathrm{d}i_{hq}}{\mathrm{d}t} \\ u_{hq} &= \ell_{dq} \frac{\mathrm{d}i_{hd}}{\mathrm{d}t} + \ell_q \frac{\mathrm{d}i_{hq}}{\mathrm{d}t} \end{aligned} \tag{b}$$

The resulting high frequency currents are sinusoidal as described in (c), whose amplitudes I_{hd} and I_{hq} are defined in (d) and (e) where ℓ_Δ is defined as in (f).

$$\begin{aligned} i_{hd}^{x} &= I_{hd} \sin(\omega_h t) \\ i_{hq}^{x} &= I_{hq} \sin(\omega_h t) \end{aligned} \tag{c}$$

$$I_{hd} = \frac{U_h[-\ell_\Sigma - \ell_\Delta \cos(2\Delta\vartheta) + \ell_{dq} \sin(2\Delta\vartheta)]}{\omega_h(\ell_{dq}^2 - \ell_d \ell_q)} \tag{d}$$

$$I_{hq} = \frac{U_h[\ell_\Delta \sin(2\Delta\vartheta) + \ell_{dq} \cos(2\Delta\vartheta)]}{\omega_h(\ell_{dq}^2 - \ell_d \ell_q)} \tag{e}$$

$$\ell_\Delta(i_d, i_q) = \frac{[\ell_q - \ell_d]}{2} \tag{f}$$

It is important to highlight that the procedure used to derive the high frequency current expressions is general therefore (c), (d) and (e) are valid for both interior permanent magnet machines and synchronous reluctance machines. For the reluctance machine the same equations apply whether the machine model is described using the IPMSM convention (d-q), that is used in this thesis work, or the SyRM convention (D-Q) defined in subsection 1.7.1, provided that ℓ_d is substituted with ℓ_D, ℓ_q with ℓ_Q and that $\ell_\Delta = \frac{[\ell_Q - \ell_D]}{2}$.

Injection along the estimated quadrature axis

The rotor position can be estimated also injecting high frequency voltages in the estimated quadrature axis (g).

$$\begin{aligned} u^x_{hd} &= 0 \\ u^x_{hq} &= U_h cos(\omega_h t) \end{aligned} \tag{g}$$

Analogously to previous case, the currents i^x_{hd} and i^x_{hq} induced in the stator windings can be calculated using the machine model in (b). Also when the high frequency injection is performed along the quadrature axis the resulting currents are sinusoidal signals (as expressed in (c)) but with different amplitudes described in (h) and (i).

$$I_{hd} = \frac{U_h[\ell_\Delta \sin(2\Delta\vartheta) + \ell_{dq}\cos(2\Delta\vartheta)]}{\omega_h(\ell^2_{dq} - \ell_d\ell_q)} \tag{h}$$

$$I_{hq} = \frac{U_h[-\ell_\Sigma + \ell_\Delta \cos(2\Delta\vartheta) - \ell_{dq}\sin(2\Delta\vartheta)]}{\omega_h(\ell^2_{dq} - \ell_d\ell_q)} \tag{i}$$

Once again the procedure used to derive the high frequency current expressions is general therefore (h) and (i) are valid for both interior permanent magnet machines and synchronous reluctance machines. Furthermore the equations stand also if the reluctance machine is described using the SyRM convention (D-Q) provided that ℓ_d is substituted with ℓ_D, ℓ_q with ℓ_Q and that $\ell_\Delta = \frac{[\ell_Q - \ell_D]}{2}$.

Comparison of the two solutions

According to the considerations made so far, the choice of the injection axis does not have an influence on the position estimation. In fact the algorithm working principle is to nullify I_{hq} if the injection is performed on the d axis and I_{hd} when the high frequency signal is injected in q. Comparing (e) and (h) it is clear that the currents have the same expression and so they feature the same dependency on the estimation error and on the machine inductances and working point. Therefore the performance of the estimation algorithm is not affected by the axis chosen for the injection of the high frequency signal.

However the choice of the injection axis affects the torque produced by the machine. The injection in fact causes high frequency torque ripple whose amplitude varies with the injection axis. A SyRM is considered and analysed in the following part. For the sake of simplicity the assumption of linearity is considered, i.e. the inductances are

constant ($\ell_d = L_d$ and $\ell_q = L_q$) and the cross-saturation inductance ℓ_{dq} is null therefore the estimation algorithm converges with no estimation error $\Delta\vartheta = 0$. In this situation the high frequency current is present only on the injection axis and can be expressed as (j) if the injection is performed along d and (k) if the injection is performed along q.

$$I_{hd} = \frac{U_h(L_\Sigma + L_\Delta)}{\omega_h L_d L_q} = \frac{U_h}{\omega_h L_d} \tag{j}$$

$$I_{hq} = \frac{U_h(L_\Sigma - L_\Delta)}{\omega_h L_d L_q} = \frac{U_h}{\omega_h L_q} \tag{k}$$

In a synchronous reluctance machine described according to the IPMSM convention the current ripple is higher if the d axis is chosen for the injection since $L_q > L_d$. Therefore, according to (1.77), a higher torque ripple is produced by the injection along d so it is preferable to inject high frequency voltage in the quadrature axis. Differently if the SyRM convention ($L_D > L_Q$) is used, higher current and torque ripple are produced if the injection is performed on the Q axis and the injection on D should be preferred.

Bibliography

[1] Y. Inoue, S. Morimoto, and M. Sanada, "A novel control scheme for maximum power operation of synchronous reluctance motors including maximum torque per flux control," *IEEE Transactions on Industry Applications*, vol. 47, no. 1, pp. 115–121, Jan 2011.

[2] X. Zhang and G. H. B. Foo, "A robust field-weakening algorithm based on duty ratio regulation for direct torque controlled synchronous reluctance motor," *IEEE/ASME Transactions on Mechatronics*, vol. 21, no. 2, pp. 765–773, April 2016.

[3] X. Zhang, G. H. B. Foo, D. M. Vilathgamuwa, and D. L. Maskell, "An improved robust field-weakeaning algorithm for direct-torque-controlled synchronous-reluctance-motor drives," *IEEE Transactions on Industrial Electronics*, vol. 62, no. 5, pp. 3255–3264, May 2015.

[4] G. H. B. Foo and X. Zhang, "Robust direct torque control of synchronous reluctance motor drives in the field-weakening region," *IEEE Transactions on Power Electronics*, vol. 32, no. 2, pp. 1289–1298, Feb 2017.

[5] Y. Ren, Z. Q. Zhu, and J. Liu, "Direct torque control of permanent-magnet synchronous machine drives with a simple duty ratio regulator," *IEEE Transactions on Industrial Electronics*, vol. 61, no. 10, pp. 5249–5258, Oct 2014.

[6] H. Hadla and S. Cruz, "Predictive stator flux and load angle control of synchronous reluctance motor drives operating in a wide speed range," *IEEE Transactions on Industrial Electronics*, vol. 64, no. 9, pp. 6950–6959, Sept 2017.

[7] D. D. Rù, M. Morandin, S. Bolognani, and M. Castiello, "Model predictive hysteresis current control for wide speed operation of a synchronous reluctance machine drive," in *IECON 2016 - 42nd Annual Conference of the IEEE Industrial Electronics Society*, vol. 2, Oct 2016, pp. 1–6.

[8] A. Yousefi-Talouki, P. Pescetto, and G. Pellegrino, "Sensorless direct flux vector control of synchronous reluctance motors including standstill, mtpa, and flux weakening," *IEEE Transactions on Industry Applications*, vol. 53, no. 4, pp. 3598–3608, July 2017.

[9] A. Yousefi-Talouki, P. Pescetto, G. Pellegrino, and I. Boldea, "Combined active flux and high-frequency injection methods for sensorless direct-flux vector control of synchronous reluctance machines," *IEEE Transactions on Power Electronics*, vol. 33, no. 3, pp. 2447–2457, March 2018.

[10] J. Ahn, S. b. Lim, K. c. Kim, J. Lee, J. h. Choi, S. Kim, and J. p. Hong, "Field weakening control of synchronous reluctance motor for electric power steering," *IET Electric Power Applications*, vol. 1, no. 4, pp. 565–570, July 2007.

[11] J. Wai and T. M. Jahns, "A new control technique for achieving wide constant power speed operation with an interior pm alternator machine," in *Conference Record of the 2001 IEEE Industry Applications Conference. 36th IAS Annual Meeting (Cat. No.01CH37248)*, vol. 2, Sept 2001, pp. 807–814 vol.2.

[12] N. Bedetti, S. Calligaro, and R. Petrella, "Analytical design and auto-tuning of adaptive flux-weakening voltage regulation loop in ipmsm drives with accurate torque regulation," in *2017 IEEE Energy Conversion Congress and Exposition (ECCE)*, Oct 2017, pp. 5884–5891.

[13] S. Bolognani, S. Calligaro, and R. Petrella, "Adaptive flux-weakening controller for interior permanent magnet synchronous motor drives," *IEEE Journal of Emerging and Selected Topics in Power Electronics*, vol. 2, no. 2, pp. 236–248, June 2014.

[14] J.-M. Kim and S.-K. Sul, "Speed control of interior permanent magnet synchronous motor drive for the flux weakening operation," *IEEE Transactions on Industry Applications*, vol. 33, no. 1, pp. 43–48, Jan 1997.

[15] S. Bolognani, S. Calligaro, R. Petrella, and F. Pogni, "Flux-weakening in ipm motor drives: Comparison of state-of-art algorithms and a novel proposal for controller design," in *Proceedings of the 2011 14th European Conference on Power Electronics and Applications*, Aug 2011, pp. 1–11.

[16] S. Bolognani, S. Calligaro, and R. Petrella, "Adaptive flux-weakening controller for ipmsm drives," in *2011 IEEE Energy Conversion Congress and Exposition*, Sept 2011, pp. 2437–2444.

[17] ——, "Adaptive flux-weakening controller for interior permanent magnet synchronous motor drives," *IEEE Journal of Emerging and Selected Topics in Power Electronics*, vol. 2, no. 2, pp. 236–248, June 2014.

[18] N. Bedetti, S. Calligaro, and R. Petrella, "Analytical design of flux-weakening voltage regulation loop in ipmsm drives," in *2015 IEEE Energy Conversion Congress and Exposition (ECCE)*, Sept 2015, pp. 6145–6152.

[19] G. Pellegrino, E. Armando, and P. Guglielmi, "Direct-flux field-oriented control of ipm motor drives with robust exploitation of the maximum torque per voltage speed range," in *2010 IEEE International Symposium on Industrial Electronics*, July 2010, pp. 1271–1277.

[20] ——, "Direct-flux vector control of ipm motor drives in the maximum torque per voltage speed range," *IEEE Transactions on Industrial Electronics*, vol. 59, no. 10, pp. 3780–3788, Oct 2012.

[21] P. Y. Lin, W. T. Lee, S. W. Chen, J. C. Hwang, and Y. S. Lai, "Infinite speed drives control with mtpa and mtpv for interior permanent magnet synchronous motor," in *IECON 2014 - 40th Annual Conference of the IEEE Industrial Electronics Society*, Oct 2014, pp. 668–674.

[22] Y.-D. Yoon, W.-J. Lee, and S.-K. Sul, "New flux weakening control for high saliency interior permanent magnet synchronous machine without any tables," in *2007 European Conference on Power Electronics and Applications*, Sept 2007, pp. 1–7.

[23] Y. Zhao, Z. Zhang, W. Qiao, and L. Wu, "An extended flux model-based rotor position estimator for sensorless control of interior permanent magnet synchronous machines," in *IEEE Energy Convers. Congr. Expo.*, Sept 2013, pp. 3799–3806.

[24] I. Boldea, M. Paicu, and G. Andreescu, "Active flux concept for motion-sensorless unified ac drives," *IEEE Trans. Power Electron.*, vol. 23, no. 5, pp. 2612–2618, Sept 2008.

[25] J. M. Liu and Z. Q. Zhu, "Rotor position estimation for dual-three-phase permanent magnet synchronous machine based on third harmonic back-emf," in *IEEE Symposium on Sensorless Control for Electrical Drives*, June 2015, pp. 1–8.

[26] S. Bolognani, S. Calligaro, and R. Petrella, "Design issues and estimation errors analysis of back-emf based position and speed observer for spm synchronous motors," in *IEEE Symposium on Sensorless Control for Electrical Drives*, Sept 2011, pp. 138–145.

[27] R. Antonello, L. Ortombina, F. Tinazzi, and M. Zigliotto, "Enhanced low-speed operations for sensorless anisotropic pm synchronous motor drives by a modified back-emf observer," *IEEE Trans. Ind. Electron.*, vol. PP, no. 99, pp. 1–1, 2017.

[28] S. Chi, Z. Zhang, and L. Xu, "Sliding-mode sensorless control of direct-drive pm synchronous motors for washing machine applications," *IEEE Trans. Ind. Appl.*, vol. 45, no. 2, pp. 582–590, March 2009.

[29] D. Liang, J. Li, and R. Qu, "Sensorless control of permanent magnet synchronous machine based on second-order sliding-mode observer with online resistance estimation," *IEEE Trans. Ind. Appl.*, vol. 53, no. 4, pp. 3672–3682, July 2017.

[30] F. Toso, D. Da Rù, and S. Bolognani, "A moving horizon estimator for the speed and rotor position of a sensorless pmsm drive," in *IEEE International Symposium on Sensorless Control for Electrical Drives*, Sept 2017, pp. 109–114.

[31] N. K. Quang, N. T. Hieu, and Q. P. Ha, "Fpga-based sensorless pmsm speed control using reduced-order extended kalman filters," *IEEE Trans. Ind. Electron.*, vol. 61, no. 12, pp. 6574–6582, Dec 2014.

[32] B. Terzic and M. Jadric, "Design and implementation of the extended kalman filter for the speed and rotor position estimation of brushless dc motor," *IEEE Trans. Ind. Electron.*, vol. 48, no. 6, pp. 1065–1073, Dec 2001.

[33] S. Nakashima, Y. Inagaki, and I. Miki, "Sensorless initial rotor position estimation of surface permanent-magnet synchronous motor," *IEEE Trans. Ind. Appl.*, vol. 36, no. 6, pp. 1598–1603, Nov 2000.

[34] M. Tursini, R. Petrella, and F. Parasiliti, "Initial rotor position estimation method for pm motors," *IEEE Trans. Ind. Appl.*, vol. 39, no. 6, pp. 1630–1640, Nov 2003.

[35] M. Boussak, "Implementation and experimental investigation of sensorless speed control with initial rotor position estimation for interior permanent magnet synchronous motor drive," *IEEE Trans. Power Electron.*, vol. 20, no. 6, pp. 1413–1422, Nov 2005.

[36] Y. Sun, M. Preindl, S. Sirouspour, and A. Emadi, "Nonlinear modeling and design of initial position estimation and polarity detection of ipm drives," in 41^{st} *Annu. Conf. IEEE Ind. Electron. Soc.*, Nov 2015, pp. 004 059–004 064.

[37] M. Corley and R. Lorenz, "Rotor position and velocity estimation for a salient-pole permanent magnet synchronous machine at standstill and high speeds," *IEEE Trans. Ind. Appl.*, vol. 34, no. 4, pp. 784–789, Jul 1998.

[38] D. Kim, Y.-C. Kwon, S.-K. Sul, J.-H. Kim, and R.-S. Yu, "Suppression of injection voltage disturbance for high frequency square-wave injection sensorless drive with regulation of induced high frequency current ripple," in *Int. Power Electron. Conf.*, May 2014, pp. 925–932.

[39] M. Morandin, A. Faggion, and S. Bolognani, "Integrated starter-alternator with sensorless ringed-pole pm synchronous motor drive," *IEEE Trans. Ind. Appl.*, vol. 51, no. 2, pp. 1485–1493, March 2015.

[40] H. Kim, K.-K. Huh, R. D. Lorenz, and T. M. Jahns, "A novel method for initial rotor position estimation for ipm synchronous machine drives," *IEEE Trans. Ind. Appl.*, vol. 40, no. 5, pp. 1369–1378, Sept 2004.

[41] Y.-S. Jeong, R. D. Lorenz, T. M. Jahns, and S.-K. Sul, "Initial rotor position estimation of an interior permanent-magnet synchronous machine using carrier-frequency injection methods," *IEEE Transactions on Industry Applications*, vol. 41, no. 1, pp. 38–45, Jan 2005.

[42] D. Raca, P. Garcia, D. D. Reigosa, F. Briz, and R. D. Lorenz, "Carrier-signal selection for sensorless control of pm synchronous machines at zero and very low speeds," *IEEE Transactions on Industry Applications*, vol. 46, no. 1, pp. 167–178, Jan 2010.

[43] S. C. Yang and Y. L. Hsu, "Full speed region sensorless drive of permanent-magnet machine combining saliency-based and back-emf-based drive," *IEEE Transactions on Industrial Electronics*, vol. 64, no. 2, pp. 1092–1101, Feb 2017.

[44] J. Holtz, "Acquisition of position error and magnet polarity for sensorless control of pm synchronous machines," *IEEE Trans. Ind. Appl.*, vol. 44, no. 4, pp. 1172–1180, July 2008.

[45] X. Luo, Q. Tang, A. Shen, and Q. Zhang, "Pmsm sensorless control by injecting hf pulsating carrier signal into estimated fixed-frequency rotating reference frame," *IEEE Trans. Ind. Electron.*, vol. 63, no. 4, pp. 2294–2303, April 2016.

[46] T. Noguchi, K. Yamada, S. Kondo, and I. Takahashi, "Initial rotor position estimation method of sensorless pm synchronous motor with no sensitivity to armature resistance," *IEEE Trans. Ind. Electron.*, vol. 45, no. 1, pp. 118–125, Feb 1998.

[47] L. M. Gong and Z. Q. Zhu, "Robust initial rotor position estimation of permanent-magnet brushless ac machines with carrier-signal-injection-based sensorless control," *IEEE Trans. Ind. Appl.*, vol. 49, no. 6, pp. 2602–2609, Nov 2013.

[48] J. A. Melkebeek and J. L. Willems, "Reciprocity relations for the mutual inductances between orthogonal axis windings in saturated salient-pole machines," *IEEE Trans. Ind. Appl.*, vol. 26, no. 1, pp. 107–114, Jan 1990.

[49] D. D. Reigosa, P. Garcia, D. Raca, F. Briz, and R. D. Lorenz, "Measurement and adaptive decoupling of cross-saturation effects and secondary saliencies in sensorless controlled ipm synchronous machines," *IEEE Trans. Ind. Appl.*, vol. 44, no. 6, pp. 1758–1767, Nov 2008.

[50] P. Guglielmi, M. Pastorelli, and A. Vagati, "Cross-saturation effects in ipm motors and related impact on sensorless control," *IEEE Trans. Ind. Appl.*, vol. 42, no. 6, pp. 1516–1522, Nov 2006.

[51] N. Bianchi, E. Fornasiero, and S. Bolognani, "Effect of stator and rotor saturation on sensorless rotor position detection," *IEEE Trans. Ind. Appl.*, vol. 49, no. 3, pp. 1333–1342, May 2013.

[52] D. Mingardi, M. Morandin, S. Bolognani, and N. Bianchi, "On the proprieties of the differential cross-saturation inductance in synchronous machines," *IEEE Trans. Ind. Appl.*, vol. 53, no. 2, pp. 991–1000, March 2017.

[53] M. Barcaro, M. Morandin, T. Pradella, N. Bianchi, and I. Furlan, "Iron saturation impact on high-frequency sensorless control of synchronous permanent-magnet motor," *IEEE Transactions on Industry Applications*, vol. 53, no. 6, pp. 5470–5478, Nov 2017.

[54] Y. C. Kwon, J. Lee, and S. K. Sul, "Full torque-range low-speed sensorless drive for heavily saturated ipmsms by manipulation of convergence point," in *2017 IEEE Energy Conversion Congress and Exposition (ECCE)*, Oct 2017, pp. 865–872.

[55] L. M. Gong and Z. Q. Zhu, "Improved rotating carrier signal injection method for sensorless control of pm brushless ac motors, accounting for cross-saturation effect," in *8th International Conference on Power Electronics - ECCE Asia*, May 2011, pp. 1132–1139.

[56] Z. Q. Zhu, Y. Li, D. Howe, and C. M. Bingham, "Compensation for rotor position estimation error due to cross-coupling magnetic saturation in signal injection based sensorless control of pm brushless ac motors," in *2007 IEEE International Electric Machines Drives Conference*, vol. 1, May 2007, pp. 208–213.

[57] S. Kuehl, P. Landsmann, and R. M. Kennel, "Compensating angle estimation errors caused by magnetic saturation in anisotropy-based sensorless control schemes," in *3rd IEEE International Symposium on Sensorless Control for Electrical Drives (SLED 2012)*, Sept 2012, pp. 1–6.

List of Acronyms

PMSM	Permanent Magnet Synchronous Machine
IPMSM	Interior Permanent Magnet Synchronous Machine
SyRM	Synchronous Reluctance Machine
MTPA	Maximum Torque per Ampere
FW	Flux Weakening
MTPV	Maximum Torque per Voltage
CVC	Current Vector Control
DTC	Direct Torque Control
MPC	Model Predictive Control
MIMO	Multiple Input Multiple Output
PWM	Pulse Width Modulation
LUT	Look-Up Table
HF	High Frequency